Development and Characterisation of RPC Detectors and Determination of Neutrino Oscillations Sensitivity for the INO-ICAL Experiment

Thesis Submitted to the University of Delhi
for the Degree of

DOCTOR OF PHILOSOPHY
IN PHYSICS

DALJEET KAUR

SUPERVISOR
DR. MD. NAIMUDDIN

DEPARTMENT OF PHYSICS AND ASTROPHYSICS
UNIVERSITY OF DELHI
DELHI - 110007
INDIA

MARCH, 2015

Declaration

The thesis entitled ***"Development and Characterisation of RPC Detectors and Determination of Neutrino Oscillations Sensitivity for the INO-ICAL Experiment"*** has been composed by Ms. Daljeet Kaur, based on research work carried out by her, at the Department of Physics and Astrophysics, University of Delhi, Delhi-110007.

This work has been carried out under the supervision of Dr. Md. Naimuddin. The material presented in this thesis is original and has not been submitted for the award of any Degree, Diploma, Associateship or Fellowship of this or any other University.

Daljeet Kaur
(Candidate)

Dr. Md. Naimuddin
(Supervisor)

Prof. Amitabha Mukherjee
Head, Department of Physics & Astrophysics
University of Delhi, Delhi-110007
India

Dedicated To

My Loving Parents

Somewhere Something

"INCREDIBLE"

Is Waiting To Be Known

-Carl Sagan

Acknowledgments

It is an immense pleasure to express my gratitude to all those people who have supported me during my Ph.D. and finally led to the accomplishment of my thesis work.

First and foremost, I would like to express my deepest respect and most sincere gratitude to my supervisor, Dr. Md. Naimuddin, for his excellent insight and guidance throughout the research work. Without his inspiring discussions, invaluable guidance and continuous encouragement, this accomplishment would have never been fulfilled. His advice and attitude made me rethink my own stance and attitude as a researcher. He provided me full freedom to express my views and ideas on various academic and non-academic matters; which was quite helpful in building my confidence. I heartiest appreciate his continuous support and patience during these five years of research, which was a great comfort. I have been amazingly fortunate to have an opportunity to work under his supervision.

I am highly thankful to my adviser Dr. Sanjeev Kumar for his invaluable expertise that was constantly available to me throughout my research work. His persistent encouragement for the understanding and development of neutrino phenomenology is gratefully acknowledged. On my personal behalf, I am very grateful to him for his wise counsel and encouragement during these years. He has been very kind and patient and always willing to lend his service whenever I approached him. Without his supervision and constant help this thesis would not have been possible.

I can not forget to express my sincere thanks to Late Dr. Shahnawaz Hussain, who brought me into this field of research. Although, his support was very limited due to his sudden and sad demise, but his inspiring words and blessings were always there to direct me the right path.

I am deeply thankful to Prof. R. K. Shivpuri, Dr. Kirti Ranjan, Dr. Ashok Kumar and Dr. Ashutosh Bhardwaj for their continuous support and advise throughout the research work. They have also been a constant source of motivation and encouragement. A sincere thanks to Prof. Amithabha Mukherjee, Head, Department of Physics, for providing me adequate facilities to work in the department.

I am really grateful to Prof. Naba Kumar Mondal, Spokesperson of the INO experiment, who provided me a chance to work on such a great experiment. It gives me great

pleasure to acknowledge the guidance, valuable suggestions and constructive criticism provided by the INO physics group. Especially, I want to thank Prof. Amol Dighe, Prof. D. Indumathi, Prof. M.V.N Murthi, Prof. Nita Sinha, Prof. Sandhya Chaubey, Prof. Sanjib Kumar Agarwalla, Prof. Srubabati Goswami, Prof. Prafulla Behera, Prof. Brajesh Chaudhary, Prof. Gobinda Majumder and Prof. S. Uma Sankar for their important and invaluable suggestions and physics discussions whenever needed. I also owe my sincere thanks to Dr. Satyanarayana Bheesette and Mr. R. Shinde for their continuous help in the RPC development work. Moreover, I would like to thank all the people involved in INO simulation and Physics analysis group. I thank Anushree Ghosh, Tarak Thakore, Moon Moon Devi, Meghna K.K., Lakshmi S. Mohan, Kanishka Rawat, Kolahal Bhattacharya and many other INO colleagues for their constant motivation and support throughout the work. Further, I would like to thank the whole INO collaboration.

I am grateful to my colleagues at CDRST lab; Ajay Kumar, Aman Phogat, Aashiq Hussain, Arun Mittal, Geetika Jain, Kavita Lalvani, Pavan Pandey, Prabhjot Singh, Prajesh Sharma, Priyanka Phogat, Mohit Gola, Varun Sharma, Ramkrishna Sharma, Sudha Aahuja and Sumit Keshri for their constant corporation, important discussions and for creating a nice and friendly lab environment. A special thank to Ankit Gaur, Purnendu Kumar, Praveen Kumar, Swati Mishra and Md. Hasbuddin for their efforts and help during RPC lab work. I am also delighted to express word of thanks to my friends; Shivali Malhotra and Jyoti Sharma for all those unforgettable moments which I shared with them. Their continuous love and support gave me strength to work hard throughout this endeavor.

The thesis would not have come to a successful completion, without the help I received from the staff of the CDRST lab. I am thankful to Md. Yunus, Amir, Sanjay Singh and Puran Singh for providing me all comfort during my studies. I also thank the administration, official staff of the Department of Physics & Astrophysics and finance office staff (Branch-X) of the University of Delhi, and especially Mr. P. Kundra from the departmental official staff, who have rendered their help with very high efficiency and pleasure.

I am grateful to the Council of Scientific and Industrial Research (CSIR), New Delhi for providing financial support in terms of fellowship as a Junior Research Fellow (JRF) for the first two years and Senior Research Fellow (SRF) for the subsequent years of my research period. I acknowledge the Department of Science and Technology (DST), New Delhi for providing financial support for the project and for international travel grant. I am also very thankful to INO collaboration for providing me financial support for the collaboration meetings.

I do not find any words to express my sincere gratitude to my parents, Mr. Barjinder Singh and Mrs. Pervinder Kaur and my brother Simran Jeet Singh for their limitless love, inspirations and efforts during these many years. Thank you Mamma and Daddy for always supporting me and believing in me. I also want to thank all my family and relatives for their continuous help and immense love during my hard times in Delhi. I have been consider myself very lucky to have such a nice family and friends. Finally, I want to acknowledge all those, who knowingly and unknowingly contributed in making my work easier and a real success.

Thank you GOD for everything!!

Daljeet Kaur

List of Publications

Publications in Peer Reviewed Journals

1. ***Characterisation of 3 mm glass electrodes and development of RPC detector for INO-ICAL experiment***
   Daljeet Kaur, Ashok Kumar, Md. Naimuddin et al., Nuclear Instrumentation and Methods (NIM) **A** 774 (2015), arXiv:1412.4998
   (Impact factor: 1.316)

2. ***Characterisation of glass electrodes and RPC detectors for INO-ICAL experiment***
   Md. Naimuddin, **Daljeet Kaur**, Ashok Kumar et al., Journal of Instrumentation (JINST) **9** C10039, (2014), arXiv:1409.7184
   (Impact factor: 1.526)

3. ***Study of RPC bakelite electrodes and detector performance for INO-ICAL***
   Ashok Kumar, **Daljeet Kaur**, Md. Naimuddin et al., Journal of Instrumentation (JINST) **9** C10042, (2014), arXiv:1409.5522.
   (Impact factor: 1.526)

4. ***Hadron energy response of the ICAL detector***
   Moon Moon Devi, **Daljeet Kaur**, Md. Naimuddin et al, Journal of Instrumentation (JINST) **8** P11003 (2013), arXiv:1304.5115
   (Impact factor: 1.526)

5. ***Hadron energy resolution as a function of iron plate thickness at ICAL***
   Lakshmi S. Mohan, **Daljeet Kaur**, Md. Naimuddin et al., Journal of Instrumentation (JINST) **9** T09003 (2014), arXiv:1401.2231
   (Impact factor: 1.526) [Not included in thesis]

6. ***INO-ICAL detector sensitivity for the neutrino oscillation parameters***
   Daljeet Kaur, Md. Naimuddin, Sanjeev Kumar, arXiv:1409.2231 (2015) (to be published in European Physical Journal C)
   (Impact factor: 5.436)

7. ***Physics potential of the ICAL detector at the India-based Neutrino Observatory (INO) [INO white paper]***
   (To be submitted & not included in thesis)

Conference Proceedings

---

1. *Hadron energy resolution and physics analysis at INO-ICAL detector*
   DAE symposium on nuclear physics, December 2012, University of Delhi, India
   Proceedings of the DAE Symp. on Nucl. Phys. 57 (2012)

2. *Characterisation of different electrode materials and Resistive Plate Chamber detector performance studies*
   DAE symposium on nuclear physics, 8-12 December 2014, Banaras Hindu University, India
   Proceedings of the DAE Symp. on Nucl. Phys. 59 (2014)

3. *Hadron energy resolution at INO-ICAL detector*
   International Workshop on neutrino factories, super beams and beta beams (NUFACT), 19-24 August 2013, Beijing, China (to be published in IOP conference series).

4. *Precision measurement of neutrino oscillation parameters at INO-ICAL detector*
   International conference on High Energy Physics, 2-9 July 2014, Valencia, Spain (to be published in Nuclear physics B).

5. *INO-ICAL detector sensitivity for neutrino oscillation parameters*
   Particles and Nuclei International Conference (PANIC), 25-29 August 2014, Hamburg, Germany (to be published)

6. *INO-ICAL detector sensitivity for neutrino oscillation parameters*
   International Conference on Unification and Cosmology after Higgs discovery and

BICEP, Panjab University, Chandigarh India, May 13-15, 2014. (to be published in Pramana Journal of Physics)

National & International Conferences / Workshops / Schools

- Attended "SERC school on Experimental high energy physics", Variable energy cyclotron center (VECC), Kolkata, 20 June- 10 July, 2011.
- "Neutrino Lecture Series", IMSc, Chennai, 19-21 December 2011.
- **Presented a poster** titled "Hadron Energy Resolution at INO-ICAL detector" at Workshop on the frontiers of nuclear and particle physics, Aligarh muslim university, Aligarh, India, March 19-20 2012.
- **Presented a poster** titled "Hadron Energy Resolution at INO-ICAL detector""National Symposium on particle detector and Instrumentations", Tata institute of fundamental research (TIFR), Mumbai, 21-24 March 2012.
- **Presented a poster** titled "Hadron energy resolution and physics analysis at INO-ICAL detector" at DAE Symposium on Nuclear Physics, Delhi, India, December 3-7, 2012.
- **Presented a poster** titled "Hadron energy resolution at INO-ICAL detector" at XX DAE-BRNS High Energy Physics Symposium, Visva-Bharati, Santiniketan (India), Jan 13-18, 2013,
- Attended "Particle physics at the cross roads", Edinburgh-Delhi Particle physics symposium, India International Center (IIC), Delhi, 15-17 February 2013.
- Attended"International Neutrino Summer School", Beijing, China, 6-16 August 2013.
- **Presented a poster** titled "Precision measurement of neutrino oscillation parameters @ INO-ICAL detector" at Workshop on contemporary trends in high energy physics and instrumentation, 10-11 March, 2014, Chandigarh, India.
- **Presented a poster** titled "Precision measurement of neutrino oscillation parameters @ INO-ICAL detector" at International conference on high energy physics, July 2-9 , 2014, Valencia, Spain.

- **Presented a talk** titled “Precision measurement of neutrino oscillation parameters at INO-ICAL detector” at International Conference on Unification and Cosmology after Higgs discovery and BICEP, Panjab University, Chandigarh India, May 13-15, 2014.

- **Presented a talk** titled “INO-ICAL detector sensitivity for the neutrino oscillation parameters” at XXI DAE-BRNS High Energy Physics Symposium, IIT Guwahati, India, Dec 8-12, 2014.

- **Actively participated and presented work in regularly INO Collaboration meetings.**

Abstract

To study the properties of atmospheric neutrinos, the India-based Neutrino Observatory (INO) has been approved to be set up at Theni (TamilNadu) in South India. A 50 kton magnetised Iron CALorimeter (ICAL) will be the main experiment at INO to address the current issues of neutrino physics like neutrino mass hierarchy, octant of θ_{23} and the precise determination of neutrino mixing parameters. In the first phase of INO, glass Resistive Plate Chambers (RPCs) will be used as active detector to track the charged particles produced through the interaction of muon neutrinos with iron target. This thesis presents results from an extensive R $\&$ D of RPC detector together with the simulation studies performed for estimating the detector response to hadrons and finally neutrino oscillation sensitivity study for the ICAL detector.

RPCs are the gaseous detectors with rather good efficiency and time resolution. The performance of RPC detectors are highly depend upon the quality of electrodes and various properties like surface uniformity and resistivity of the electrode material. We have characterised different electrodes of Bakelite and Glass materials for these properties. Using these electrodes single gas gap small RPCs have been fabricated and characterised under different operational conditions like temperature and humidity. Efficiencies, count rate and leakage current measurements for these RPCs using NIM/VME data acquisition system with different gas compositions have been performed. This thesis describes these studies and suggest the best electrodes for INO-ICAL RPC with appropriate operational conditions and gas mixtures.

The ICAL detector is sensitive to muons as well as hadrons produced in neutrino interactions. A GEANT4 based Monte Carlo simulation study has been performed to obtain the detector response for hadrons. Using the obtained efficiencies, energy and direction resolutions of ICAL detector, sensitivity studies for ICAL detector have been performed. This thesis focuses on the precision measurement of atmospheric neutrino oscillation parameters, octant of θ_{23} and the mass hierarchy study for INO-ICAL detector. These physics analyses have been performed using muon neutrino events, generated through Monte Carlo NUANCE event generator. A marginalised χ^2 analyses based on neutrino energy and muon zenith angle binning scheme has been performed to determine the sensitivity for the atmospheric neutrino mixing parameters ($\sin^2\theta_{23}$ and $|\Delta m^2_{32}|$).

Contents

List of Figures

List of Tables

Chapter 1

Introduction

Neutrinos have been playing a unique role in the formation of this universe since their birth around 14 billion years ago right after the big-bang explosion. These neutrinos exist everywhere in the universe and are known as nature's ghost messengers. Nowadays, study of these neutrinos is quite fascinating as these "ghostly particles" play a decisive role in nuclear and elementary particle physics, as well as in astrophysics, cosmology and geophysics. Because they interact so weakly with matter, some of their most basic properties, such as their mass and charge conjugation symmetry, are largely unknown. This thesis, while describing some aspects of neutrino physics, focus on our efforts to know about the mass and mixing of the neutrinos in the context of India-based Neutrino Observatory (INO)[1, 2].

1.1 Neutrinos

Neutrinos are one of the most abundant elementary particles in the set of building blocks of nature. They pass through almost all of the matter without leaving any effect; billions of them are passing harmlessly through our body right now. Their masses are so tiny that so far no experiment has succeeded in measuring them accurately. They travel at nearly the speed of light. They are charge less, spin-half particles which comes in three flavors ν_e, ν_μ and ν_τ, along with their anti-particles.

The elementary particles and their interactions are well described by SU(3) $\times$ SU(2) $\times$ U(1) gauge theory commonly known as Standard Model (SM) of particle physics. Six leptons, six quarks and their anti-particles along with four force carriers (bosons) are the

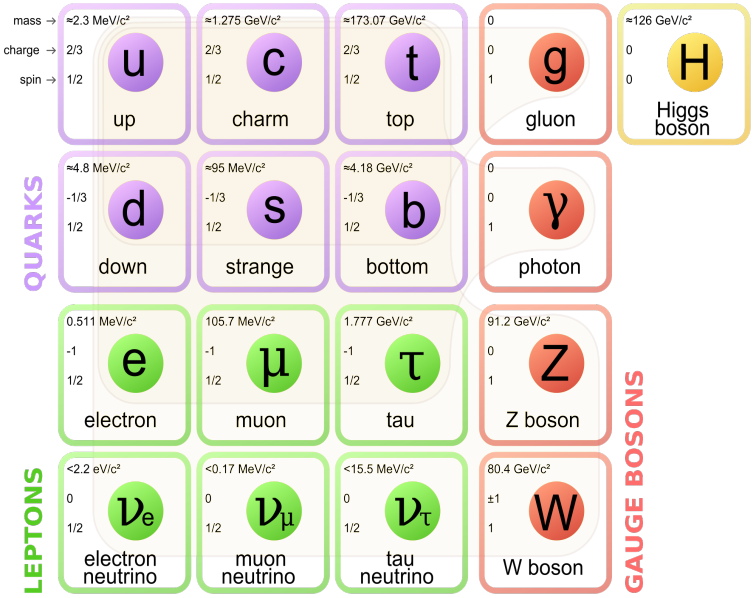

Figure 1.1: Standard Model of Particle Physics [3]

basic building blocks of Standard Model (Figure 1.1). These fermions are grouped into three generations and their masses increase with generation . The standard model describes interactions between these fundamental constituents of matter (quarks and leptons) via the electromagnetic, weak and strong forces which are mediated by the exchange of gauge bosons. In electromagnetic interactions, electric charge is conserved and this force is mediated by the mass-less photon. The short-range strong force between quarks is carried by the mass-less colored gluons and in this case the color charge is conserved. The quark binding through the color interaction is what gives rise to formation of the proton, neutron and all other hadrons. The charged leptons do not interact via the color force, but experience the electromagnetic and weak force. Massive W and Z exchange bosons are compatible with the short-range nature of the weak force. These standard model fundamental particles acquire mass by interacting with the Higgs field via the exchange of 125 GeV massive Higgs boson which has been discovered at LHC experiments [4, 5, 6].

Today, the neutrino is known as one of the fundamental particles belonging to the lepton family of the SM which interact primarily through weak force. Generally, neutrinos are referred to as electron neutrino ν_e, muon neutrino ν_μ, or tau neutrino ν_τ depending upon the production of charged leptons on their interactions. All three different types of neutrinos are complemented by their anti-particles called anti-neutrinos. As neutrinos are charge less, they can be their own anti-particles. Till now, we do not have any experimental evidence

whether neutrinos are their own anti-particles or not. Experiments such as Neutrino less Double Beta Decay (NDBD) may tell us the answer in the future. Neutrino less double beta-decay can only occur if neutrinos and anti-neutrinos are the same particles but this decay mode has not been observed yet. Neutrinos are point like particles and are described as exactly mass less within the theory of standard model. But many experiments have revealed their massive nature and have shown that neutrinos are not mass less. Thus, the study of neutrinos could provide a hint for a physics beyond the standard model.

1.2 A Brief History of Neutrinos

Theoretically, the existence of neutrinos was first postulated by W. Pauli as a neutral and mass less particle with half integer spin to explain the energy and momentum conservation in beta decay [7]. Pauli initially thought to call this mysterious particle a "neutron", but this led to come confusion when James Chadwick discovered a massive nuclear particle in 1932 [8, 9] and named it neutron. Soon after, Enrico Fermi developed a theory of weak interactions and decided to fix a new term for this particle "Neutrino" which means "the neutral one" [10]. Scientists didn't detect neutrinos until over thirty years later. The first experimental evidence of electron anti-neutrino induced interaction was brought by Reines & Cowan in 1953 [11], using reactor electron anti-neutrinos in the inverse beta-decay process, $\nu_e + p \rightarrow n + e^+$. In addition to the electron neutrino emitted in nuclear beta decay, two other neutrinos were also discovered. The identity of muon neutrino (ν_μ) was proved in 1962 [12].

In the late 1980's, precision measurements of the invisible Z boson width by the LEP experiments [13] showed the existence of only three active light neutrinos flavors within the standard model. Almost a decade later after the discovery of ν_μ, the discovery of tau lepton indicated the existence of a tau type of neutrino ν_τ which was finally discovered in 2001 by Direct Observation of the Nu Tau (DONUT) experiment [14], thus completing the observation of the three neutrinos.

1.3 Sources of Neutrinos

The sources of naturally occurring neutrinos are both terrestrial and extraterrestrial. The main source of naturally produced neutrinos is our sun. Within the galaxy, a star (like sun) produces a large number ($\sim 5 \times 10^6\ cm^{-1}s^{-1}$) of neutrinos in fusion processes. Other than

sun, supernova burst is also an important source for neutrino emission. The galaxy has relic neutrinos left over from supernova bursts and the formation of the universe during the Big Bang. On Earth, neutrinos are produced naturally by some radioactive isotopes, such as carbon-14 and potassium-40, and also by cosmic rays striking the Earth's atmosphere. The Earth has a flux of $6 \times 10^6\ cm^{-1}s^{-1}$ geological neutrinos from natural radiation. They can also be produced artificially by nuclear reactors and by particle accelerators. Reactor neutrinos come from radioactive beta decay process. Nuclear fission releases about 200 MeV of energy, of which roughly 6% is radiated away as anti-neutrinos. Some reactors have capability to produce over 10^{20} neutrinos per second. Accelerator neutrinos come from exactly the same process as cosmic-ray neutrinos, just in a more controlled environment. An accelerator facility called "neutrino factory" is also proposed to produce neutrino beam through muon decays. The energy spectrum of naturally produced neutrinos starts from fractions of electron-volts and covers a wide range. Figure 1.2 shows the spectra of neutrinos from different sources. However, this thesis will focus on the neutrinos that are

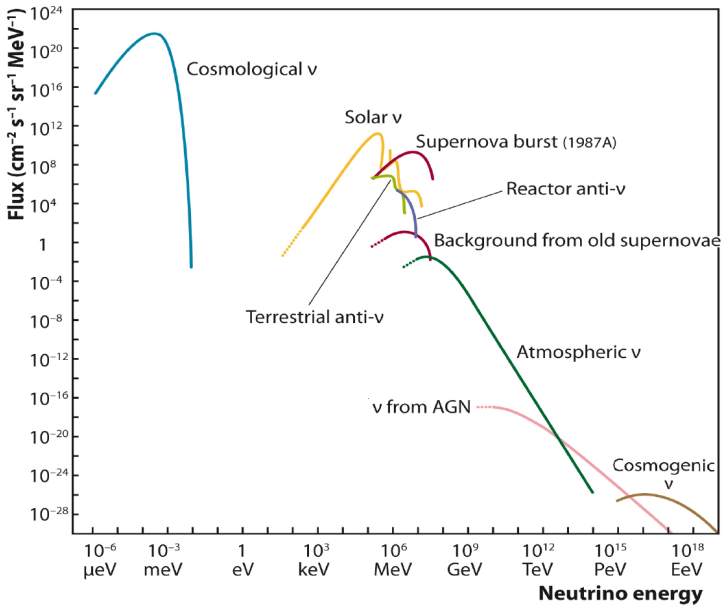

Figure 1.2: Neutrino spectrum from different terrestrial and extraterrestrial sources [15]

produced in the Earth's upper atmosphere due to cosmic rays. Therefore, here we will discuss in detail the production of atmospheric neutrinos.

1.3.1 Atmospheric Neutrinos

Earth receives an approximately isotropic and constant flux of cosmic rays. The primary cosmic rays consists of mainly protons with around 10-15$\%$ heavier nuclei. Atmospheric neutrinos are produced due to the interaction of these high energy protons with nitrogen and oxygen nuclei present in the air. Pions are copiously produced in these interactions as well. Among them, positively or negatively charged pions decay into a muon and a muon anti-neutrino. Further, most of the muons produced in the upper atmosphere decay into electron (or positron), muon neutrino, and electron anti-neutrino. The dominant part of decay chain producing atmospheric neutrinos, are

$$\begin{aligned} \pi^+ &\rightarrow \nu_\mu\, \mu^+, \qquad \mu^+ \rightarrow e^+ \nu_e \bar{\nu_\mu}. \\ \pi^- &\rightarrow \mu^-\, \bar{\nu_\mu}, \qquad \mu^- \rightarrow e^- \bar{\nu_e} \nu_\mu. \end{aligned} \tag{1.1}$$

Thus, atmospheric neutrinos come in both ν_μ and ν_e ($\bar{\nu}_\mu$ and $\bar{\nu}_e$) flavors with the ν_μ flux almost double than total of ν_e flux. Production of atmospheric neutrinos from cosmic shower is shown in Figure 1.3(a). These neutrinos cover a wide range of energies (E), from a few tens of MeV to several GeV, and although their flux decreases rapidly for large E, neutrinos of the order of TeV energies are also observed. A detector near the surface observes neutrino that travel about 15 km atmospheric height called downward-going neutrinos, while neutrinos which are coming towards detector from below, traveling up to $\approx$ 12000 km through the earth are called upward-going neutrinos as shown in Figure 1.3(b).

1.4 Neutrino Oscillations

The idea of neutrino oscillations was first introduced by Bruno Pontecorvo in 1957 [17]. The Ray Devis's chlorine experiment in the Homestake mine, South Dakota [18] measured the ν_e by analyzing the Argon (Ar) atom production through the reaction $\nu_e + Cl^{37} \rightarrow Ar^{37} + e^-$. It was observed that the measured flux of ν_e was $\sim$1/3 of that predicted by various solar model calculations. This deficit is famously known as solar neutrino problem. The description about the experiments dedicated for solving the solar neutrino anomaly are given in later section of this chapter. From multiple solar neutrinos experiments, with different measurement techniques, it was confirmed that the deficits in the measured solar neutrino fluxes are due to the conversion of ν_e flux to other flavors. The observed flavor change of neutrinos from one type into another is a result of their massive nature. They

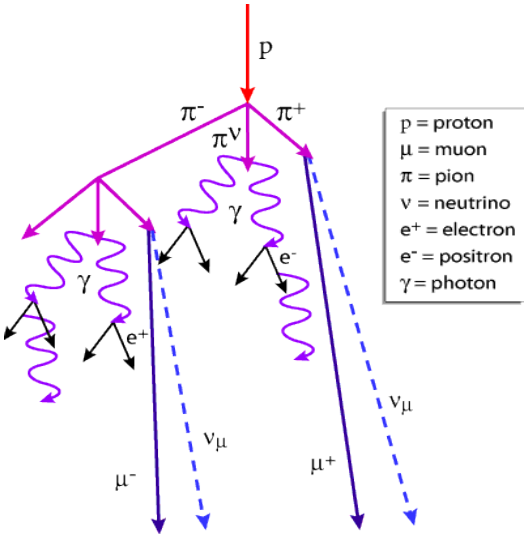

(a) Atmospheric neutrino production

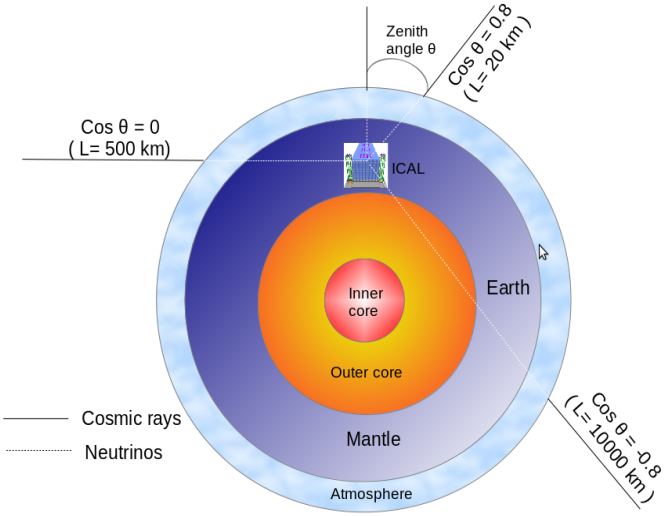

(b) Detection scheme of atmospheric neutrinos

Figure 1.3: Production of atmospheric neutrinos from cosmic rays [16] and their detection scheme at detector placed on Earth.

continuously evolve on their journey through a quantum mechanical phenomenon known as neutrino oscillations.

The consequence of the finite masses of neutrino can be explained with the theory of neutrino oscillations. Neutrino have masses means that there is spectrum of neutrino mass eigenstates ν_1, ν_2 and ν_3 with three flavor eigenstates ν_e, ν_μ and ν_τ. Leptonic mixing is considered by the leptonic decay of $W^\pm$ boson into a charged lepton and a neutrino

$$W^\pm \rightarrow \nu_i + \bar{l}_\alpha, \tag{1.2}$$

where $\alpha = e, \mu$ or τ and l_α referred to a charged lepton of flavor α. The amplitude for $W^\pm$ decay to produce specific combination $\bar{l}_\alpha + \nu_i$ $(i = 1, 2, 3..)$ is denoted by $U^*_{\alpha i}$. The neutrino of flavor α is then can be written as the superposition of mass eigenstates as

$$|\nu_\alpha\rangle = \sum_i U^*_{\alpha i} |\nu_i\rangle , \tag{1.3}$$

where $U^*_{\alpha i}$ is the unitary neutrino mixing matrix and $|\nu_i\rangle$ is the mass eigenstate. Above Eq. 1.3 may be inverted to express each mass eigenstate ν_i as a superposition of flavors:

$$|\nu_i\rangle = \sum_i U_{\alpha i} |\nu_\alpha\rangle . \tag{1.4}$$

The flavor-α fraction of ν_i is $|U_{\alpha i}|^2$. When ν_i interacts in a detector and produces a charge lepton then this flavor-α fraction is the probability that the charge lepton will be of flavor α.

Consider the case of vacuum oscillations assuming that state ν_α is a linear combination of mass eigenstates ν_i. ν_α evolves in time by applying the Schrodinger equation to a mass eigenstate as:

$$|\nu_i(\tau_i)\rangle = e^{-i(m_i \tau_i)} |\nu_i(0)\rangle , \tag{1.5}$$

where τ_i is the time in the frame of ν_i. In terms of the time t and distance L traversed by neutrino in the laboratory frame the phase factor can be written as:

$$e^{-im_i\tau_i} = e^{-i(E_i t - p_i L)}, \tag{1.6}$$

where E_i and p_i are the energy and momentum of ν_i respectively. Considering the neutrino

as a relativistic particle, the phase factor at $t \approx L$ is

$$e^{-im_i\tau_i} = e^{-i(E_i - p_i)L}. \tag{1.7}$$

If the neutrino ν_α is produced with momentum p, so that all the mass eigenstates have same momentum, the energy E_i of the mass eigenstate ν_i, with mass m_i will be

$$\sqrt{p^2 + m_i^2} \approx p + \frac{m_i^2}{2p}. \tag{1.8}$$

As the neutrinos are extremely light particles, one may consider $m_i^2 \ll p^2$ then phase factor becomes

$$e^{-im_i\tau_i} = e^{-i(m_i^2/2p)L}. \tag{1.9}$$

Using this result, it follows from Eq. 1.3 that the vector state of neutrino while traveling a distance L is

$$|\nu_\alpha(L)\rangle \approx \sum_i U^*_{\alpha i} e^{-i(m_i^2/2E)L} |\nu_i\rangle , \tag{1.10}$$

where $E \approx p$ is the average energy of the mass eigen states. Since the matrix U is unitary we can invert Eq. 1.3 and put the result in Eq. 1.10. We have

$$|\nu_\alpha(L)\rangle \approx \sum_\beta \left[\sum_i U^*_{\alpha i} e^{-i(m_i^2/2E)L} U_{\beta i} \right] |\nu_\beta\rangle . \tag{1.11}$$

The probability for a neutrino to change from one flavor α to another flavor β while traveling a distance L through vacuum with energy E is given by

$$\begin{aligned} P(\nu_\alpha \to \nu_\beta) = \delta_{\alpha\beta} &- 4 \sum_{i>j} \Re(U^*_{\alpha i} U_{\beta i} U_{\alpha j} U^*_{\beta j}) sin^2[1.27 \Delta m^2_{ij}(L/E)] \\ &+ 2 \sum_{i>j} \Im(U^*_{\alpha i} U_{\beta i} U_{\alpha j} U^*_{\beta j}) sin[2.54 \Delta m^2_{ij}(L/E)], \end{aligned} \tag{1.12}$$

where Δm^2_{ij} = $m_i^2 - m_j^2$ in eV^2, L in km and E in GeV. Assuming $\hbar = c = 1$ we have

$$\Delta m^2_{ij}(L/4E) \approx 1.27 \Delta m^2_{ij}(eV^2) \frac{L(km)}{E(GeV)}. \tag{1.13}$$

If all the neutrino masses, and consequently all the mass splittings Δm^2_{ij} vanishes then $P(\nu_\alpha \rightarrow \nu_\beta) = \delta_{\alpha\beta}$. The probability $P(\bar{\nu_\alpha} \rightarrow \bar{\nu_\beta})$ for the corresponding anti-neutrino oscillation may be found from $P(\nu_\alpha \rightarrow \nu_\beta)$ using the fact that the process $\bar{\nu_\alpha} \rightarrow \bar{\nu_\beta}$ is the CPT mirror image of $\nu_\alpha \rightarrow \nu_\beta$. Thus assuming that the CPT invariance holds,

$$P(\bar{\nu_\alpha} \rightarrow \bar{\nu_\beta}) = P(\nu_\alpha \rightarrow \nu_\beta). \tag{1.14}$$

Now from eq (1.12) we see that,

$$P(\nu_\alpha \rightarrow \nu_\beta; U) = P(\bar{\nu_\alpha} \rightarrow \bar{\nu_\beta}; U^*). \tag{1.15}$$

Thus,

$$P(\bar{\nu_\alpha} \rightarrow \bar{\nu_\beta}; U) = P(\nu_\alpha \rightarrow \nu_\beta; U^*). \tag{1.16}$$

That is, the probability for $\bar{\nu_\alpha} \rightarrow \bar{\nu_\beta}$ is same as for $\nu_\alpha \rightarrow \nu_\beta$, when U is replaced by U^*. But this means if U is not real, then $P(\bar{\nu_\alpha} \rightarrow \bar{\nu_\beta})$ differs from $P(\nu_\alpha \rightarrow \nu_\beta)$ by a reversal of the last term in Eq. 1.11. This difference is a violation of CP invariance; CP invariance would require that $\nu_\alpha \rightarrow \nu_\beta$ and $\bar{\nu_\alpha} \rightarrow \bar{\nu_\beta}$ have equal probabilities.

The unitary matrix U is usually parametrized in the following manner:

$$U = \begin{bmatrix} 1 & 0 & 0 \\ 0 & c_{23} & s_{23} \\ 0 & -s_{23} & c_{23} \end{bmatrix} \begin{bmatrix} c_{13} & 0 & s_{13}e^{-i\delta} \\ 0 & 1 & 0 \\ -s_{13}e^{-i\delta} & 0 & c_{13} \end{bmatrix} \begin{bmatrix} c_{12} & s_{12} & 0 \\ -s_{12} & c_{12} & 0 \\ 0 & 0 & 1 \end{bmatrix} \begin{bmatrix} e^{i\alpha_1/2} & 0 & 0 \\ 0 & e^{i\alpha_2/2} & 0 \\ 0 & 0 & 1 \end{bmatrix}. \tag{1.17}$$

In the standard parameterization, the Pontecorvo-Maki-Nakagawa-Sakata [19, 20] matrix is given by

$$U = \begin{bmatrix} c_{12}c_{13}e^{i\alpha_1/2} & s_{12}c_{13}e^{i\alpha_2/2} & s_{13}e^{-i\delta} \\ (s_{12}c_{23} - c_{12}s_{23}s_{13}e^{-i\delta})e^{i\alpha_1/2} & (c_{12}c_{23} - s_{12}s_{23}s_{13}e^{-i\delta})e^{i\alpha_2/2} & s_{23}c_{13} \\ (s_{12}s_{23} - c_{12}c_{23}s_{13}e^{-i\delta})e^{i\alpha_1/2} & (-c_{12}s_{23} - s_{12}c_{23}s_{13}e^{-i\delta})e^{i\alpha_2/2} & c_{23}c_{13} \end{bmatrix} \tag{1.18}$$

Here, $c_{ij} = \cos\theta_{ij}$ and $s_{ij} = \sin\theta_{ij}$, and θ_{12}, θ_{13} and θ_{23} are the three mixing angles. The CP-violating phase δ would lead to $P(\bar{\nu_\alpha} \to \bar{\nu_\beta}) \neq P(\nu_\alpha \to \nu_\beta)$, while α_1 and α_2 are the CP-violating Majorana phases. These phases have consequences only if the neutrinos are Majorana particles. The phase α_i are associated with the neutrino mass eigenstate ν_i in the way that $U_{\alpha i} = U^0_{\alpha i} e^{(i\alpha_i/2)}$ for all flavor of α. So from Eq. 1.11 we see that two majorana phases do not affect neutrino oscillations, regardless of whether neutrinos are Majorana or Dirac particles. Thus if $\nu_i \neq \bar{\nu_i}$ only the phase δ can cause CP violation in neutrino oscillations.

Considering the simplest case of two flavor neutrino oscillation in vacuum, in this situation there will be only single mass splitting Δm^2, and the mixing matrix can be parameterized as a rotation in terms of mixing angle θ

$$U = \begin{bmatrix} \cos\theta & \sin\theta \\ -\sin\theta & \cos\theta \end{bmatrix}. \tag{1.19}$$

So that transition probability written as

$$P(\nu_\alpha \to \nu_\beta) = \sin^2 2\theta sin^2 \left(\frac{\Delta m^2 L}{4E}\right). \tag{1.20}$$

While the neutrino of flavor α will survive with the probability

$$P(\nu_\alpha \to \nu_\alpha) = 1 - \sin^2 2\theta sin^2 \left(\frac{\Delta m^2 L}{4E}\right). \tag{1.21}$$

1.4.1 Mass Hierarchy

From the three flavor neutrino oscillations, we inferred that there are three types of mass mixing Δm^2_{21}, Δm^2_{31} and Δm^2_{32} where only two are independent

$$\Delta m^2_{32} + \Delta m^2_{21} - \Delta m^2_{31} = 0$$

From Eq. 1.12 it is clear that neutrino oscillations are only sensitive to mass squared difference rather than actual mass of neutrino. The solar experiments have inferred the sign of Δm^2_{21} from MSW effect [21] but sign of mass squared difference in atmospheric case is still unknown and the experimental prediction that $\Delta m^2_{sol} \ll \Delta m^2_{atmos}$ shows that two types of neutrino mixing can occur. One is normal hierarchy having two light states and one heavier state($m_1 < m_2 \ll m_3$); another is inverted hierarchy where these states are inverted in the order of ($m_3 \ll m_1 < m_2$). The two hierarchy scheme is shown in Fig-

ure 1.4.

Thus as illustrated in mass hierarchy scheme Figure 1.4, oscillation experiments can determine the neutrino squared-mass spectrum, but not how far above zero, this entire pattern lies.

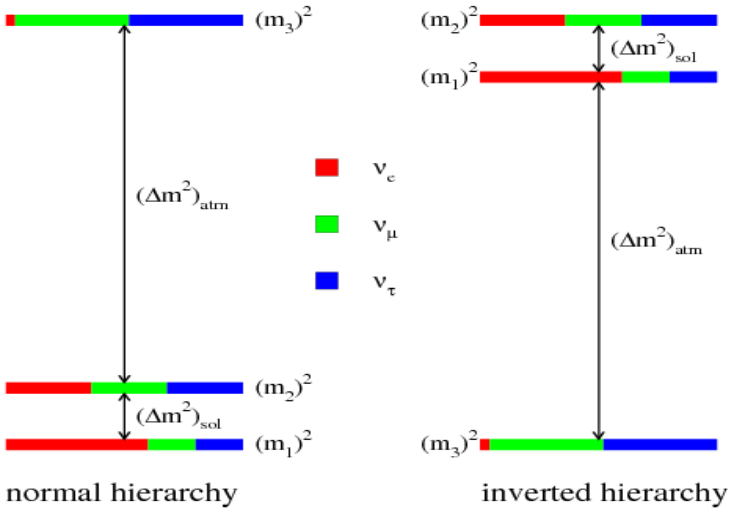

Figure 1.4: Normal and Inverted Mass hierarchy scheme for neutrinos.

Hence, two different neutrino mass ordering are possible either $m3 > m2 > m1$, called Normal Hierarchy (NH) ($\Delta m^2_{32} > 0$) or $m2 > m1 > m3$, called Inverted Hierarchy (IH) ($\Delta m^2_{32} < 0$).

1.4.2 Neutrino Flavor Change in Matter

Neutrinos can travel through matter without being absorbed, but the presence of matter can affect their propagation significantly. Neutrino oscillations are largely affected due to the coherent forward scattering interactions of the different neutrino flavors with the surrounding fermions present in matter. This was first suggested before neutrino oscillations were confirmed in 1978 by Wolfenstein [21]. The neutrino coherent forward scattering from ambient matter interferes with neutrino propagation: as a result, the probability of changing flavor can be different than that in vacuum. This effect is known as Mikheyev-Smirnov-Wolfenstein effect [21]. When neutrinos travel through a medium, they interact with the background of electron, proton and neutrons and acquire an effective mass, This modifies the mixing between flavor and mass eigen states, leading to a different oscillation probability w.r.t. vacuum. Electron neutrinos have CC and NC interactions with matter , while

muon and tau neutrinos only interacts through NC as shown in Figure 1.5.

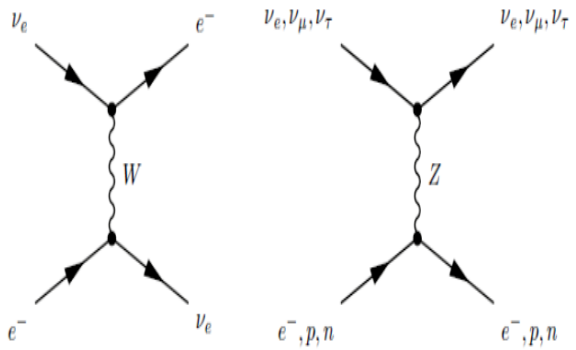

Figure 1.5: Neutrino CC and NC scattering with matter

For the neutrinos propagating in matter like the Earth, the Hamiltonian $\mathcal{H}$ can be written as:

$$\mathcal{H} = \mathcal{H}_0 + \mathcal{H}_M, \tag{1.22}$$

where $\mathcal{H}_0$ is the undisturbed Hamiltonian leading to the results discussed in Section 1.4. $\mathcal{H}_M$ is the effective weak interaction Hamiltonian due to the coherent interaction with the electrons, protons and neutrons in a medium. The neutrino flavors in Eq. 1.3 are eigenstates of $\mathcal{H}_M$ such that:

$$\mathcal{H}_M \left|\nu_\alpha\right\rangle = V_\alpha \left|\nu_\alpha\right\rangle, \tag{1.23}$$

where V_α is the effective potential depending on the neutrino flavor and is given as

$$V_e = V_{NC} + V_{CC}, \tag{1.24}$$

$$V_\mu = V_\tau = V_{NC}. \tag{1.25}$$

Here, V_{NC} and V_{CC} are the neutral and charged-current effective potential of neutrinos respectively and given by:

$$V_{CC} = \sqrt{2} G_F N_e, \tag{1.26}$$

$$V_{NC} = -\frac{\sqrt{2}}{2} G_F N_n, \tag{1.27}$$

where G_F is the Fermi constant and N_e and N_n are the electron and neutron number density in the medium. Due to the fact that the matter is considered to be free of muons and taus ν_μ and ν_τ interact only by neutral current. In the case of two neutrino flavor, one can determine

the effective squared mass difference in matter [22] as

$$\Delta M^2_{atm} = \Delta m^2_{atm} \sqrt{(\cos 2\theta_{atm} - 2EV_{CC}/\Delta m^2_{atm})^2 + \sin^2 2\theta_{atm}}, \tag{1.28}$$

and the mixing angles in matter as

$$\sin^2 2\theta_{atm,M} = \frac{\sin^2 2\theta_{atm}}{(\cos 2\theta_{atm} - 2EV_{CC}/\Delta m^2_{atm})^2 + \sin^2 2\theta_{atm}}. \tag{1.29}$$

Therefore, Eq. 1.30 has to be modified by taking matter effect into account as:

$$P(\nu_\alpha \to \nu_\alpha) = 1 - \sin^2 2\theta_{atm,M} sin^2 \left(\frac{\Delta M^2 L}{4E} \right). \tag{1.30}$$

1.5 Neutrino Experiments

Several worldwide neutrino experiments have provided impressive evidences of neutrino oscillations and their masses. Many experiments are currently running to address unresolved issues in neutrino physics, and shape the future directions of particle physics. In this section we will discuss the various neutrino experiments, their performance, current status and physics reach.

1.5.1 Solar Neutrino Experiments

The sun is a very rich natural source of neutrinos. According to the Standard Solar Model (SSM)[23], solar neutrinos are produced due to the nuclear fusion of four protons. The basic reaction for solar neutrinos is $4p + 2e \to 4He + 2\nu_e$ with a Q value of 26.7 MeV. But in fact there is a chain of reactions producing neutrinos spectrum with different energy thresholds as shown in Figure 1.6. For several years, many experiments have detected these neutrinos with the satisfactory results. The Homestake [18], a radiochemical experiment using chlorine target, was built in 1965-67 and operated until 1984. It was the first experiment to observe the solar neutrino flux and was the first one to notice a discrepancy between the observed solar neutrino flux and the expected solar neutrino flux measurement, often referred to as the "solar neutrino problem". Homestake results were also confirmed by many experiments like SAGE [24], GALLEX [25] and water cherenkov detectors like Kamiokande [26] in Japan, IMB [27] in United States. Super Kamiokande (SK) [28, 29] is

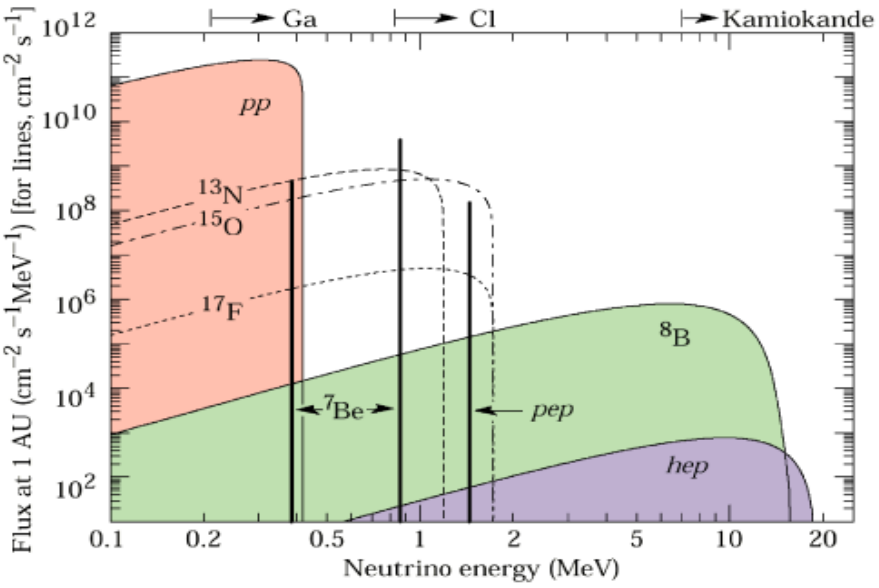

Figure 1.6: Solar neutrino flux on earth according to the standard solar model [23].

a large underground detector, comprising 50 kton pure water and 11,146 large photo multiplier tubes (PMT). It is sensitive to solar neutrino down to about 6 MeV. Besides confirming the solar neutrino deficit, its data allowed to constrain other important effects like spectral distortions and day-night variations due to a possible neutrino regeneration in the earth.

The Sudbury Neutrino Observatory (SNO) [30] experiment confirmed Super-Kamiokande results about solar neutrinos [31]. It consists of 1000 tonnes of heavy water (D_2O) at the Sudbury mine located in Canada. The SNO results were a very nice confirmation of the neutrino oscillation theory. SNO was able to study both Neutral Current (NC) interactions and Charged Current (CC) interactions. SNO found that the total number of neutrinos are consistent with the expected solar flux, and thus the disappearing electron neutrino must be oscillating into neutrinos of another flavor [31]. Results from SNO's first running phase in terms of ν_μ and ν_τ versus ν_e fluxes are shown in Figure 1.7. The three colored bands show the results from the three reaction channels used for detection. They are both consistent with each other and with the predictions from the SSM (dotted lines).

Finally, KamLAND reactor experiment [32] in Japan measuring anti-neutrinos produced by nuclear reactors, provided a very clean confirmation of "solar" neutrino oscillation and measured θ_{12} very accurately. KamLAND is located in the Kamioka mine and uses neutrinos coming from 55 nuclear reactors situated in Japan. Present best fit solution from the Super Kamiokande [29, 33] for solar neutrino combined with the reactor neutrino

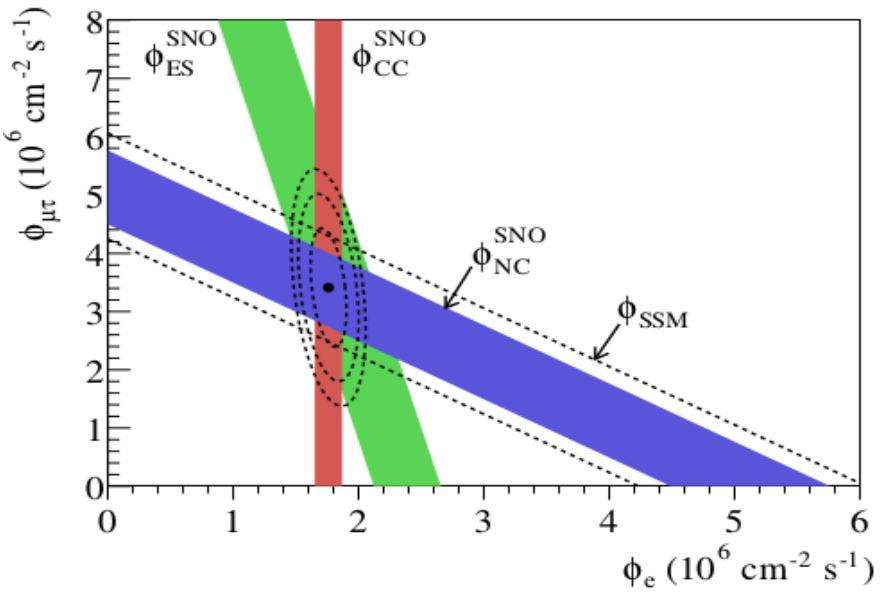

Figure 1.7: Results from SNO phase I for the CC, NC and Electron Scattering detection reactions. Results present here are in terms of the flux of B^8 solar neutrinos separated into electron-like (ϕ_e) flux and non-electron-like ($\phi_{\mu\tau}$) fluxes. The three measurements are in good agreement as expected from SSM [23].

data of KamLAND [32, 34] experiment is $\Delta m^2_{21} = 7.6 \pm 0.2 \times 10^{-5} eV^2$ and with mixing angle $\sin^2\theta_{12} = 0.31 \pm 0.01$ [33].

1.5.2 Atmospheric Neutrino Experiments

Earth atmosphere is enriched with ν_μ and ν_e types of neutrinos. The flux of atmospheric ν_μ were predicted as almost double that of atmospheric ν_e flux. In 1988, Kamiokande experiment [35] first attempted to make a measurement of the relative fluxes of these atmospheric ν_μ and ν_e. The Kamiokande experiment measured ν_e to ν_μ ratio to be 0.60 + 0.07(stat.) $\pm$ 0.05(syst.). The ν_e flux was found to be in well agreement with experimental predictions but the muon neutrino flux was $\sim 60\%$ lower than expected. Later on, these discrepancy also confirmed by the other experiments like IMB water-Cherenkov experiment, [36], MACRO [37], and Soudan-2 iron tracking-calorimeter experiment [38] and became famous with the name "Atmospheric Neutrino Anomaly". In 1998, Super-Kamionkande (SK), the water cherenkov experiment in Japan, was the first to report a conclusive measurement of the oscillations in the atmospheric sector by confirming that the deficit was due to the ν_μ to ν_τ oscillations [39]-[42]. This detector was able to measure the direction

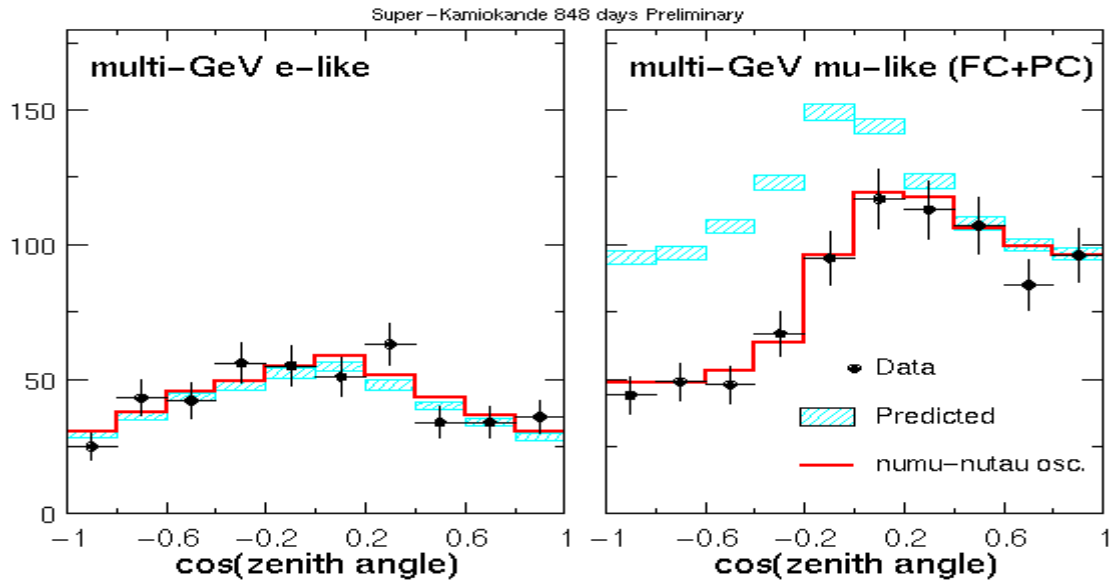

Figure 1.8: Atmospheric neutrino events as a function of zenith angle observed by SK experiment [28].

of the incoming neutrino, therefore, the interaction rates for ν_μ and ν_e events were plotted as a function of zenith angle, as shown in Figure 1.8. From this figure it is clear that the ν_e flux well matches with predictions, but the ν_μ flux is heavily dependent on the zenith angle which clearly indicates that ν_μ to ν_τ oscillations on their travel trip from their production point to the detector.

Till now SK detector has collected more statistical events, to explore and to determine the atmospheric neutrino oscillation parameters. The upgraded detector is a large underground cylindrical water cherenkov stainless-steel tank of 39 m diameter and 42 m tall, filled with 50,000 tons of ultra pure water. The detector consists of about 13,000 photomultipliers installed on the tank wall. The inner-detector instrumented with 11,146 photo multipliers (PMTs) of 20-inches and an outer veto made of 1,885 PMTs of 8-inches. The detector is located at 1000 m underground in the Kamioka-mine, Japan. The most recent oscillation studies from Super-Kamiokande are 3-flavor analyses which include all oscillation parameters, matter effects and a recent constraint on $\sin^2 2\theta_{13}$ [43]. Obtained results for normal hierarchy assumption are $\Delta m^2_{32} = 2.66^{+0.15}_{-0.40}(1\sigma) \times 10^{-3} eV^2$ and $\sin^2\theta_{23} = 0.425$ (0.391-0.619 at 90% CL). On the other hand, the results for inverted hierarchy assumption are $\Delta m^2_{32} = 2.66^{+0.17}_{-0.23}\ (1\sigma) \times 10^{-3} eV^2$ and $\sin^2\theta_{23} = 0.575$ (0.393-0.630 at 90% CL). It is clear from these results that Δm^2_{32} is almost similar for NH and IH assumption, however

octant of θ_{23} has been observed close to maximum at its best fit value but its correct octant is still unknown.

Other than Super Kamiokande detector, various interesting results for atmospheric neutrino oscillations have been provided by gigantic underground water/ice cherenkov neutrino detectors like IceCube-DeepCore [44] and ANTARES [45]. The large volume of these detectors which provide adequate statistical events, is a key feature to detect matter effects of atmospheric neutrino oscillations. Thus, these detectors are built as high energy neutrino telescopes. The IceCube neutrino telescope is a 1 Giga-ton ice cherenkov detector at South Pole. It has started partial operation since 2006 and has completed full detector construction in 2010. IceCube consists of 86 "strings" of 60 Digital Optical Modules (DOMs), each containing a photomultiplier tube (PMT). The horizontal distance between most of the IceCube strings is approximately 125 m while the DOMs on each string are separated by 17 m vertically. This geometry is supplemented by eight additional strings in conjunction with the twelve strings surrounding them, know as the DeepCore detector. The horizontal distance between DeepCore strings ranges from 42 m to 72 m. The DeepCore is sensitive to lower light levels and therefore to lower energy neutrino interactions relative to IceCube alone. The typical energy threshold to operate IceCube/Deepcore is 100 GeV, which is too high for atmospheric neutrinos, but with the aim to get down to 10 GeV. The recent results reported by IceCube are $\Delta m^2_{32} = 2.5 \pm 0.6(1\sigma) \times 10^{-3} eV^2$ and $\sin^2 2\theta_{23} > 0.92$ at 68% C.L. [46]. Results presented here are in agreement with the SK results within statistical uncertainties.

The Astronomy with a Neutrino Telescope and Abyss environmental RESearch (ANTARES) project deep sea neutrino telescope with surface area 0.1 km^2 is located in the Mediterranean sea to detect upward going muons. This detector operates on relatively high energy threshold for atmospheric neutrinos which is around 20 GeV. ANTARES also reports atmospheric neutrino oscillations using up-going muon data taken from 2007 to 2010. Their energy threshold of 20 GeV is low enough to measure the oscillation parameters. Assuming maximum mixing, Δm^2_{32} is obtained to be $(3.1 \pm 0.9) \times 10^{-3} eV^2$ [47]. It shows good agreement with existing values. Besides these detectors, some other reactor and accelerator experiments are also studying for atmospheric neutrino parameters. Details and physics results of these detectors are mentioned in next sections.

1.5.3 Reactor Experiments

- **Double Chooz:** The Double Chooz (DC) experiment [48], located in France, is a reactor experiment. The goal of this experiment is to measure non-vanishing θ_{13} neutrino mixing angle, responsible for changing electron neutrinos into other neutrino flavors. The experiment has liquid scintillator detector with fiducial mass of 8.3 tons placed at an average distance of 1050 m from two reactor cores at the Chooz nuclear power plant. The two reactors are approximately equal, with an individual thermal power of 4.25 GW. Double Chooz has been taking data with only its far detector. This experiment will also have a near detector which will be identical to the far detector and will be placed at a distance of 470 m and 350 m respectively from the two reactor cores. In the first stage, with only the far detector operating, DC has reported results with 101 live days of running and have observed a positive signal for θ_{13} at 3.1σ confidence level [49]. A more recent analysis of Double Chooz data with an exposure of 467.90 live days [50] has been reported. The best fit value for the reactor angle is obtained as: $\sin^2 2\theta_{13} = 0.090^{+0.032}_{-0.029}$ [50]. Based on rate plus spectral shape analysis, with more statistics and with systematics reduction, an improvement in the determination of the reactor mixing angle has been observed.

- **Daya Bay:** The Daya bay reactor experiment [51] is a neutrino oscillation experiment located in China. The main objective of this experiment is to measure θ_{13} precisely. The experiment observes anti-neutrinos from the Daya bay and Ling Ao (I & II) nuclear power plants (NPP). Each of them have two reactor cores to generate electron anti-neutrinos with equal individual thermal power of 2.9 GW and a total combined power of 17.4 GW. Experiment consists of six anti-neutrino detectors arranged in three experimental halls. Two detectors are located in first experimental hall, one in second experimental hall and rest of the three detectors in third experimental hall. Detector placed in first and second experimental halls serve as near detectors while detectors of third experimental hall serve as far detectors. The detectors are approximately equal, with a volume of 20 tons of Gadolinium-doped liquid scintillator as neutrino target material. The effective baselines are 512 m and 561 m for the near halls and 1579 m for the far halls [52]. The recent results reported by Daya Bay for 217 days data [53] allows a stronger rejection for $\theta_{13} = 0$ at almost 8σ. A rate-only statistical analysis of the new Daya Bay data reports a best fit value of $\sin^2 2\theta_{13}$ to be $0.090^{+0.008}_{-0.009}$. Such a high statistics sample leads to a substantial im-

provement in the statistical errors compared to the previous analysis in Refs.[51, 52].

- **RENO:** The Reactor Experiment for Neutrino Oscillations (RENO) [54] is a short baseline reactor neutrino oscillation experiment situated in South Korea. The experiment has been designed for the precise measurement of θ_{13}. RENO consists of six reactor cores, placed at equal distances from each other along a 1.3 km straight line. First two reactors have a maximum power of 2.66 GW while the other four have power of 2.8 GW respectively. Reactor anti-neutrinos are detected by two identical detectors placed near and far with effective baseline of 294 m and 1383 m from the center of reactor array respectively. Each RENO detector contains 16 tons of Gadolinium-doped Liquid Scintillator. First set of results obtained by RENO collaboration strongly confirmed the non vanishing θ_{13} value at 4.9σ level [55]. The recent results reported by RENO collaboration with 800 live days data on the basis of rate-only statistical analysis find $\sin^2 2\theta_{13} = 0.101 \pm 0.008(stat.) \pm 0.010(syst.)$ [56].

1.5.4 Accelerator Experiments

- **MINOS:** Main Injector Neutrino Oscillation Search (MINOS) [57] is a long baseline experiment designed to study the phenomena of neutrino oscillations. The experiment uses a beam of neutrino particles produced by the beam line facility called Neutrinos at the Main Injector (NuMI). The beam of neutrinos is sent through the two MINOS detectors, one at Fermilab which serves as near detector and other one in the Soudan Mine in northern Minnesota as far detector. The average distance between near and far detectors is about 735 km. The two detectors (near and far) are magnetized steel-scintillator tracking calorimeters. The main objective of MINOS experiment is to precise measure the atmospheric mixing angle (θ_{23}) and sign of mass square splitting (Δm^2_{32}) from ν_μ disappearance channel using beam line and atmospheric data. A dedicate search for the measurement of θ_{13} using ν_e and $\bar{\nu}_e$ appearance channel with anti-neutrino beam also done by MINOS experiment. The most recent results reported by MINOS collaboration [58] with combined analysis of ν_μ disappearance and ν_e appearance using both accelerator (10.7×10^{20} Protons on Target (POT) ν_μ mode and 3.36×10^{20} POT $\bar{\nu}_e$ mode) and 48.67 kton-yr atmospheric data show that $\Delta m^2_{32} = 2.34^{+0.09}_{-0.09} \times 10^{-3} eV^2$ & $\sin^2 2\theta_{23} = 0.43^{+0.16}_{-0.04}$ for normal hierarchy and $\Delta m^2_{32} = 2.34^{+0.11}_{-0.07} \times 10^{-3} eV^2$ & $\sin^2 2\theta_{23} = 0.43^{+0.19}_{-0.05}$ for inverted

hierarchy with 68% confidence level. These results also show the non-maximality of atmospheric mixing angle θ_{23}. A search for θ_{13} measurement at MINOS shows $\sin^2\theta_{13} = 0.0242 \pm 0.0025$ [59].

- **T2K:** The Tokai to Kamioka (T2K) experiment [60] is a long-baseline neutrino oscillation experiment designed to measure θ_{13} by observing ν_e appearance in a ν_μ beam. It aims to perform the precision measurement of the known oscillation parameters, Δm^2_{32} and $\sin^2 2\theta_{23}$, via ν_μ disappearance studies. The experiment uses an intense 2.5° off axis-neutrino beam generated by the J-PARC accelerator in Tokai, Japan. A near detector complex (ND280) located at a distance 280 m from the beam target, and a far detector Super-Kamiokande with fiducial volume of 22.5 kton located 295 km away from J-PARC facility for detection of neutrino oscillations. The first indication of non zero value of reactor angle was provided by T2K experiment [60], followed by the MINOS [57] and Double Chooz [48] which added up to a confidence level above 3σ. The latest results of T2K for the ν_μ disappearance channel [61] and ν_e appearance channel [62] correspond to a total exposure of 6.57×10^{20} POT in T2K have been collected during the four runs of the experiment. From disappearance data, a total number of 120 muon neutrino events have been observed at the far detector while 446.0 $\pm$ 22.5 (syst.) events were expected in absence of oscillations. Latest T2K data places the best constraint on the atmospheric angle θ_{23}. The most recent results yields $\sin^2 2\theta_{23}$=$0.514^{+0.055}_{-0.056}$ (0.511 $\pm$ 0.055) and mass square splitting Δm^2_{32} = 2.51 $\pm$ 0.10 $\times$ $10^{-3} eV^2/c^4$ (2.48 $\pm$ 0.10 $\times$ $10^{-3} eV^2/c^4$) for normal (inverted) hierarchy [61]. With appearance channel, a sample of 28 electron neutrino events have been detected when compared to 4.92 $\pm$ 0.55 expected background events in the absence of oscillations. The observed event distribution is consistent with an appearance signal at 7.6σ. A best-fit value of $\sin^2 2\theta_{13}$ = $0.140^{+0.038}_{-0.032}$ $(0.170^{+0.045}_{-0.037})$ is obtained at $\delta_{CP} = 0$ [62].

- **NOνA:** The NOνA (NuMI Off-Axis ν_e Appearance) [63] is another dedicated experiment at Fermilab designed to detect neutrino from NuMI (Neutrinos at the Main Injector) beam. A 3.3° off-axis neutrino beam from NuMI will shoot towards the neutrino detectors. NOνA will consist of two detectors, one at Fermilab (330 metric-ton near detector), and one in northern Minnesota (14 metric-kiloton far detector). The two detectors (near and far) are at a distance of 810 km apart. NOνA's main goal is to observe the oscillation of muon neutrinos to electron neutrinos. The detectors

are made up of 344,000 cells of extruded, highly reflective plastic PVC filled with liquid scintillator. Measurement of the mixing angle θ_{13}, CP-violating phase δ and determination of the neutrino mass hierarchy by observing ν_e to $\bar{\nu}_e$ appearance and ν_μ to $\bar{\nu}_\mu$ disappearance channels are the primary goals of this experiment.

1.6 PMNS Today

In previous sections, we discussed about the experiments, making efforts to find all the relevant oscillation parameters of the PMNS mixing matrix [19, 20]. Till now several experiments have provided remarkable results in evaluating the neutrino oscillations and oscillation parameters. Present best fit solution from the Super Kamiokande [28, 29] for solar neutrino combined with the reactor neutrino data of KamLAND [32, 34] experiment is $\Delta m^2_{21} = 7.6 \pm 0.2 \times 10^{-5} eV^2$ and with the mixing angle $\sin^2\theta_{12} = 0.31 \pm 0.01$ [33].

For the atmospheric neutrino anomaly mass square difference is found to be $\Delta m^2_{32} = 2.66^{+0.15}_{-0.40}(1\sigma) \times 10^{-3} eV^2$ and mixing angle $\sin^2\theta_{23} = 0.425(0.391\text{–}0.619$ at 90% C.L.) for normal hierarchy . On the other hand, the results for inverted hierarchy assumption are $\Delta m^2_{32} = 2.66^{+0.17}_{-0.23}(1\sigma) \times 10^{-3} eV^2$ and $\sin^2\theta_{23} = 0.575(0.393\text{–}0.630$ at 90% C.L.) [43].

In the last three years, neutrino oscillation physics has significantly advanced with the most spectacular result for third unknown mixing angle of PMNS [19, 20] matrix i.e. reactor mixing angle θ_{13} which is found to be non zero and have substantially large value close to its upper bound. The conclusive results for non-zero θ_{13} were presented by Daya Bay [51] and RENO [54] up to 7.7σ. The current results for θ_{13} mixing angle $\sin^2 2\theta_{13} = 0.092 \pm 0.016\ (stat) \pm 0.005\ (syst)$ from Daya bay [51], $\sin^2 2\theta_{13} = 0.113 \pm 0.013\ (stat) \pm 0.019\ (syst)$ from RENO [55] and $\sin^2 2\theta_{13} = 0.109 \pm 0.030\ (stat) \pm 0.025\ (syst)$ from Double Chooz [48] experiment gives the clear information of large θ_{13} mixing angle. Global analyses [64, 65, 66, 67] including T2K [62] and MINOS [59] results of all the neutrino oscillation data available imply a non zero value of θ_{13} at more than 10σ confidence level. According to a global analysis [67], the present best fit oscillation parameters with their 3σ ranges are listed in Table 1.1.

1.7 Future Atmospheric Neutrino Experiments

The Super-Kamiokande detector provided the first evidence for atmospheric neutrino oscillations [28]. Atmospheric neutrinos cover a broad range in energy (100 MeV to 10 TeV)

Parameters	$\theta_{12}(^\circ)$	$\theta_{23}(^\circ)$	$\theta_{13}(^\circ)$	$\delta_{CP}(^\circ)$	$\frac{\Delta m^2_{12}}{10^{-5}eV^2}$	$\frac{\Delta m^2_{32}(NH)}{10^{-3}eV^2}$
Bestfit $\pm 1\ \sigma$	$33.57^{+0.77}_{-0.75}$	$41.9^{+0.5}_{-0.4}$	$8.73^{+0.35}_{-0.36}$	266^{+55}_{-55}	$7.456^{+0.19}_{0.16}$	$2.417^{+0.062}_{-0.062}$
3σ range	31.37-36.01	37.2-54.5	7.56-9.77	0-360	6.98-8.05	2.247-2.623

Table 1.1: Present best fit values with corresponding 3σ range of neutrino oscillation parameters [67]

and path length (L $\sim$ 15 km to 12500 km). As a result of this, one can study a multitude of effects with these neutrinos including the resonant matter effects, while they pass through the earth on their way to the detector. The future detectors for atmospheric neutrinos and their salient features are summarized below.

- **Hyper-Kamiokande:** The proposed Hyper-Kamiokande (Hyper-K) [68, 69] detector will be located in Japan as a next generation underground water cherenkov detector, about 25 times larger than Super-Kamiokande. It is a multipurpose detector but it will mainly act as the far detector of a future long baseline neutrino experiment. Hyper-Kamiokande will also able to study proton decays, atmospheric neutrinos, and neutrinos from astrophysical origins. The current design for Hyper-K consists of two cylindrical tanks lying side-by-side; the outer dimensions of each tank being of width 48 m, height 54 m and length 250 m. The large detector volume will provide the significant statistics to determine the correct neutrino mass ordering and precise oscillation parameters value.

- **PINGU:** The Precision IceCube Next Generation Upgrade (PINGU) [70] is a proposed low-energy in-fill extension to the IceCube Observatory. PINGU will consist of about 20 new strings with a smaller horizontal distance between strings and a smaller vertical distance between digital optical modules (DOMs) on the strings relative to DeepCore. This will serve to further lower the energy threshold from roughly 10 GeV for DeepCore down to a few GeV. With this low energy threshold PINGU detector will be able to determine the neutrino mass hierarchy. The recent physics sensitivity of PINGU experiment is given in Ref [71].

- **Liquid Argon Detectors:** Liquid Argon detectors [72] are time projection chambers with fine-grained tracking and total absorption calorimetry. Liquid Argon detectors are known as precise tracking device that allows three-dimensional spatial reconstruction with mm-scale precision of the ionized tracks in the energy range of MeV to multi-GeV. The obtained ionization electrons are detected by drifting their paths over

several meters to wire planes. The orientation of these planes is designed to reconstruct the time, length and position of each path by recording multiple snapshots of the electrons, from which a bubble-chamber like image is constructed. The examples of Liquid argon detector experiments are LBNE (Long Baseline Neutrino Experiment), LBNO (Long Baseline Neutrino Oscillation experiment), LAGUNA etc. The sensitivity and physics reach of these detectors are mentioned in Ref [72, 73, 74].

1.7.1 INO: The India-based Future Neutrino Experiment

The observation of massive neutrinos and the discovery of neutrino oscillations requires us to revise our understanding of the fundamental building blocks of matter, and we are poised to investigate the laws of nature that govern this particle. Although the neutrino oscillation parameters are now explained with a good precision by various experiments, there are still some unknowns in neutrino sector *viz* neutrino mass hierarchy problem, CP violation phase δ_{cp}, a more precise value of θ_{13}, absolute mass of neutrinos, whether neutrinos are dirac or majorana neutrinos, etc as explained in the beginning of this chapter. Solar neutrino data constrain $\Delta m^2_{21} = m^2_2 - m^2_1$ to be positive i.e. $m2 > m1$ but there is no experimental constraint on the sign of Δm^2_{32}. The Charge-Parity (CP) violation in leptonic sector is defined by a CP violating phase δ_{CP} which is also unconstrained and can take any value in the range (-180^o to 180^o). The other important issue is the octant of atmospheric mixing angle θ_{23} i.e. how far this angle is from its maximal mixing ($\sin^2\theta_{23} = 0.5$), whether θ_{23} lies in the lower octant (LO: $\theta_{23} < 45^\circ$) or in higher octant (HO: $\theta_{23} > 45^\circ$). Recently, MINOS experiment [59] shows that $\sin^2\theta_{23}$ is non-maximal and the best-fit value for the mixing angle θ_{23} as $\sin^2\theta_{23}$ = 0.41 (LO) and $\sin^2\theta_{23}$ = 0.61 (HO). Many unexplored questions related to neutrino's actual mass and mixing is yet to be explored.

The India-based Neutrino Observatory (INO) [1, 2] has been planning to find the actual neutrino mass ordering by setting up a magnetized Iron calorimeter detector (ICAL) with its good charge identification capability to distinguish between neutrinos and anti-neutrinos interaction. The India-based Neutrino Observatory (INO) project aims to build an underground laboratory devoted study the atmospheric neutrinos. The laboratory is foreseen to be located in the Bodi-West Hills of Theni District of Tamil Nadu with an overburden of approximately 1 km of rock. The main detector at INO will be the Iron Calorimeter having modular structure with three identical modules forming a 50 kton detector. It will consist of about 150 horizontal iron layers interspersed with glass Resistive Plate Chambers (RPCs)

acting as the active detector element. Being made of iron, the ICAL detector will be magnetized with a magnetic field strength of about 1.5 T, allowing to determine the charge of muons passing though the detector. The details of the ICAL detector and its physics potentials are largely mentioned in the coming chapters of this thesis. In the shed of large θ_{13}, which is favorable for ICAL [75], INO-ICAL will look forward to achieve the following major physics goals:

- **Precision measurement of atmospheric neutrino oscillation parameters:** Several experiments have measured and confirmed the neutrino oscillation. Atmospheric data covers an extremely large range of L/E values, so a clear oscillation pattern with a clear minimum dip will be able to measure the atmospheric neutrino mixing parameters (Δm^2_{32} and $sin^2\theta_{23}$) quite precisely. Although, many experiments have announced their results for these parameters but their results have large uncertainties. Therefore, a more precise study of these oscillation parameters by observing the clear oscillation pattern is one of the major goals of INO experiment.

- **Determination of right mass hierarchy of neutrinos:** The issue of neutrino mass hierarchy i.e. whether it is "normal" (i.e. $\Delta m^2_{32} > \Delta m^2_{21}$) or inverted (i.e. $\Delta m^2_{32} < \Delta m^2_{21}$) is still unsettled. This is the most important issue at present in neutrino physics and is also one of the main goals of ICAL experiment. Atmospheric neutrinos, before reaching the detector pass through the large earth matter of different densities. Since neutrinos and anti-neutrinos interacts differently with earth matter, it is possible for ICAL to find the right neutrino mass spectrum through its charge identification capability, good energy and angular resolution.

- **Determination of right octant for θ_{23}:** The several running experiment have been able to determine quite precisely the value of neutrino mixing parameter, $sin^2\theta_{23}$, but they are not able to infer the octant of θ_{23} i.e. we do not know whether θ_{23} is greater or less than its maximal value ($\theta_{23} = 45^0$). Determination of the octant of θ_{23} in the regime of earth matter effects using atmospheric neutrino source is another important goal of ICAL.

- **CP violation in leptonic sector:** The last unknown parameter of the PMNS mixing matrix, which is yet to be discovered is the Charge-Parity (CP) violating phase δ_{cp}. The matter effects in the neutrino oscillations are sensitive to the sign of Δm^2_{32} and depend on the Dirac CP violating phase δ_{cp} . So, a measurement of δ_{cp} will improve

the sensitivity of the determination of the sign of Δm^2_{32} and hence, neutrino mass hierarchy.

- **Other issues:** Apart from the above listed main goals, there are some other physics issues that INO-ICAL experiment has the capability to address; like
  - Determination of existence of sterile neutrinos.
  - To look for any non-standard effects beyond neutrino oscillations.
  - Search for new physics.
  - Search for magnetic monopoles.
  - Study of ultra high energy muons.

1.7.2 Why ICAL ?

Neutrinos are very weakly interacting particles with the crossection of about $10^{-43}\ cm^2$, therefore, their interaction rates are very very small. So, a large detector with dense target material is required to achieve statistically significant neutrino interaction events in a desired period of time. A 50 kton massive ICAL detector with iron target fulfill this basic criteria for a neutrino detector. Also, neutrinos and anti-neutrinos interact differently with matter, so it is important that the detector is able to distinguish them as well. The ICAL detector can do this job easily by identifying the bending of the track and charge of the muons produced due to neutrino interaction in ICAL through an applied magnetic field. The neutrino charge discrimination capability of ICAL will be of great use to solve the several current neutrino physics issues. A long muon track inside the calorimeter will be helpful in obtaining better energy and angular resolutions for ν events, so that the ratio of the length L traversed by the atmospheric ν before interaction and the energy E of the interacting neutrino event can be measured with better precision. The sinusoidal L/E dependence of P($\nu_\mu \rightarrow \nu_\mu$) will provide the direct evidence from the neutrino oscillation for atmospheric neutrino data. ICAL detector with iron target and glass resistive plate chambers is quite economical and comparable to other present neutrino detectors in the world in terms of performance.

The next few chapters will discuss the details of the ICAL detector along with Resistive Plate Chamber detector characterization and performance studies (Chapter 2), its ability to measure the muons and hadrons parameters (Chapter 3) and the physics sensitivity that can

be achieved for the precision measurement, mass hierarchy and octant measurement with ICAL detector (Chapter 4). Finally, we will discuss the results and future outlook of the ICAL detector in Chapter 5.

Chapter 2

The INO-ICAL Experiment

India's contribution in the field of neutrino physics started almost 50 years ago when in an underground laboratory at Kolar Gold Field (KGF), Indian scientists for the first time observed the atmospheric neutrino events coming from the cosmic rays interaction with the earth atmosphere [76]. It was a great discovery and a rare achievement which encouraged scientists to further research in the field of atmospheric neutrinos. However, KGF mines were closed down in around 1990's, and as a result, the neutrino research at this facility came to a full stop. After this sudden pause in the neutrino research, Indian scientists started to explore other possibilities including the construction of another neutrino observatory. As a result, the proposal of India-based Neutrino Observatory (INO) [1] as a multi-institutional collaboration was put forward to perform deep underground neutrino studies which has now been approved by the government of India. At present, a large number of institutions and universities from all over India are involved in the INO collaboration. This large collaboration is the first of its kind in the country and is expected to grow further.

In this chapter, we will discuss the salient features of INO facility and then provide a brief introduction of the various detectors including the Iron CALorimeter (ICAL) detector at this facility. Further, we provide a detailed description of RPC detector which act as an active detector element in ICAL and various efforts for its development and better performance. Finally, we show results obtained from the $R\&D$ on RPC detectors at our laboratory in University of Delhi.

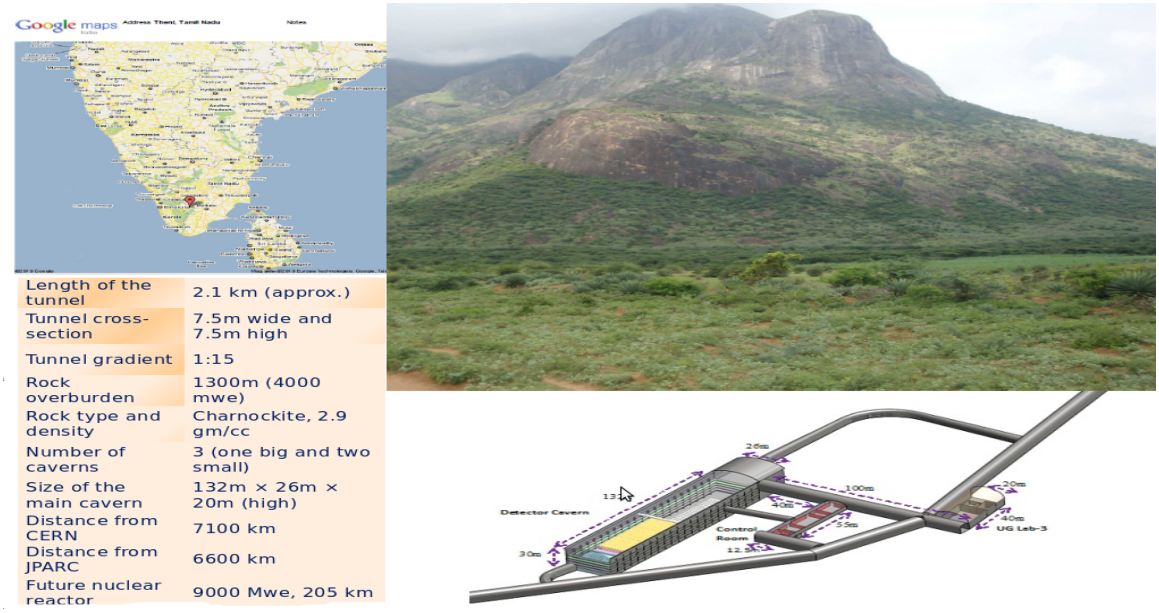

Figure 2.1: Bodi hill, location and schematic diagram of INO cavern with its specifications.

2.1 India-based Neutrino Observatory

India-based neutrino observatory (INO) [1, 2] is an approved project for an underground facility built to perform primarily the atmospheric neutrino searches in India. This project includes the construction of an underground laboratory and associated surface facilities at Pottipuram in Bodi West hills of Theni District in Tamil Nadu, India. It will have a large cavern of size 132 m $\times$ 26 m$\times$ 20 m to house a 50 kton magnetized ICAL neutrino detector and several small caverns to house smaller experiments like Neutrino less Double Beta Decay (NDBD) and dark matter searches at INO (DINO). The cavern will be protected from the cosmic background through a shielding of 1 km all around rock cover. The underground INO cavern can be accessed by a 2100 m long and 7.5 m wide tunnel. The schematic view of INO cavern and its location is shown in Figure 2.1. At present, INO has been dedicated for atmospheric neutrinos, but many long-term options are also open for it like the solar and supernova studies. In future, the ICAL can also be used as a far detector to detect neutrinos coming through beam shot out from an accelerator situated in Japan or CERN in Geneva.

Apart from the above mentioned facilities, a center for the operation and maintenance of the underground laboratory, human resource development and detector $R\&D$ will also be established at Madurai namely National Center for High Energy Physics.

2.2 The Iron Calorimeter Detector

The main detector at INO will be a large magnetized Iron CALorimeter (ICAL) neutrino detector. A schematic view of the ICAL detector is shown in Figure 2.2. ICAL is designed to study the properties of the atmospheric neutrinos and anti-neutrinos and to address several open questions discussed in Chapter 1. The ICAL detector will consist of three modules, each weighing about 17 ktons and of dimensions 16 m $\times$ 16 m $\times$ 14.5 m in x, y and z directions respectively. Each module will be a stack of 150 layers of alternate passive and active detector material. Horizontally placed Iron plates; each of thickness 5.6 cm will be used as the passive material and in between two successive iron plates there will be a gap of 4 cm to place the active detector material. In the first phase of ICAL experiment, which consists of building the first module, the Resistive Plate Chambers (RPCs) of dimension 2 m $\times$ 2 m, made up of glass plates have been chosen as active detector element. The RPC technology for later phases is still being explored through rigorous $R\&D$ all over the country. RPCs are basically a gas ionization tracking detector with good spatial and timing resolution. A detailed study on RPC working principles, construction, operation and $R\&D$ is presented in Section 2.2.2. The overall layout of the RPC detector is shown in Figure 2.3. The entire ICAL detector will be magnetized using a uniform magnetic field of approximately 1.5 T. This will help to distinguish the μ^- and μ^+ through their tracks bending in opposite direction inside the detector. By knowing the charge of muons, ν_μ and $\bar{\nu}_\mu$ events can be separated. This feature of ICAL makes it possible to determine the right mass spectrum of the neutrinos. Good tracking, energy and time resolutions, and excellent charge identification are key features of this detector. The ICAL detector specifications are listed in Table 2.1. The basic RPC units are placed in grid-format within the air gap, with a 16 cm horizontal gap between them, accommodating steel support structures in both x and y directions. Thus the iron structure for this detector will be self supporting with the layer above resting on the layer immediately below using iron spacers located every 2 m along the X-direction. The schematic of the design is shown in Figure 2.3. This will create 2 m wide roads along the Y-direction for the insertion of RPC trays. There will be a total of 8 roads per module in a layer. The whole detector, as described above, will be surrounded by an external layer of scintillation or gas proportional counters. This will act as a veto layer and will be used to identify muons entering the detector from outside as well as to identify partially confined events with the vertex inside the detector [1].

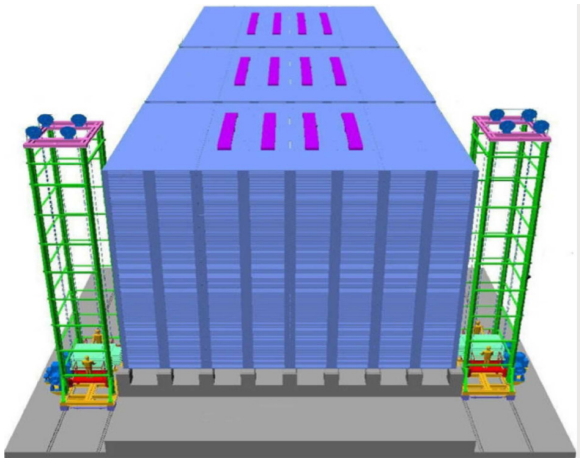

Figure 2.2: The schematic view of INO-ICAL detector.

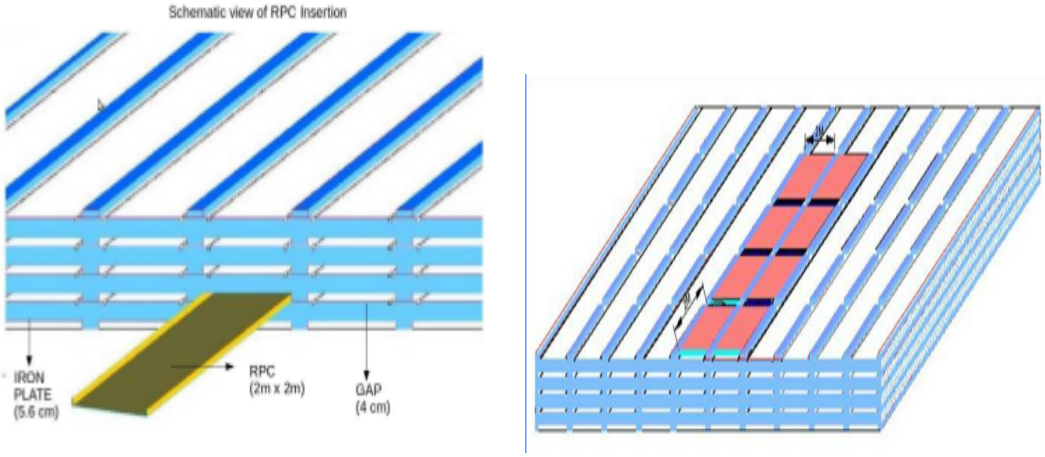

(a) RPC insertion scheme (b) Iron-RPC structural layout

Figure 2.3: RPC insertion methods and INO-RPC structural layout at ICAL detector.

ICAL Detector	
No. of Modules	3
Module Dimension	16 m $\times$ 16 m $\times$ 14.45 m
Detector dimension	48 m $\times$ 16 m $\times$ 14.45 m
No. of layers	150
Iron plate thickness	5.6 cm
Gap for RPC tray	4 cm
Magnetic field	1.5 Tesla
Total no. of RPC units	28000

Table 2.1: ICAL detector specifications.

2.2.1 The ICAL Magnet

The magnetic field causes charged particles to curve inside the detector, thus reveals their identity by charge identification and helps in detection of the particle. Using the curvature of the charged particle's track inside the magnetic field, the momentum of the particle can also be estimated. The precision of the momentum measurement depends on the magnetic field and in general it improves with increasing magnetic field. The geometry and structure of INO magnet has been designed with the specifications of the ICAL detector. The magnetized ICAL detector will consist of about 50 kton of low carbon steel. The steel plates in the proposed detector will be magnetized to a magnetic field of about 1.5 T by using toroidal shaped copper coils of height 15 m and width 8 m approximately. In the toroidal design, the copper coil goes through the rectangular slots in the stack of steel plates. The magnet for ICAL has been designed such that it can provide a uniform magnetic field inside and with minimal field leakage outside the detector for better performance. The ICAL magnet will have a modular structure as shown in Figure 2.4.

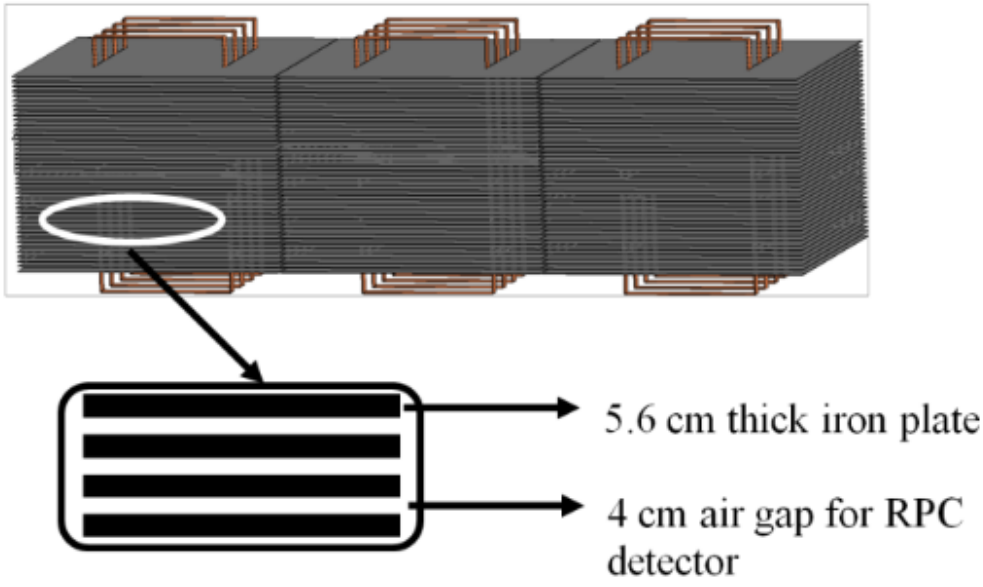

Figure 2.4: The design of INO-ICAL detector with copper coils in brown [78].

There will be three modules of the magnet for 50 kton steel which can be added further with the expansion of detector volume. The coil placement and schematic modular construction of ICAL detector is shown in Figure 2.5. Modular structure also provides the ease of maintenance and quick replacement of the coils in case of any damage. The design also

facilitates the insertion and removal of RPC trays from the side of the detector.

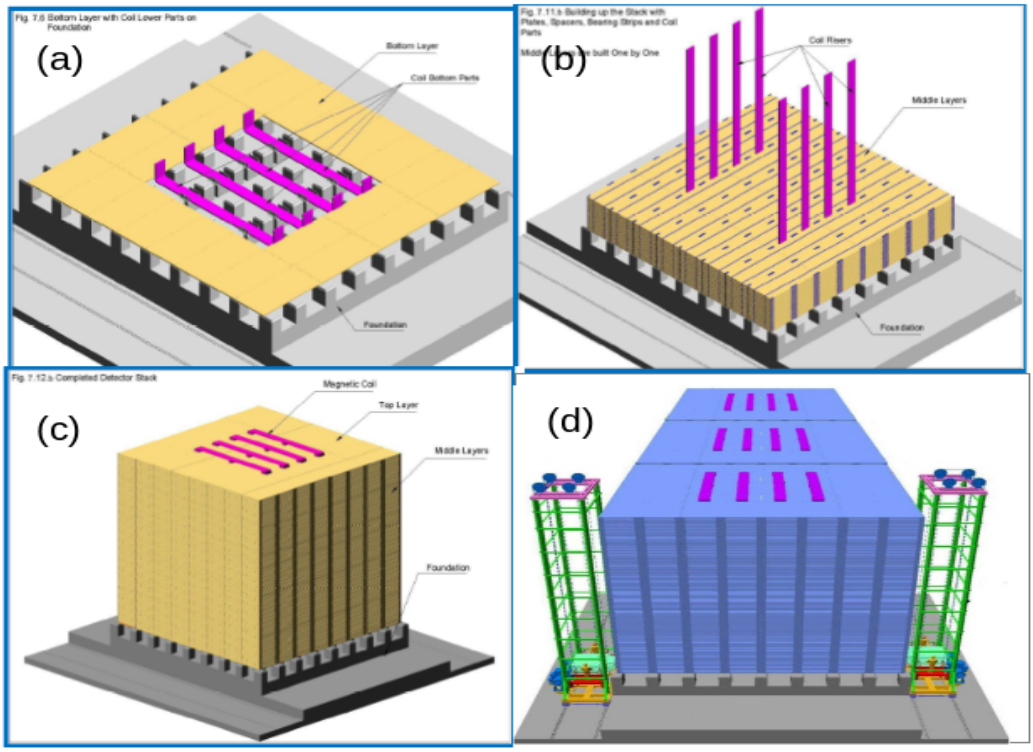

Figure 2.5: The schematic view of INO-ICAL detector detector construction with magnetic coils.

To study the magnetic-field distribution and its uniformity inside the detector, a detailed 3D electromagnetic simulation has been carried out with Magnet 6.0, Magnet software [77, 78]. To reduce the large computation time, simulation has been performed for a single iron layer of dimension 16 m $\times$ 16 m $\times$ 0.056 m. The magnetic field lines in a single iron plate in the central module are shown in Figure 2.6. The arrows denote the direction of the magnetic field lines while the length of the arrows and color shades indicate the magnitude of the field. The white circles and cross symbols show the outward and inward directions of current respectively. In the central region of each module, typical value of the field strength is about 1.5 T as obtained from simulations. From the magnetic-field distribution, it can be seen that field strength is low at four corners and at the middle (top and bottom) part of the plate (peripheral regions), whereas, a higher field is found in regions which have proximity to the coils. From this study, it is clear that there are variations in field strength at different parts of the iron plate which will ultimately affects the reconstruction of muon momenta and charge.

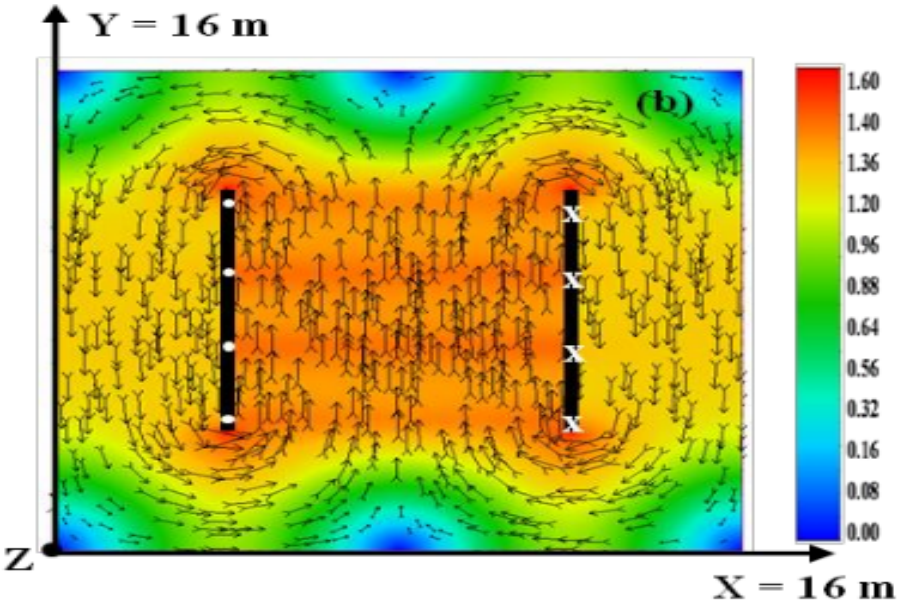

Figure 2.6: Magnetic field lines and their directions for magnet having continuous slots containing four coils at 20 kA-turns [78].

2.2.2 Resistive Plate Chamber

Resistive Plate Chambers (RPCs) [79, 80] are commonly and widely used particle tracking detector in high energy particle physics experiments such as BABAR [81], BELLE [82], OPERA [83] and experiments at LHC [84]-[86], as well as for many cosmic rays experiments. RPCs are of great interest due to their good efficiencies, high gain, moderate time and spatial resolutions with simple design, large coverage area and relatively lower cost. Good spatial and timing resolution make them well suited for tracking calorimetry such as ICAL. Generally, RPC is a gas ionization chamber made up of two high resistive parallel plates, a positively-charged anode and a negatively-charged cathode, and separated by a gas volume. It detects the signal generated in a thin gas volume between these two electrodes following the ionization produced by primary charged particles. These detectors are very simple to construct and are almost free from damaging discharges. Due to these important features, RPCs have been chosen as active detectors for the ICAL experiment at INO. As mentioned earlier that there will be a stack of alternate 150 layers of passive-active (Iron-RPC) material with a total weight of 50 kton ICAL detector. Therefore, a large amount of RPCs ($\sim$ 28,000) of dimension 2 m $\times$ 2 m are needed for the experiment.

2.2.2.1 RPC and its Working Principle

The Resistive Plate Chamber is a type of spark chamber with two parallel high resistive electrodes (glass or Bakelite) of thickness ($\sim$ 2-3 mm) and volume resistivity of around $10^{12}\Omega\ cm$. Two resistive electrodes are separated for a gas gap of 2 mm by means of highly insulated polycarbonate spacers as shown in Figure 2.7. Typically, the electrodes should have high resistivity to control time resolution, counting rate and preventing spread of discharge throughout the entire gas volume. Various studies have been performed on these properties and discussed in detail in Refs [79]-[94]. Button shaped spacers are used to maintain the gap at the central region while T-shaped spacer are used to lock the side spaces of the RPCs. A suitable gas mixture is circulated through the gap and an appropriate uniform electric field is applied across the electrodes through a conductive coating (usually graphite coating) on their outer surfaces. The gas mixture is required for the multiplication of charge (streamer mode) produced when some ionizing particle passes through the gas volume. Due to high resistivity and quenching characteristics of the electrodes, the discharge is limited to a tiny area of about 0.1 cm^2. This discharge induces an electrical signal. The electrical signal induced by the passage of the charged particle is detected through the external pickup strips, placed orthogonal to each other, above and below the electrodes. Thus, RPC detector has an ability to provide two dimensional (X and Y) readout at a time. It can be used to record location and time of ionization. The discharge area recharges slowly through the high resistivity glass plates and recovery time is about 2 sec, detector remains insulating during this period. The basic structure of a RPC is shown in Figure 2.7 followed by a view of the specifications of different parts.

RPC can be operated either in streamer (discharge mode) or in avalanche mode. In avalanche mode, charged particles passing through the gaseous medium produce primary ionization. These ionized particles are accelerated by electric field thus producing secondary ionization by colliding with the gas molecules. This avalanche stops as the external field opposes the internal field due to ionization and the charged particles get collected on the respective electrodes. This is shown schematically in Figure 2.8. This mode operates at a lower voltage and typical pulse amplitudes are order of $\sim$mV are generated, hence external amplifiers are required to readout the signal. In the streamer mode, the avalanche generated is followed by a streamer discharge. The secondary ionization continues until there is a breakdown of the gas and a continuous discharge takes place. This mode operates at a higher voltage and also results in high gain. Typical pulse amplitudes are of the order of 100-200 mV. The electric field inside the gap is kept intense enough to generate limited

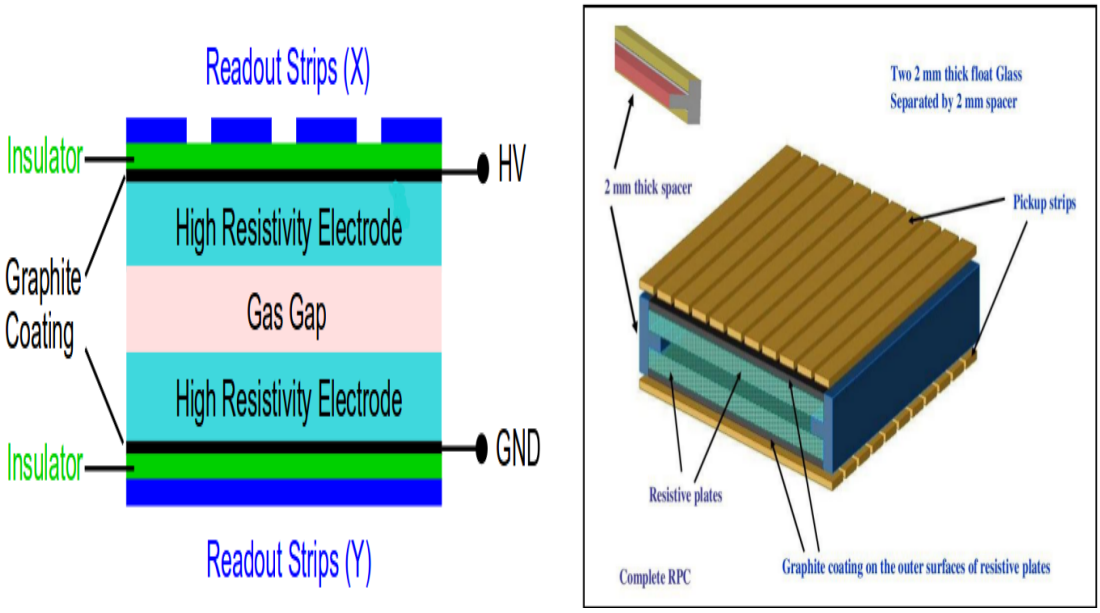

(a) Basic design of Resistive Plate Chamber. (b) Schematic diagram of ICAL-RPC.

Figure 2.7: Resistive Plate Chamber design

discharge localized near the crossing of the ionizing particle. As the streamer signals are quite large (between 50 pC and a few nC), no pre-amplification is needed and the signals can be discriminated directly. Thus the read out of streamer mode RPCs is quite simple [87, 88]. Figure 2.9 shows schematic images of the streamer development in the gas gap. Due to the relatively long relaxation time of the resistive electrode, this mode is adequate for cosmic ray and low-rate accelerator experiments. The counting rate capability of RPCs is significantly improved if the occurrence of streamers is suppressed and the detector is operated in avalanche mode [89]. This can be achieved by the addition of small contents of SF_6 to the gas mixture [90]. Hence, RPCs operated in avalanche mode will be used for the muon trigger system at INO-ICAL detector.

Figure 2.10 shows the equivalent circuit of glass RPC module. At low voltages, the gas mixture is insulating and the primary ionization's in the gas gap do not develop avalanche. In this case, an infinite resistance is provided by the gas gap and, therefore, the current passing through the chamber is determined by the spacers resistance only. At high voltages, the gas mixture is shorted out because of the discharge and gas mixture acts effectively as a conductor. As a result, the effective voltage is applied on the glass electrodes which results in a higher current. The current flowing through the chamber in this case is determined by

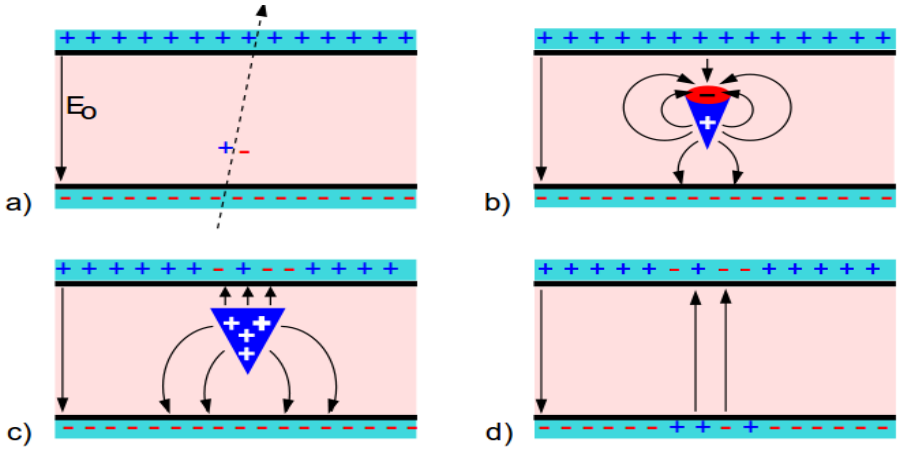

Figure 2.8: Avalanche mode operation of Resistive Plate Chamber (RPC).

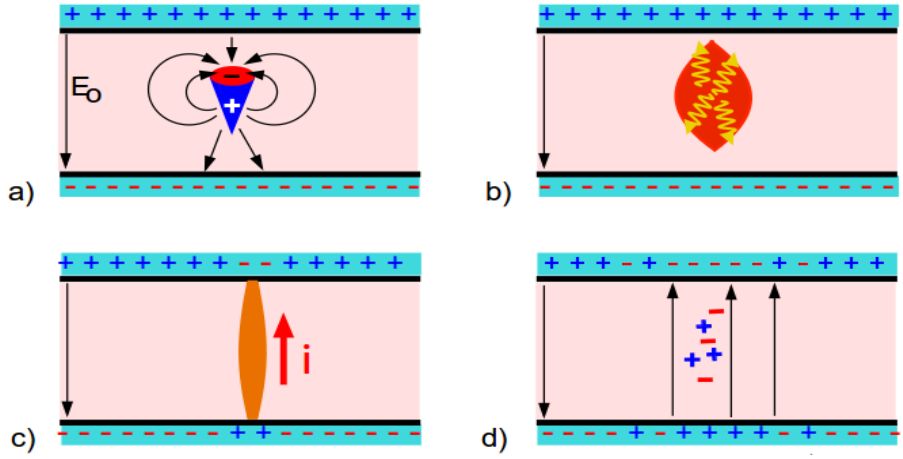

Figure 2.9: Streamer mode operation of Resistive Plate Chamber (RPC).

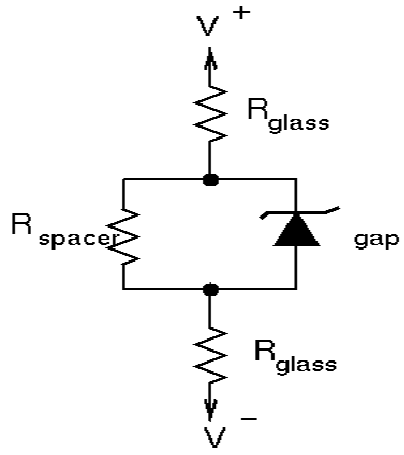

Low voltage

$$R_{gap} \approx \infty$$

$$\frac{dV}{dI} = R_{spacer}$$

High voltage

$$R_{gap} \approx 0$$

$$\frac{dV}{dI} = R_{glass}$$

Figure 2.10: Electrical circuit diagram for a RPC module.

the resistance of the glass.

2.2.2.2 Choice of Gases and Gas Mixture

In order to produce an electrical signal of sufficient amplitude, an avalanche multiplication is essential in all gaseous detectors. In principle, all gases can be used for generating electron avalanches in presence of enough electric field. However, depending on the mode of operation and the specific requirements for the chamber e.g. signal proportionality, high gain, good drift properties, or short recovery time, limits the choice of gases or gas mixtures. Generally, the noble gases are preferred as they require low electric field intensities for avalanche formation. The gas mixture plays an important role in the functioning of a RPC. It fixes the working mode of the RPC in avalanche mode or in streamer mode, resulting in different characteristics and performances. The first ionization potential, the first Townsend co-efficient and the electronegative attachment co-efficient determines the avalanche multiplication, the presence and the relative importance of photo production and the saturated avalanche range to the streamer mode.

The filling gas is usually composed by an optimized mixture. To work in the streamer mode the main components should provide a robust first ionization signal and a large avalanche multiplication for a low electric field. One typical element can be Argon, because of its higher ionization energy and low cost, which ensures that a greater avalanche increases with electron abundance, good situation to start the streamer mode. To work in an avalanche mode the main components could be an electronegative gas, with high primary ionization but with small free path for electron capture. The high electronegative attachment co-efficient limits the avalanche electron number. Tetrafluroehtane (known as Freon), is widely used for this purpose. But here we use R134A (as Freon) which is Eco-friendly. One more component is constituted by polyatomic gases, often Hydrocarbons, which have absorption probability for ultra violet photons, produced in electron-ion recombination. This gas is known as quenching gas. In our gas system we have used Iso-Butane as quenching gas. Finally we use SF_6 (sulfur-hexafluoride) to control the excess number of electrons. A small quantity of SF_6 in a few fraction of the standard gas mixture could enlarge the pure avalanche mode operating voltage range up to 1 kV streamer free plateau.

2.3 RPC Detector $R\&D$

The INO-ICAL experiment will use RPCs as the active detector elements. Their high gain, simple design and low cost make them favorite to construct about 28,000 detectors of dimension, 2 m $\times$ 2 m, that INO-ICAL need. The experiment is planned to operate at least for 20 years and may also be upgraded to 100 kton in later phases. Because of the huge number of detectors required for INO-ICAL and keeping in mind the long life span of the experiment, it is pertinent to perform a vigorous $R\&D$ to carefully optimize the various detector design and operational parameters like the electrode material, gas composition, operational conditions, etc. to exploit fully all the advantages of the RPC detectors.

In the first phase of ICAL detector, RPCs made up of glass electrodes have been chosen for the active detector. Since INO-ICAL experiment is going to construct huge number of RPCs which in turn requires a large amount of the electrode's material, therefore, one factor that also becomes very important in the selection of electrodes is the ease of availability of it at a reasonable cost. Keeping in view, the huge quantity of glasses required and the complexity involved in its long distance transportation, we decided to pursue our $R\&D$ on the glasses and Bakelites available locally. We selected three types of glass *viz*., Saint Gobain, Asahi and Modi and two types of Bakelites *viz*., Formica and Hylam which are easily and readily available in the local market at a reasonable price for our $R\&D$.

2.3.1 Electrode Compositions

Electrode material of a RPC plays an important role in the functioning of the detector. In RPC detectors, material properties of electrodes and environmental factors play a significant role in detector working. The two parallel plate should be resistive enough to control the time resolution, counting rate and to prevent the spreading of discharge. The bulk resistivity ρ of the electrode plates should be optimized according to the required rate capability, which is strongly dependent on it. It must also have uniform surface to avoid localization of excess charge and to prevent alternating leakage path for post streamer recovery. Also, a better time resolution can be achieved with smooth surface electrode of the detector. Therefore, surface treatment of the electrodes need to be done carefully. We have performed various characterization studies of above mentioned glass and Bakelite electrodes in order to find the best among all of the samples for INO-RPC; which are described below:

2.3.2 Bulk and Surface Resistivity Measurements

The bulk and surface resistivity (volume resistivity) are important parameters for the detector operation. The time resolution, counting rate, leakage current and aging issues of detector performance highly depends on these electrical properties of electrodes. Therefore, we determine the electrical properties such as bulk resistivity and surface resistivity of different glass and Bakelite electrodes. The bulk resistivity of the electrode material of the RPC has been determined through the measurement of current through the electrode for a given bias voltage. Figure 2.11(a) shows the circuital diagram for bulk resistivity measurement. Two cables are soldered on the copper plates and connected to the CAEN N471A high voltage power supply. The copper plates are placed on the adjacent flat surfaces of the electrode sample and a bias voltage has been applied across it. The current measured by the inbuilt ammeter inside CAEN N471A power module, is noted down as a function of the applied voltage. The voltage drop across the resistance has been measured as a function of the applied voltage.

For the surface resistivity measurement, a circuit has been developed with two heavy brass bars with soft padded conducting edges at the bottom, which are placed on the test sample as shown in Figure 2.11(b). This type of heavy jig provides a good surface contact with the electrode which in turn makes reliable measurements. The length of the brass bars and their separation are kept at 5 cm. A DC bias voltage applied on the jig and the leakage current across the terminals of the jig through the sample is measured. The resistance, R of a surface film of thickness, t, as measured between two conductors of length, L and separated by width, W is proportional to $L/(W \times t)$. So for a given square of side, L (which is equal to W) R is independent of L (and W) and depends only inversely on t. The jig essentially consists of two conducting bars fixed in frame so as to form a square. Provision is made to measure the resistance across these conducting bars, using a multimeter. The resistance value is directly read as $\Omega/\square$. Jigs of small and big squares were fabricated so that the resistivity measurements on both fine and coarse length scales could be made.

2.3.2.1 Bulk and Surface Resistivity of Glass Electrodes

For bulk resistivity measurement, glass samples of dimension 3 cm $\times$ 3 cm have been taken. Figure 2.12 shows the bulk resistivity of the three types of glasses as a function of the applied bias voltage. The Saint Gobain glass has been found to have the maximum bulk resistivity among all the three samples. In the operating region around 6 kV, the bulk

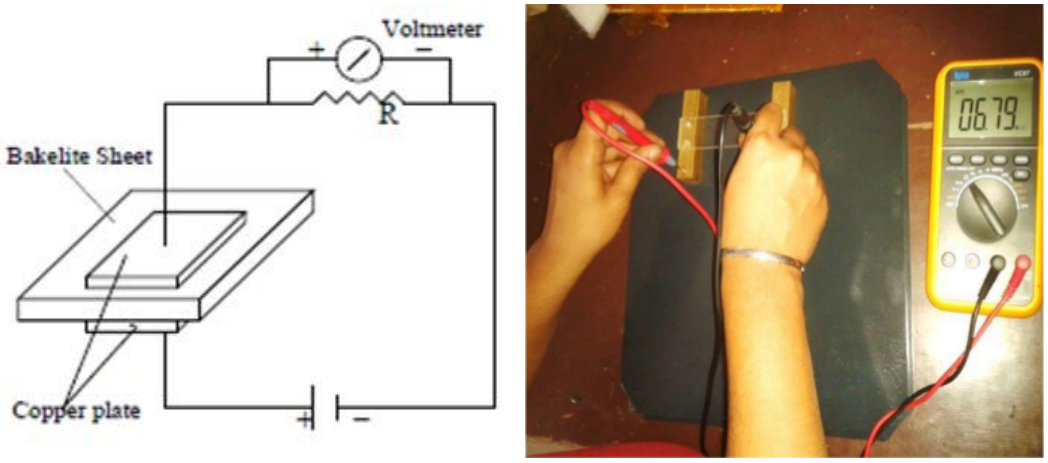

(a) Bulk resistivity (b) Surface resistivity

Figure 2.11: Setup for Bulk and surface resistivity measurements.

resistivity of Saint Gobain is of the order 5×10^{12} Ω-cm on average. Asahi and Modi are found to be having similar bulk resistivity and is approximately 1.5×10^{12} Ω-cm in the operating region around 5 kV. The bulk resistivity measurements are repeated many times and the results varied within less than 5% from the mean values.

For surface resistivity measurement of glass plates, a total of 10 measurement points are taken on each plate to obtain a fine binning. Also, the measurements are repeated many times and it is found to be agreeing within 6%. Figure 2.13 shows the average surface resistivity measurements of the three glasses. From this figure it can be seen that the surface resistivity of the Asahi glass is approximately constant over most of the surface area whereas there are significant variations in the surface resistivity distribution of the Saint Gobain glass. The Modi glass has even wider surface resistivity variations. From the scale of surface resistivity variations of the three glasses, it can be concluded that the Asahi glass is having the smoothest surface of all, followed by Saint Gobain and Modi respectively [93].
Theses measurements of bulk and surface resistivity are performed under standard pressure, relative humidity maintained between 45% to 49% and temperature between 19° C to 21°C.

2.3.2.2 Bulk and Surface Resistivity of Bakelite Electrodes

The measured bulk resistivity of Formica and Hylam Bakelite as a function of voltage is shown in Figure 2.14. We found that Bulk volume resistivity of Formica electrode is

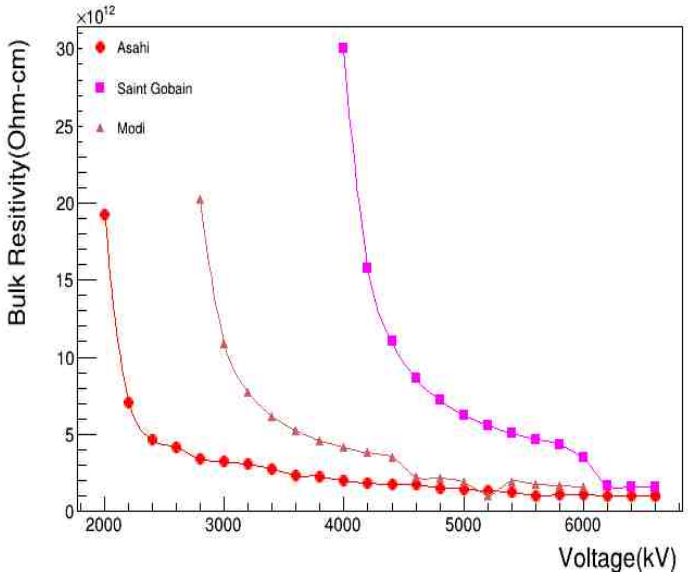

Figure 2.12: Bulk Resistivity of all the three types of glasses in Ω-cm as a function of the applied voltage.

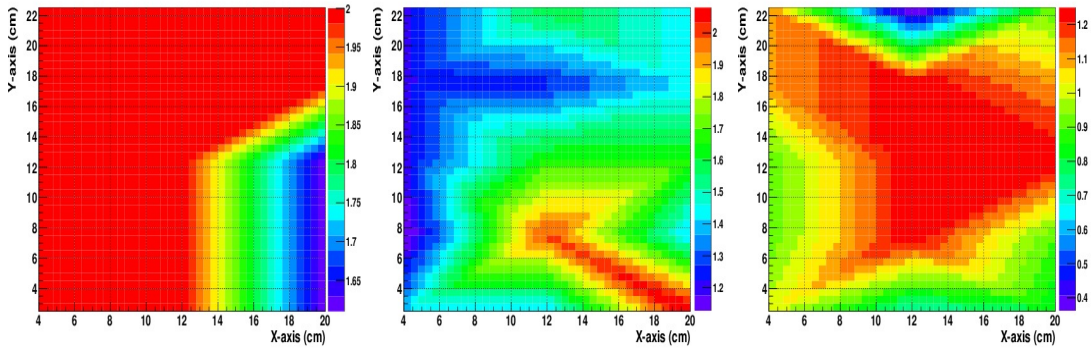

(a) Asahi (b) Saint Gobain (c) Modi

Figure 2.13: Surface resistivity for all the three glasses. The X and Y axes are the length and breadth in centimeters of the glass plate whose surface resistivity has been measured. The intensity of the colors indicates the value of the surface resistivity in $10^{11}\Omega/\square$ and the variation in colors represents the variation in the surface resistivity at different points across the glass plate.

$2.7 \times 10^{10}\ \Omega\ cm$ and for Hylam it is $4.7 \times 10^{10}\ \Omega\ cm$.

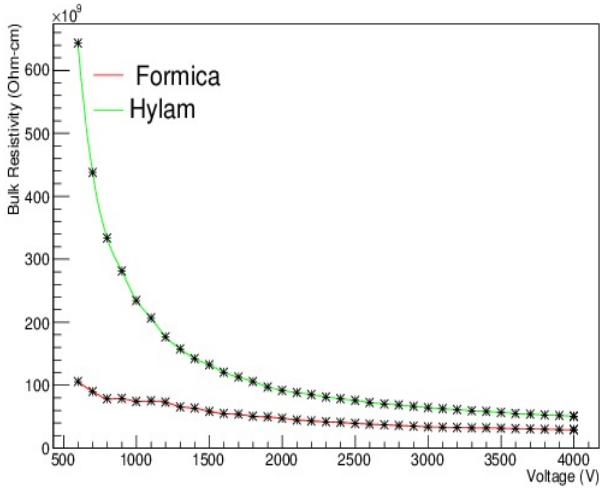

Figure 2.14: Bulk resistivity of Formica and Hylam Bakelite as function of applied voltage.

The surface resistivity of the Bakelite sheet is measured using jig method as mentioned in Section 2.3.2. The brass bars, forming the opposite sides of a square shape, are mounted on epoxy plates. The length of brass bars and their separation are kept 3 cm. A DC bias voltage has been applied on the jig and leakage current across the terminals of jig through the sample has been measured. Figure 2.15 shows the surface resistivity measurement of the Formica and Hylam Bakelites.

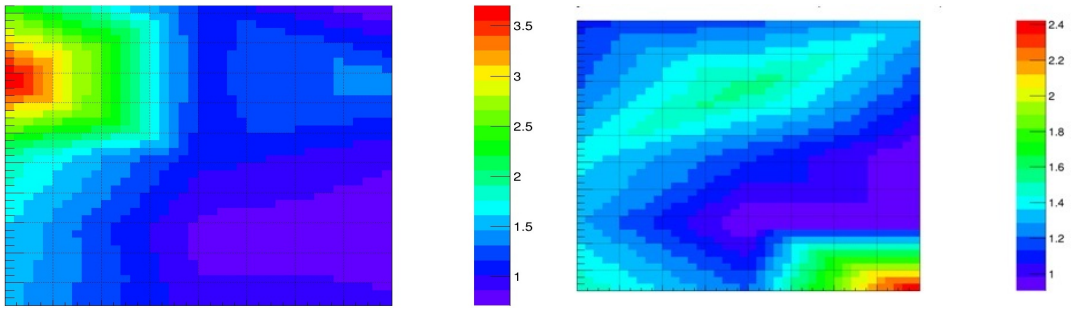

(a) Formica (b) Hylam

Figure 2.15: Surface resistivity contour plots for (a) Formica and (B) Hylam Bakelites. The X and Y axes are the length and breadth in centimeters of the electrode whose surface resistivity has been measured. The intensity of the colors indicates the value of the surface resistivity in $10^{11}\Omega/\square$ and the variation in colors represents the variation in the surface resistivity at different points across the Bakelite plate.

2.3.3 Surface Properties

Uniformity of the surface texture is important to control the increase in dark current, counting rate and thus influencing the efficiency of the detector. The rough inner surface of the electrodes may cause wide variation in the electric field inside the RPC. Due to rough surface, the sharp uneven edges in the surface morphological structure causes the non uniform electric field inside the RPC. Rough surface is very sensitive to the field emission which is a source of high dark current and high counting rates. Therefore, it is very important to perform a panoramic study of surface roughness for the efficient operation of the RPC. We use Scanning Electron Microscopy (SEM) and Atomic Force Microscopy (AFM) techniques to determine the the smoothness (roughness) of the electrodes surface. The average roughness is defined as:

$$R_{av} = \sqrt{\frac{\sum_{i}(t_{av} - t_i)^2}{N}} \tag{2.1}$$

where, t_{av} is the average height, t_i is the individual measured height and N is the number of data points scanned on the surface. The other surface properties like the crystalline or amorphous nature of the material has been detected with the help of X-Ray Diffractometer (XRD) measurement. The optical properties of the electrode surface have been determined with the help of Ultra Violet (UV) transmittance/reflectance studies.

2.3.3.1 Surface Properties of Glass Electrodes

AFM images taken from multimode AFM instrument is shown in Figure 2.16 for all the three glass samples. The average roughness of 1.28 ± 0.33 nm, 2.00 ± 0.96 nm and 2.81 ± 1.56 nm is found for Asahi, Saint Gobain and Modi respectively. The SEM images for the three glasses are shown in Figure 2.17. The SEM images are taken from ZEISS MA15 instrument at 20 kV using common electron beam. The AFM and SEM measurements alone are not conclusive enough to declare any sample as smoother than other with high confidence, however, after taking into account the surface resistivity results together with the AFM and SEM measurements, we can conclude that, at least, qualitatively Asahi glass appears to have the smoothest surface of all. Since these results are not conclusive enough quantitatively to reject any of the three glass samples at this stage, we proceeded to fabricate the RPCs using all the three samples to perform the characterization studies. To confirm that the glasses which we have selected are amorphous in nature, we performed an X-ray diffractometer scan with REGAKU D-2000 instrument with acceleration voltage of 40 kV,

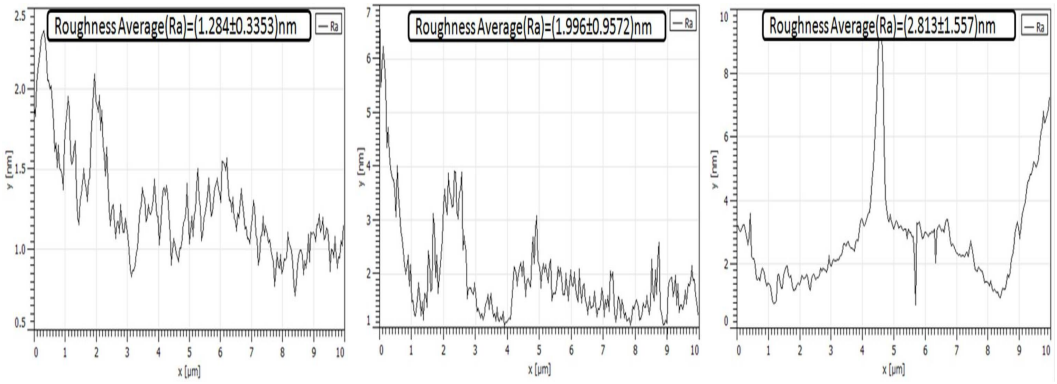

(a) Asahi (b) Saint Gobain (c) Modi

Figure 2.16: Atomic Force Microscopy scans for the three glass samples. The X-axis shows the scanned length of the glass sample in μm, and Y-axis shows the variation in the surface roughness (or smoothness) in nm.

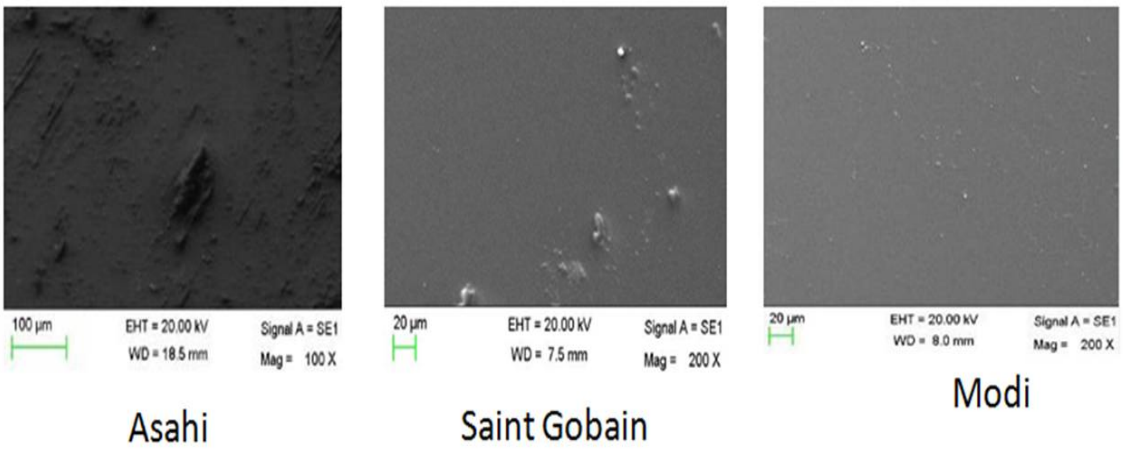

Figure 2.17: Electron Microscopy scans for the three glass samples.

current of 100 mA, and $Cu - K\alpha$ as an X-ray. The diffraction data has been acquired with a step of 0.02° and sampling time of 4 seconds is applied for each glass sample. Figure 2.18 shows the results of the XRD scan. The XRD study confirms molten glassy type matrix for all the samples. We also performed the study for the determination of the composition percentage of elements present in electrode samples. Carbon, Sodium, Magnesium, Aluminium, Silicon, Calcium, Oxygen and Tin have been found in different quantity in the three glasses. The detailed composition is given in Table 2.2. It can be seen from the table that Saint Gobain glass has no Carbon component whereas Asahi and Modi have 4.89% and 6.68% Carbon respectively. Since Carbon is a conducting element so absence of it from the Saint Gobain glass could be one of the reasons for its high bulk resistivity compared to Asahi and Modi.

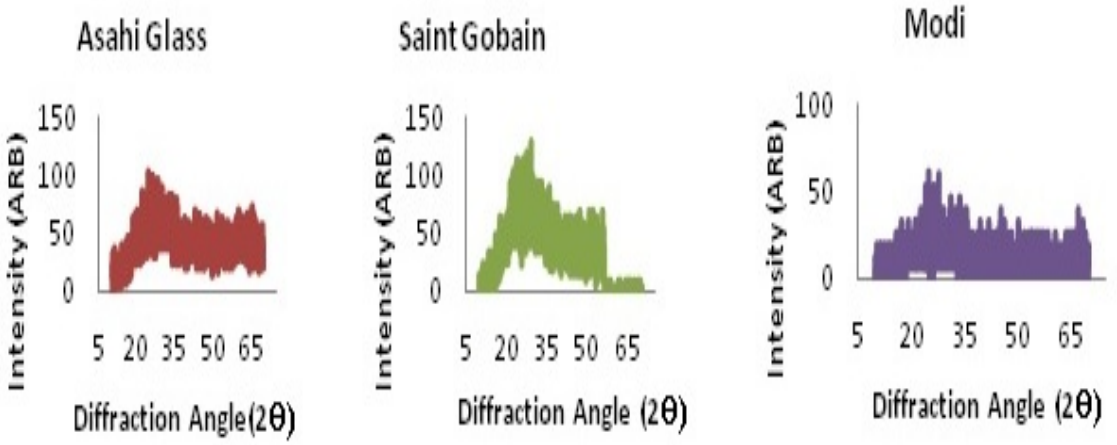

Figure 2.18: XRD studies for the three glass samples.

Serial No.	Element Name	Percentage of Elements		
		Asahi	Saint Gobain	Modi
1	C	4.89	-	6.68
2	Na	6.89	8.22	6.34
3	Mg	1.79	1.85	1.55
4	Al	0.32	0.27	0.31
5	Si	21.7	24.56	20.44
6	Ca	2.71	3.32	2.45
7	O	61.67	59.97	61.99
8	Sn	-	0.58	-

Table 2.2: Element composition in the three glass samples in atomic weight percentage.

For selecting the smoother surface out of the two sides of the electrodes, we also performed the reflectance test on Perkin Elmer Lamda 3B spectrophotometer between λ range 0 - 1200 nm. The results from the reflectance measurements are shown in Figure 2.19. The reflectance test shows that Saint Gobain has the maximum reflectance power of roughly 94% whereas Asahi is slightly less. Modi is having the least reflectance capability.

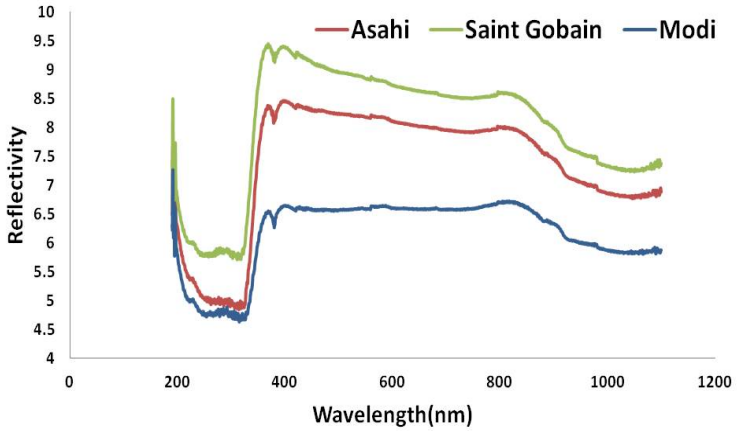

Figure 2.19: Reflectance measurements for the three glass samples.

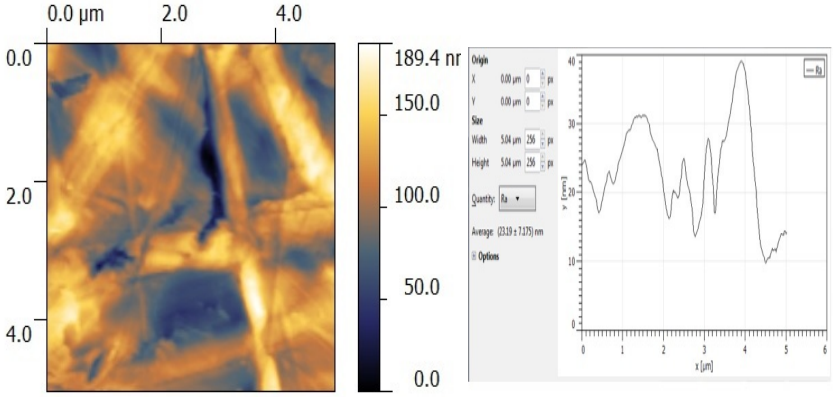

Figure 2.20: Results of AFM study Formica with silicon coating.

2.3.3.2 Surface Properties of Bakelite Electrodes

We know that the Bakelite available from market generally do not have very smooth surfaces. Therefore, to make inner surface of Bakelite smoother a thin silicon coating has

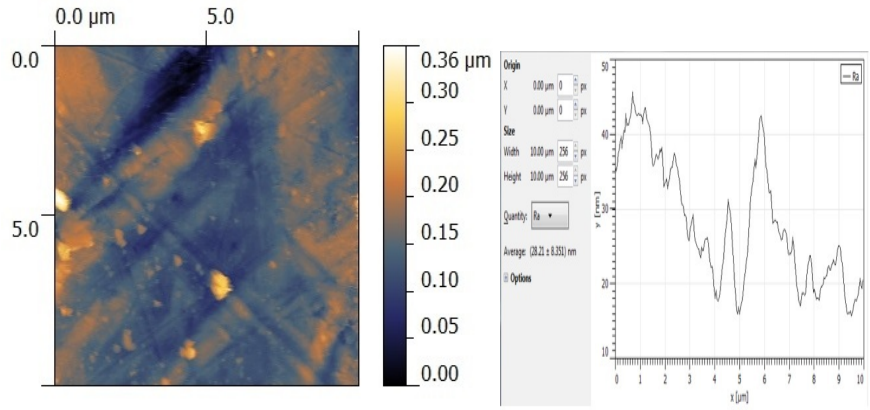

Figure 2.21: Results of AFM study Formica without silicon coating.

been applied to both the Bakelite samples. AFM studies has been performed separately for Formica Bakelite with silicon coating (see Figure 2.20) and without silicon coating (see Figure 2.21). From AFM studied it is found that after silicon coating, the surface roughness is decreased and the surface quality is improved, which has profound effect on the detector performance.

2.3.4 Construction of Bakelite and Glass RPC Chambers

Using three different types of glasses and two types of Bakelite electrodes mentioned in the previous sections, we fabricated small prototypes RPCs of 30 cm $\times$ 30 cm dimensions in our lab. Fabrication of a RPC has been done by following the steps given below:

- **Electrode Cutting and Cleaning** : Each electrode of thickness 3 mm is cut in the appropriate size (30 cm $\times$ 30 cm) and the four corner edges are chamfered by a jig of right dimension to make a correct 45^0 angle as shown in Figure 2.22(a). The electrodes are then cleaned with water, alcohol followed by labolene and distilled water. The edge spacers and polycarbonate button spacers are also cleaned with alcohol. The glass edges are taped over with masking tape with 1 cm being masked or taped off on each side so as to prevent the conductive coating to be painted right up to the edge of the glass to avoid the leakage of high voltage through the edge spacers.

- **Conductive Coating**: Each electrode is then coated with graphite to improve the conduction all over the electrode surface as shown in Figure 2.22(b). This coating is used for the uniform application of high voltage over the area of the RPC and to

increase the conductivity of the glass. Graphite coating is essential for the localization of charge produced by the passage of charged particle. Uniform resistivity of the coating across the surface of the electrodes plays an important role in the RPC performance. If the surface resistivity of the graphite coat is too small, the induced charge is less localized and spreads laterally across the graphite coat, producing large cross-talks between the pickup strips and thus severely affecting the position resolution of the detector. It has been observed that the cluster size of an RPC exponentially decreases with the surface resistivity of its electrode coating and a thin coat with surface resistivity of 0.1 - 1 $M\Omega$ results in time constants that are comparable to the charge movement duration [96, 97].

We used graphite paint made up of colloidal grade graphite powder (3.4 gm), Duco-lacquer (25 gm) and Duco-thinner (40 ml) and sprayed on the glass electrodes using an automobile spray gun to obtain the uniformity of the surface with a surface resistivity of about 1 $M\Omega$. Once the surface is coated, the masking tape is removed and the resistivity of both surfaces is measured using a resistance measurement as mentioned in Section 2.3.2.1.

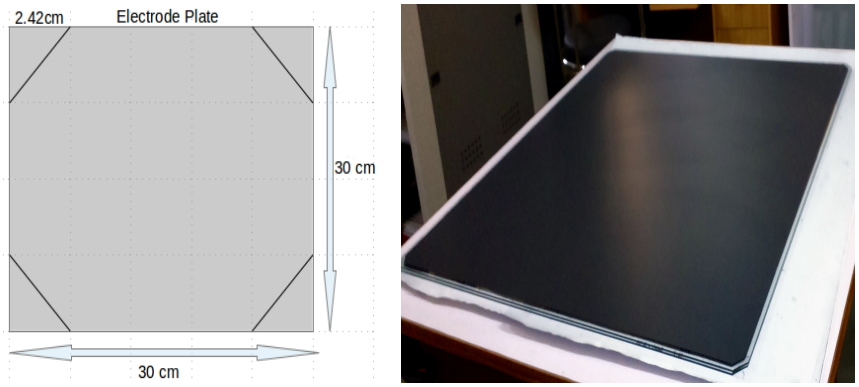

(a) RPC cutting scheme (b) Electrode with graphite coating

Figure 2.22: Schematic view of edge cutting of glass plate of dimension 30 cm $\times$ 30 cm and a sample glass electrode with graphite coating.

- **Gluing of Glass**: To maintaining the gas gap between two electrodes, we used three types of spacers made up of polycarbonate material as shown in Figure 2.23(a). Buttons spacers of size 2 mm are glued on the electrode surface in a square array on the surface without the graphite coating (see Figure 2.23(b). They provide a precise and uniform gap separation between the two electrode plates. Then the other glass

plate facing the non-coated surface down wards is placed on this array of spacers thus obtaining required gas gap. The electrodes are then glued from each side of four edgers using polycarbonate side spacers as shown in Figure 2.23(c). A gas inlet and a gas outlet nozzles made up of polycarbonate are glued on the diagonally opposite corners of each gap. An epoxy adhesive glue has been used to seal the chamber. The setup is left for 12 hours for glue to dry.

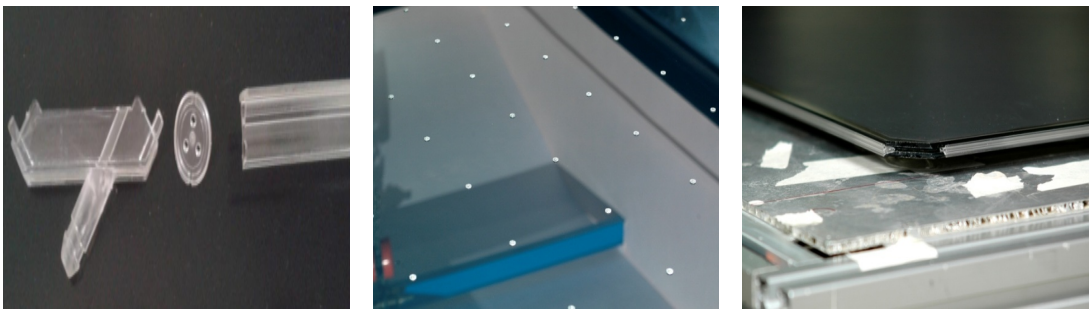

(a) Nozzle, button and side spacers (b) Electrode with button spacers (c) Side spacers fitting

Figure 2.23: RPC spacers and their fitting.

- **Leak Test:** To ensure against the gas leak (especially at the glued joints), a test is done using manometer technique by measuring the pressure difference (water level difference in both arms of manometer) with respect to time. Re-gluing is done on the edge spacers wherever a gas leak is detected. Figure 2.24 shows the gas leak test of RPC using manometer technique.

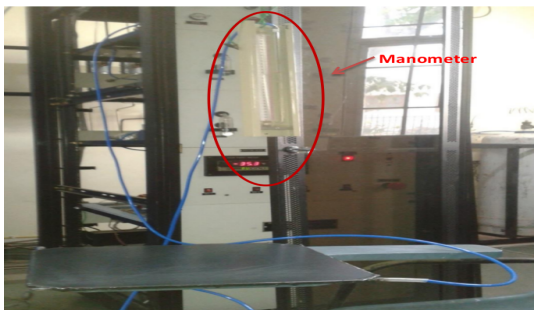

Figure 2.24: Gas leak test of RPC using manometer technique.

- **High Voltage (HV) supply:** The high voltage is applied to the graphite layer through a copper tape sticked on the electrodes. HV wires are then soldered on to this copper

tapes. Positive voltage is applied to one side and an equal negative voltage to the other side, using a bi-polar high voltage DC supply, so that both see a common ground. The bi-polar connection is better than the unipolar since each glass surface sees only half the total voltage, thus decreasing the chances of HV leaks. We used HV modules (like CAEN N417A) and HV carrying cables and SHV connectors for power supply connection.

- **Pickup Strips:**- For signal readout, copper strips of width 2.80 cm with an adjacent separation of 2 mm are mounted on honey comb panel are placed orthogonally above and below the sealed chamber, and then packed in an aluminium case for proper grounding. Honeycomb panels are light weight and provide adequate mechanical strength. Each copper strip is terminated with a 50 Ω impedance to match the characteristic impedance of the strip. A layer of mylar sheet is placed between the graphite layer and the pickup panel to provide insulation. Figure 2.25(a) shows the pickup panels mounted over the honeycomb.
  A picture of completely assembled RPC following the above mentioned steps is shown in Figure 2.25(b).

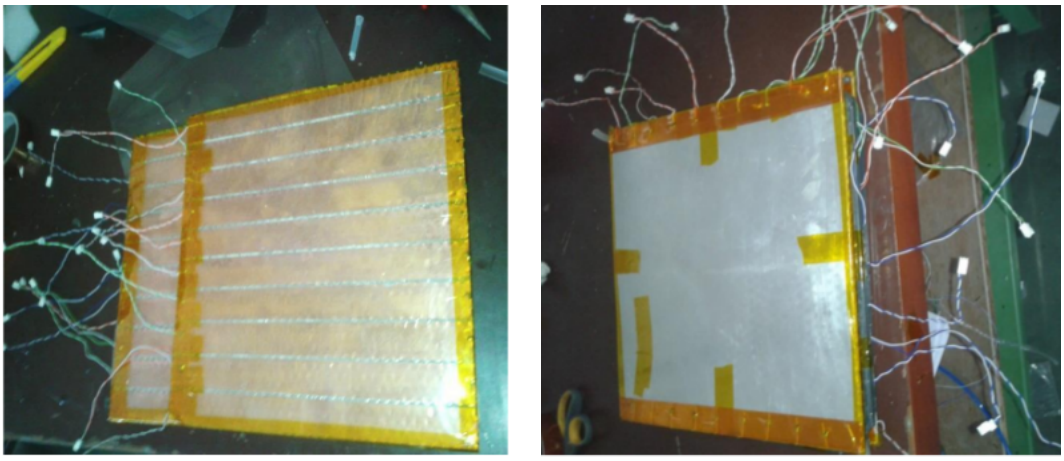

(a) Copper pick up panel (b) A complete RPC module

Figure 2.25: Copper pick up strips with the plastic honeycomb base used for RPC fabrication and an assembled RPC of dimension 30 cm $\times$ 30 cm.

2.4 Gas Mixing Unit & Calibration

As mentioned in Section 2.2.2.2, gas mixture plays an important role in the characterization and functioning of the resistive plate chamber. For the RPC performance studies, we use mixture of Freon (R134a), Isobutane (C_4H_{10}) and SF_6 gases in different proportions. Freon is used as primary gas for ionization, Isobutane is used as quenching gas while SF_6 is used to control the excess number of electrons. For proper and efficient working of RPCs, it is required to premix individual gases in appropriate proportion and also control the flow in the detector. This is done with the help of gas mixing and distribution system. A gas mixing unit capable of mixing four individual gas components and control the mixed gas flow through the detector has been designed and developed with the help of local industry [95] as shown in Figure 2.26. This mixing unit serves to control the flow rate of gas using

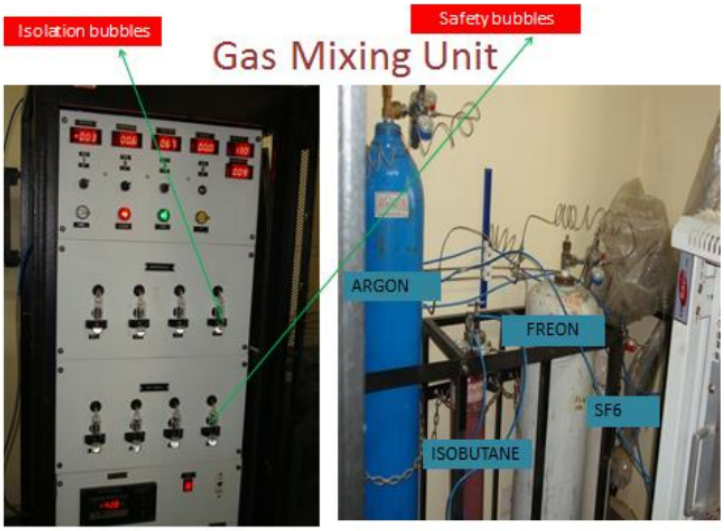

Figure 2.26: Four channel gas mixing system and gas cylinders at Delhi University lab.

Mass Flow Controllers (MFC) and maintains the pressure in the RPC detector with the help of safety and isolation bubblers. Safety bubblers of borosilicate glass take care of the back pressure and protect the RPCs from possible damage due to over pressure whereas the isolation bubblers serve to prevent back diffusion of air into the RPC. To avoid the situation of over pressure, these bubblers have been made in such a way that gas should not bubble through safety bubblers and there should be continuous bubbling in the isolation bubblers. The presence of bubbles in the safety bubbler and absence of them in isolation bubbler indicates the problem of gas leakage and over pressure.

Before using the gases for the RPC performance studies, flow rate of each gas provided

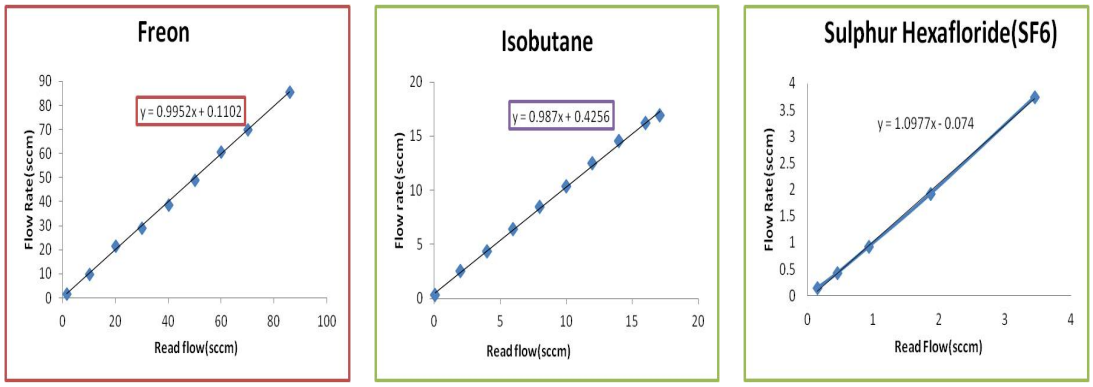

(a) Freon calibration (b) Isobutane calibration (c) SF_6 calibration

Figure 2.27: Mass Flow Controller (MFC) calibration of gas mixing units for Freon, Isobutane and SF_6 gases.

by the MFCs of the Gas Mixing Unit (GMU) has been calibrated to ensure that GMU is working properly. MFCs are used to measure and control the flow of gases. The MFCs of gas mixing unit are calibrated to control a specific type of gas at a particular range of flow rates. For this calibration, water displacement method has been adopted. In this method, we check the displacement of water level caused by the gas which has to be calibrated using a volumetric burette. For a given set flow of the gas provided by GMU, an actual flow of that gas has been measured using following formula

$$Flow\ rate = \frac{\Delta L}{t} \times 60, \tag{2.2}$$

where ΔL is the change in volume displaced by the gas in time t. Flow rate, ΔL and time are measured in SCCM (Standard Cubic Centimeter per Minute), ml and seconds respectively. Figure 2.27 shows the calibration plots of all the three gases required for the RPC performance studies. It is clear from this figure that the measured flow of each gas is linear with the set flow of that gas provided by GMU and indicates proper functioning of gas mixing unit.

2.5 Detector Characterization & Test Set-up

To characterize the performance of the RPCs made from the selected electrodes and under different gas compositions mentioned below, we performed the efficiency, noise rate and

leakage current measurements. A muon telescope consisting of three scintillator detectors being connected with the NIM/VME Data Acquisition system (DAQ) has been used for conducting these measurements. A complete measurement setup at Delhi University lab is shown in Figure 2.28.

Figure 2.28: A complete lab setup for RPC characterization studies at Delhi University lab.

All fabricated RPCs (Bakelite and glass) are characterized for various gas compositions, temperatures and humidity to obtain the optimum parameters to maximize the detector performance. We use following gas compositions for RPCs performance. All the Glass RPCs are tested in avalanche mode with four different gas mixture compositions as follows:

1. First Composition: 95% Freon (R134a), 5.0% Isobutane (C_4H_{10}) and 0.0% SF_6
2. Second Composition: 90% Freon, 10.0% Isobutane and 0.0% SF_6
3. Third Composition: 95% Freon, 4.5% Isobutane and 0.5% SF_6
4. Fourth Composition: 90% Freon, 9.0% Isobutane and 1.0% SF_6

The Bakelite RPCs are tested under the following gas compositions:

1. First Composition: 67.7 % Freon, 32% Isobutane and 0.3% SF_6
2. Second Composition: 95 % Freon, 4.5% Isobutane and 0.5% SF_6

The flow rate is kept fixed at 10 SCCM for all the compositions. Since the Freon gas is the primary ionizing gas, we use it in a large percentage. The C_4H_{10} is a flammable gas so it would not be advisable to increase its composition to large fraction due to safety reasons.

The SF_6 gas is used to control the excess number of electrons, therefore, its fraction in the gas mixture has been kept low and varied from 0 to 1%. For all the above compositions, we measured the efficiency, noise rate and leakage current of the RPCs made from all the three types of the glasses and two types of Bakelites.

2.5.1 Efficiency Measurements

All the fabricated RPCs are tested for their efficiencies at various operating voltages with different gas compositions and under different environmental conditions. The detector to be characterized is interleaved in between the scintillator detectors and readout of the DAQ system as shown in Figure 2.29 and its corresponding logic circuit diagram is shown in Figure 2.30. Analog pulses from the scintillators are converted to digital pulses using discrim-

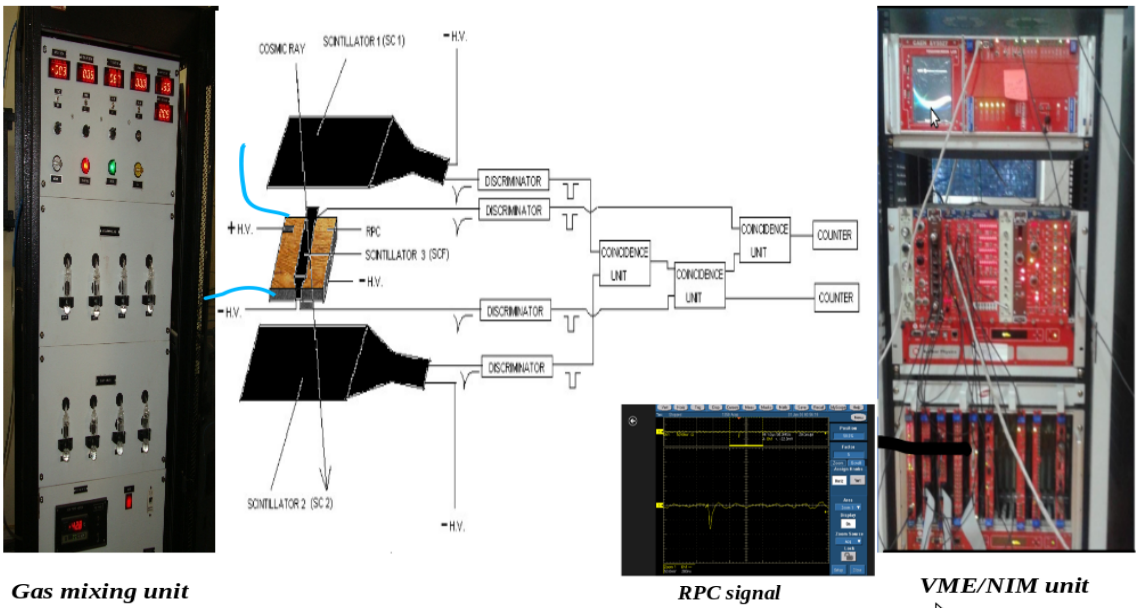

Figure 2.29: Data Acquisition set-up for RPC characterization.

inator module. Discriminator produces a standard logic signal when the pulse height of the signal is greater than a certain threshold value, and blocked the low amplitude noise from the photo multiplier tube. We set the threshold value 50 mV for discriminator operation. The discriminated scintillator pulses are then ANDed together to get a 3 fold coincidence (3F) using NIM based logic unit and thus generate our trigger signal. The counting rate of generated signals at every step is monitored using a VME based scalar module. Pickup strips of RPC are connected to pre-amplifiers by twisted pair cables and to discriminators

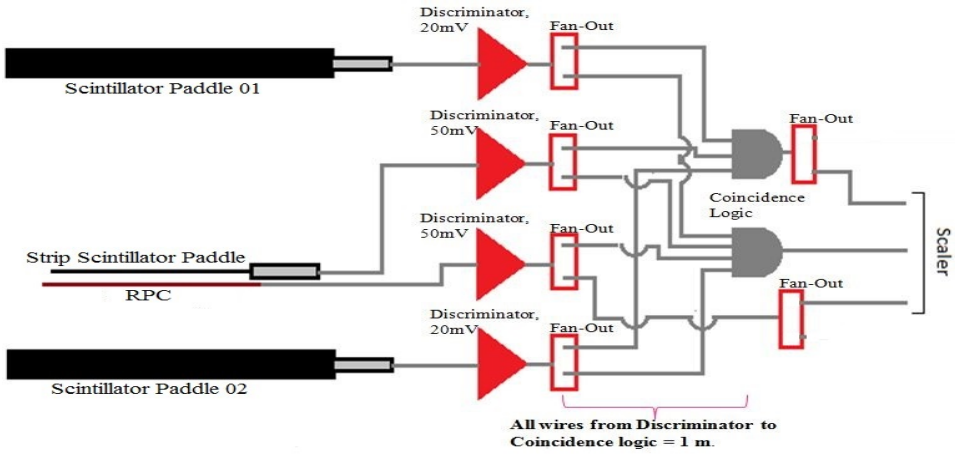

Figure 2.30: Coincidence logic circuit for RPC characterization.

by coaxial cables. The Efficiency of the RPC is determined by the ratio of RPC signal in coincidence with the trigger signal as

$$Trigger\ signal = Scintillator\ 1\ \ \textbf{AND}\ \ Scintillator\ 2\ \ \textbf{AND}\ \ Scintillator\ 3$$

$$Efficiency = \frac{RPC\ signal\ in\ coincidence\ with\ 3F\ Trigger\ signal}{Trigger\ signal}$$

Figure 2.31 shows efficiency of all the glass RPCs, for the first and second gas composition and Figure 2.32 show the same with third and fourth gas composition respectively. From these figures it can be seen that the efficiencies under different gas compositions are similar for all the types of the glasses and is above 95%. All the measurements reported here are performed at the normal pressure, relative humidity varying between 40% to 45% and temperature varying between $19°C$ to $21°C$. From the bulk resistivity, surface resistivity and surface uniformity studies for both the Bakelite electrodes, we found Formica having the best surface texture. Therefore, we have performed efficiency measurements for the Formica based RPC detector. Figure 2.33 shows the efficiency results for two gas compositions for Bakelite. It is clear from Figure 2.33 that Formica RPC reached upto 90% under first and second gas compositions.

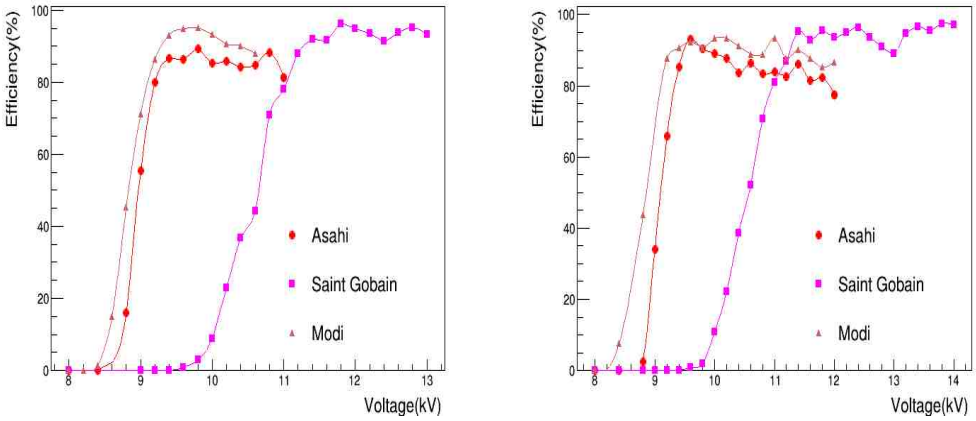

Figure 2.31: Efficiencies of Asahi, Modi and Saint Gobain glass samples using first and second gas compositions.

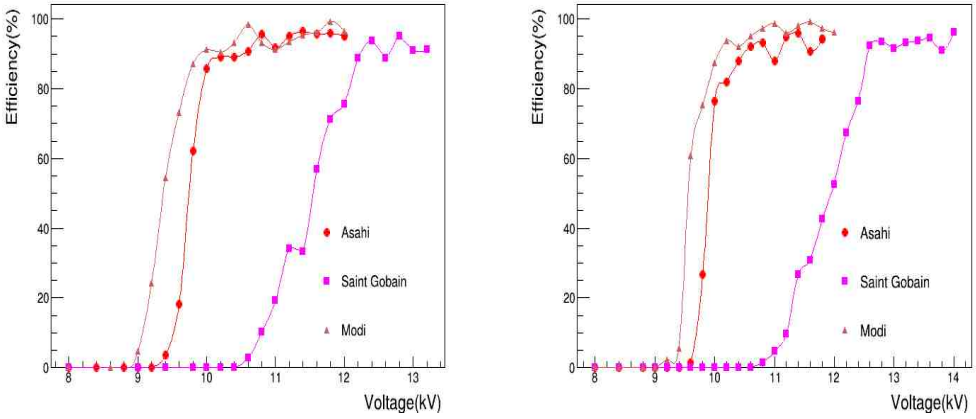

Figure 2.32: Efficiencies of Asahi, Modi and Saint Gobain glass samples using third and fourth gas compositions.

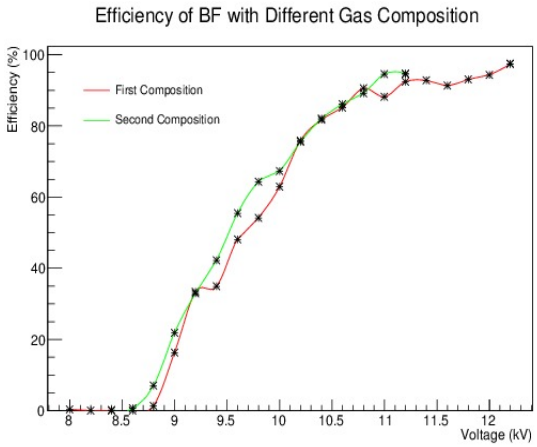

Figure 2.33: Efficiency of Formica Bakelite RPC with different gas compositions.

2.5.2 Noise rate and Leakage Current

Noise rate of an RPC is defined as a total counting rate of all its signals above a certain discriminator threshold. These noise signals can be produced by the surrounding radiations, cosmic ray charged particles of all energies as well as due to the dark current of the chamber. For a better RPC performance, it is necessary that the noise rate per unit cross-sectional area of a particular RPC should be consistent when averaged over a reasonable period of time. Noise rate directly effects the RPC efficiency and its gain; increase in noise rate decreases the detector efficiency. Therefore, each fabricated RPC is also tested for noise rate and leakage current for all glass samples. Figure 2.34 shows the noise rate for all glass samples under different gas compositions. Noise rate as expected is maximum in the absence of SF_6 and decreases as we increase the SF_6 fraction. The noise rate is maximum for Modi and minimum for Asahi. Figure 2.35 shows the leakage current under different gas compositions. Leakage current is much higher for Modi compared to Asahi and Saint Gobain which have reasonable values. These observations are consistent with the roughness measurement reported in Section 2.3.3, where we found Modi glass having the most rough surface while Asahi having the least rough surface with Saint Gobain in between the two.

2.5.3 Variation of Thresholds

The threshold setting for the discriminator plays a vital role in signal counting. A low discriminator threshold gives the high count due to the addition of electrical noise while the

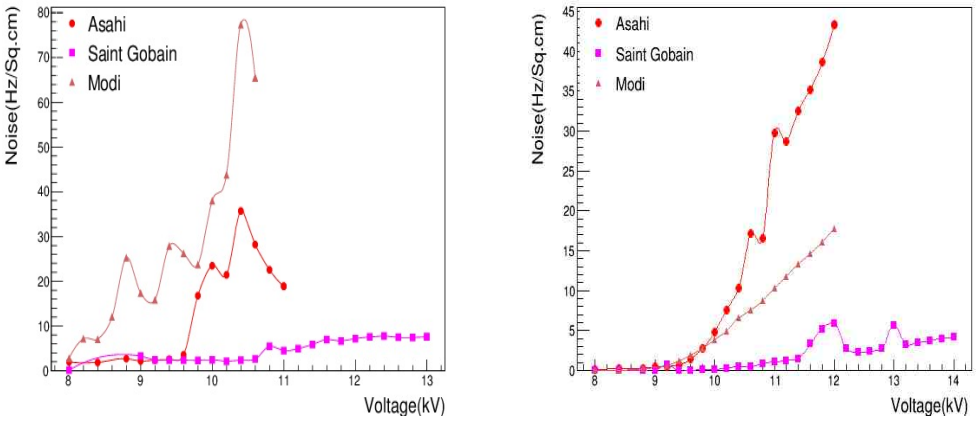

Figure 2.34: Noise Rate of glass samples using first and fourth gas compositions.

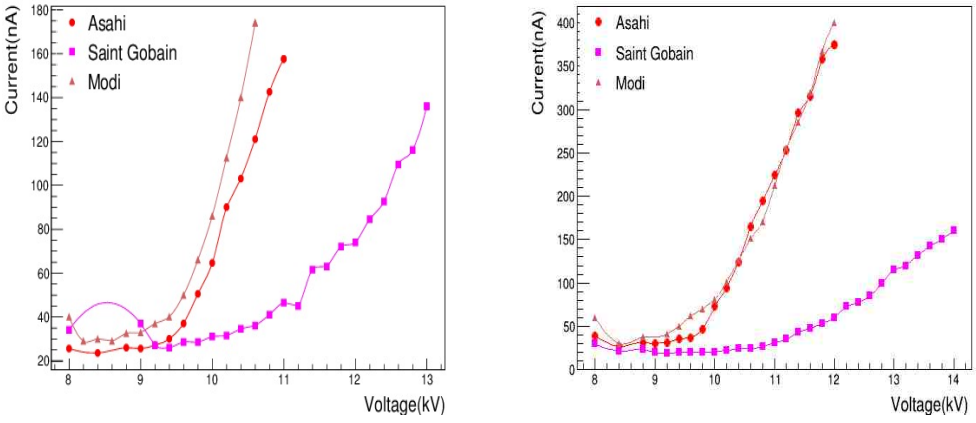

Figure 2.35: Leakage current of all glass samples using first and fourth gas compositions.

high threshold could reject the actual signal from the detector. Therefore, for a fine tuning of threshold value and to see the effect of threshold variation on the detector performance, we varied the threshold values for RPC detector. We observed the efficiency and noise rate under different threshold values like 30 mV, 50 mV and 70 mV. Figure 2.36 shows efficiency and noise rates for Asahi glass RPC with threshold variation. We observed that there is a less effect of threshold variation over the efficiency of RPC, whereas, the noise rate decreases as we increase the threshold value within range of 30 mV-50 mV. On further increasing the threshold value up to 70 mV count rate for RPC remains same. On the basis of this study, we fixed the threshold value of 50 mV for further studies.

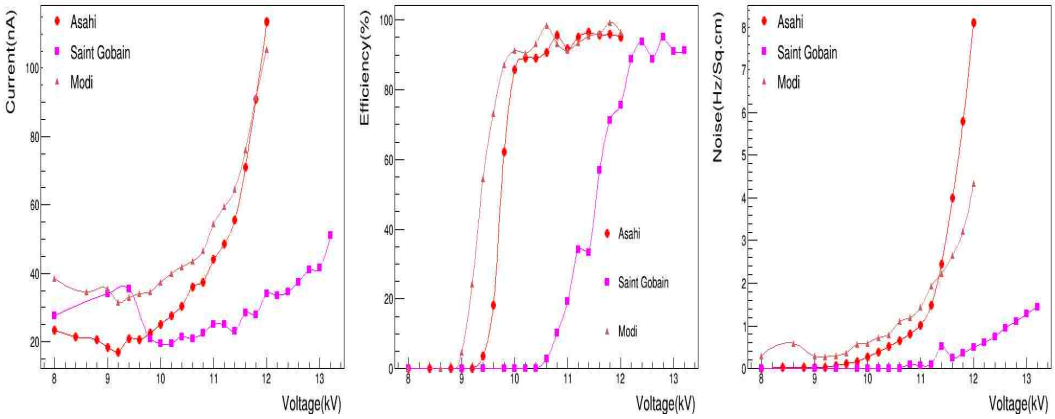

Figure 2.36: Leakage current, efficiency and Noise rate for Asahi Glass at three different threshold values and with third gas composition.

2.5.4 Variation of Environmental Temperature and Humidity

In order to optimize the RPC performance, its working under different environmental conditions like temperature and humidity is very important. We varied the temperature and humidity to different values and measured the efficiency, noise rate and leakage current for the RPCs made up from all types of electrodes (Bakelite and Glass). Figure 2.37 shows the effect of temperature and humidity variation on the efficiency, current and noise rate for the RPC made up of Asahi glass. We observed that the leakage current and noise rate of RPCs increases with increase in room temperature and relative humidity. However, for the temperature from 18 to 21 degree centigrade and relative humidity varying between approximately 35 and 45%, there is not much effect on leakage current and noise rate.

But, further increasing the temperature to $24°C$, both the leakage current and noise rate increases. On the other hand, efficiency of RPCs remains almost unaffected under the given temperature and relative humidity variation. the results present here are only for the Asahi glass, however, other two glasses also show the similar characteristics. Further, we have

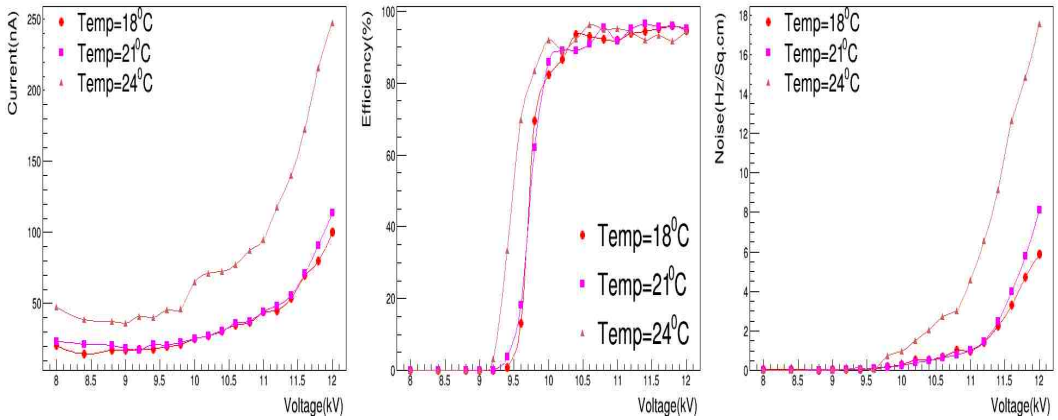

Figure 2.37: Leakage current, efficiency and noise rate for Asahi Glass at three different temperatures. The relative humidity is maintained between 35% to 45%. These measurements are with third gas compositions.

also studied the performance of Formica Bakelite RPC (mainly noise, leakage current and efficiencies) using the gas composition (94 % Freon, 4.5% Isobutane and 0.5% SF_6) under different room temperatures and humidity combinations which are given below:
(a) $23°C$ room temperature and 35% room humidity
(b) $18°C$ room temperature and 40% room humidity
(c) $19°C$ room temperature and 60% room humidity
Formica RPC detector studies on operational environment basically humidity and temperature shows the increase in the leakage current as we have observed for glass electrodes. However, we see an abrupt fluctuation in leakage current at higher humidity as shown in Figure 2.38. On the other hand we found smoother curve for efficiency on lower humidity. The noise rate also increases with increase in temperature and humidity in case of Bakelite RPCs.

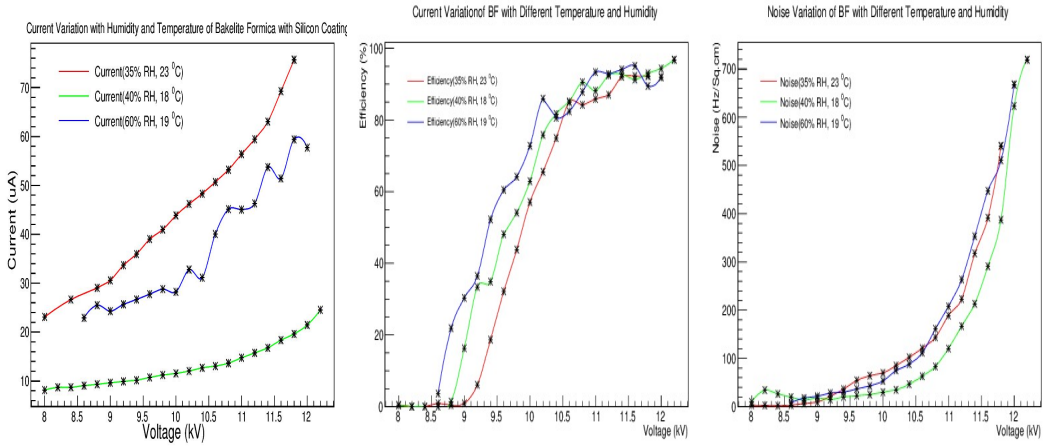

Figure 2.38: Leakage current, efficiency and noise rate for Formica Bakelite at three different temperatures and relative humidities. These measurements are with second gas compositions.

2.6 Results and Conclusions

The India-based Neutrino Observatory (INO) collaboration is planning to build a massive 50 kton magnetized Iron Calorimeter (ICAL) detector, to study atmospheric muon neutrinos and to measure the neutrino oscillation parameters. ICAL will have a unique quality to discriminate the charged muons (μ^- *or* μ^+) due to the applied magnetic field of strength 1.5 T. An approximately 28,000 Glass Resistive Plate Chambers (RPCs) of dimension 2 m $\times$ 2 m in size will be used as active elements for the detection of charged particles at ICAL detector. High efficiency, good timing and spatial resolution, large detection area and low construction cost of RPCs make them suitable choice for ICAL detector. However, before we embark upon building such a large amount of RPCs and freezing various parameters, it is important to perform a thorough $R\&D$ on all aspects of the detector performance. In this direction, we studied different types of electrodes (glass and Bakelite) for the RPCs available from the local market; three types of glasses, *viz.* Asahi, Saint Gobain, Modi and two types of Bakelites *viz.* Formica $\&$ Hylam. We performed various studies to assess the electrical properties of these electrodes. From our studies, we conclude that out of all glass samples qualitatively Asahi is better than Saint Gobain and Modi in terms of smoothness. Saint Gobain is best in terms of bulk Resistivity and reflectance. In case of Bakelite, Formica electrode have comparable bulk resistivity but more smooth surface texture compared to Hylam.

From performance studies of glass RPCs, we find that all glass samples give almost

similar efficiencies under all conditions and the value is always above 95$\%$. The threshold voltage for Saint Gobain is higher than others and the reason for this could be the higher bulk resistivity of the Saint Gobain glass. Saint Gobain shows lowest noise for all the gas compositions. Leakage current is lowest for Saint Gobain for the first three gas compositions while Asahi shows the lowest current for the fourth gas composition. However, at lower bias voltages large fluctuation in the current is observed. The error on the current measurement is $2\% \pm 9\ nA$, so the current measurements are consistent with each other within errors at lower bias voltages. From our gas mixture composition studies, we find that the efficiency is not much dependent on the gas composition. The fourth composition of $R134a$ (95.0%), C_4H_{10} (4.0%), SF_6 (1.0%) is found to be giving the lowest noise rate and least current as expected.

The study on variation of temperature and humidity shows that with increase in temperature from 18 to 21 degree centigrade and relative humidity varying between approximately 35% and 45%, there is not much effect on leakage current and noise rate. But, further increasing the temperature to $24^{\circ}C$, both the leakage current and noise rate increases. We did not find any considerable effect of temperature and relative humidity on efficiency.
Formica Bakelite RPCs performance studies shows the similar efficiency (90%) for both the gas composition but with higher noise rate and leakage current compare to glass electrodes under different temperatures and relative humidity. Hence, we conclude that the two Bakelite electrodes that we studied are not well suited for INO-RPC. Nevertheless, there is a need to further perform the Bakelite $R\&D$ with better electrodes. In conclusion, we found that Saint Gobain and Asahi glasses are best suited for the INO-ICAL RPCs in terms of most of the parameters that we studied. We suggest to operate the RPC under the $R134a$ (95.0%), C_4H_{10} (4.5%), SF_6 (0.5%) gas composition and keep the temperature around 20^0C and relative humidity under control. It is to be noted, however, that all the studies reported in this thesis are performed on small prototypes RPCs of size 30 cm $\times$ 30 cm. We are in the process of constructing actual size INO-ICAL RPCs to further continue our studies.

Chapter 3

ICAL Detector Response to Muons and Hadrons

To explicitly detect the oscillation pattern in the L/E spectrum of atmospheric muon neutrinos, the energy and direction of the incoming neutrino have to be known very accurately. As mentioned earlier, atmospheric neutrinos interact with iron target in ICAL detector and produced daughter particles i.e. muons and hadrons. The energies and directions of these interacting neutrinos can be determined from the reconstructed energies and directions of their daughter particles. Thus, the ICAL energy and direction resolution for these particles plays an important role in the physics reach of ICAL. Any uncertainty in the estimation of energy and direction of these particles will directly affect the accuracy of neutrino oscillation parameter measurements. This chapter includes the response of the ICAL to the muons and hadron produced in the atmospheric ν_μ interaction. In this chapter, we mainly discuss the detail of methods adopted and analysis performed to estimate the hadron energy resolution for INO-ICAL detector.

3.1 Atmospheric Neutrino Interaction at ICAL

The neutrinos are not directly observed, but we observe the charged particles produced due to the interaction of neutrinos. The atmospheric muon neutrinos (ν_μ) and anti-neutrinos ($\bar{\nu}_\mu$) interact with iron target in the ICAL detector. When these atmospheric neutrinos interact with the detector, they undergo Charged-Current (CC) and Neutral Current (NC) interactions. In CC interactions neutrino changes its identity to a charged lepton via the

exchange of charged vector boson $W^{\pm}$ while in Neutral Current interactions neutrino or anti-neutrino exchange a neutral vector boson Z^0.

As shown in Figure 3.1, at low energies neutrino interactions are predominantly quasi-elastic (QE) and resonance or single pion production while at high energies deep inelastic scattering (DIS) takes place. Quasi-elastic scattering is the most important reaction for neutrinos energies up to 1 GeV, in which neutrino scatter off an entire nucleon rather than the constituent parton. In resonance, single pion is produced along with one lepton on neutrino interaction. In DIS, the neutrino scattering takes place off of the parton inside the nucleons. All possible neutrino interaction processes are shown in Figure 3.2. In this figure, ν stand for every kind of neutrino flavor as well as for its anti-particle. R stand for resonance and X represent the hadrons produced in the interaction process.

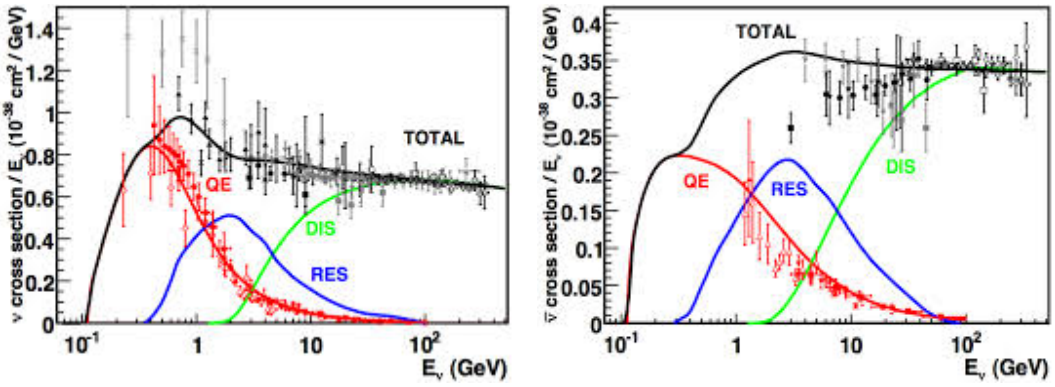

(a) Neutrino cross-section measurement (b) Anti-neutrino cross-section measurement

Figure 3.1: Charge-Current cross-section measurement as a function of neutrino energy (a) for muon neutrinos (b) for anti-neutrinos [98].

Muon neutrinos and anti-neutrinos are identified through their CC interactions as:

$$\nu_\mu(\bar{\nu}_\mu) + X \rightarrow \mu^-(\mu^+) + X'. \tag{3.1}$$

Muon typically deposits its energy in the detector in a track-like pattern while the hadronic recoil system, X′ produce a shower-like deposition pattern. Hadrons produce shower of hits near the event vertex. Since, hadrons do not give a track like muon, energy reconstruction of these particles can be done only on the basis of their shower hits.

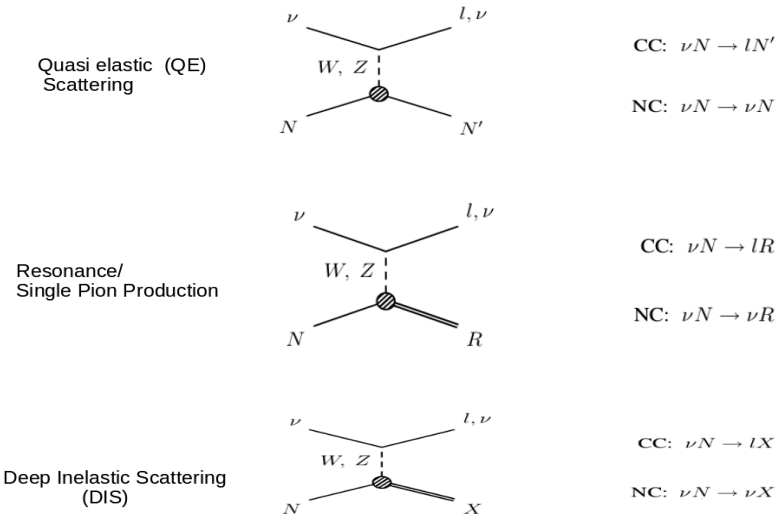

Figure 3.2: Atmospheric neutrinos interaction processes at ICAL.

3.2 ICAL Detector Simulation

In order to assess the capability of ICAL detector for the neutrino interaction products i.e. muons and hadrons, a complete simulation framework has been followed which incorporates the steps given below:

- **Event Generation:** First we generate the particles randomly which results from interactions of neutrino with matter using theoretical models. For this purpose NUANCE [99] neutrino generator has been used. This part gives information about the reaction channel, energy and momentum of the interaction products along with the information of interaction vertex.

- **Event Simulation and Digitization:** This step allows to simulate propagation of particle through the detector. Basically, this part shows how the particles pass through the detector and what is the effect of detector geometry and magnetic field on passage of particles inside the detector. For this purpose, GEANT4 [100] simulation package which simulate the propagation of each particle based on detector geometry, tracking and physics models has been used. This gives the information about the coordinates (x, y, z and t) of a particle at interaction vertex and energy deposition by the particle inside detector. Each information from the simulated output is then digitized with the addition of detector's electronics, efficiency and noise.

- **Event Reconstruction:** Finally, each particle produced in the interaction is then

reconstructed by their track using suitable fitting algorithm to get their energy and momentum information. This gives the information of reconstructed energy and momentum of the interaction particle.

For detector simulation, a code based on GEANT4 simulation package within CERN-ROOT [104] framework has been developed by the INO collaboration. All the above mentioned simulation steps are included in this code. This package incorporates the 150 iron-RPC layered ICAL detector with all essential detector parameters like filled gas mixture, air gap, thickness, placement and alignment of each of detector component, and magnetic field map. An example of visualization of simulated muon neutrino interaction at ICAL for a deep inelastic process is shown in Figure 3.3.

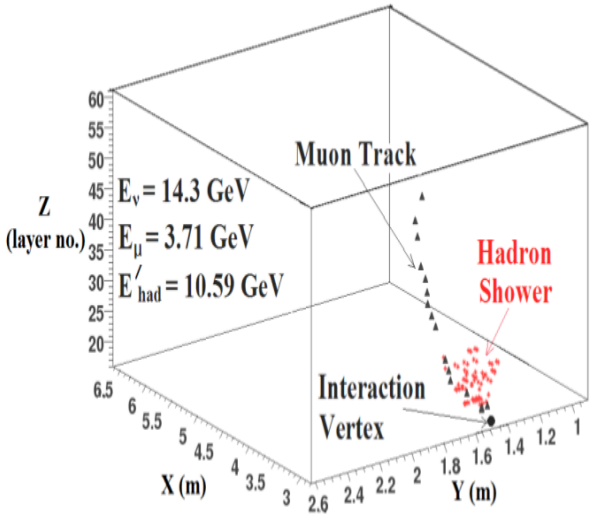

Figure 3.3: Visualization of deep inelastic neutrino charged-current interaction in the simulated ICAL detector. Red points show the hadron shower near the interaction vertex and a clear muon track can be seen in black points in vertical Z direction.

3.3 Detector Response for Muons

The ICAL detector is mainly sensitive to muon neutrinos or anti-neutrino which fall in the energy range 0.5-10 GeV. All the interaction processes as mentioned in Section 3.1 equally participate in this energy range. CC interaction of muon neutrinos and anti-neutrinos produce muons while single pion along with one lepton are produced due to resonance interactions. Hadrons are produced due to deep inelastic scattering (DIS) at high energies.

Muon neutrinos and anti-neutrinos can be easily separated by the direction of curvature of the charged muon track in the magnetic field of the detectors. The muon momentum is determined from the range for muons that stop in the detector and from curvature of exiting muons. the charge of the muon can also be found from the direction of curvature of the track and this in turn distinguishes ν_μ and $\bar{\nu}_\mu$ interactions. The muon track reconstruction is based on a Kalman filter algorithm [101] that takes into account the local magnetic field. The structure of each of these algorithms is briefly described in Ref. [102].

To find out the detector response for muons, Monte Carlo (MC) muon event analyses have been performed using INO simulation framework. Firstly, muons in the momentum range 1-20 GeV/c are allowed to fall in the central region of the detector where the magnetic field is uniform and then in the peripheral and side region of the detector where the magnetic field is non-uniform. In each case, muon momentum resolution and zenith angle resolution, momentum reconstruction efficiency and relative charge identification efficiencies have been obtained. The method and analysis techniques adopted for these studies are largely discussed in Refs. [102, 103].

Figure 3.4 and 3.5 which have been obtained from Ref [102], show the obtained muon momentum resolution and zenith angle resolution respectively in the central region of the detector. In order to find the dependence of resolution on azimuthal angle, resolution studies has been performed in different azimuthal (ϕ) bins; the azimuthal symmetry can be affected due to the presence of the magnetic field as well as the coil gaps and support structures. It is clear from these figures that in the uniform magnetic field ICAL is able to achieve 9-14$\%$ muon momentum resolution. A very good angular resolution about a degree for all angles for momenta greater than about 4 GeV/c has been observed, which is most important for studying the neutrino mass hierarchy through matter effects. Figure 3.6(a) shows the reconstruction efficiency of the muon which is about 80% and Figure 3.6(b) shows the relative charge identification efficiency which has been measured to be about 98$\%$ over this range.

3.4 Detector Response for Hadrons

In order to find the hadron energy response of the ICAL detector, MC simulations for hadrons produced in CC interactions have been performed. In a neutrino-nucleon interaction $\nu_\mu N \rightarrow \mu X$, where X represent the hadron shower in the final state, the energy of

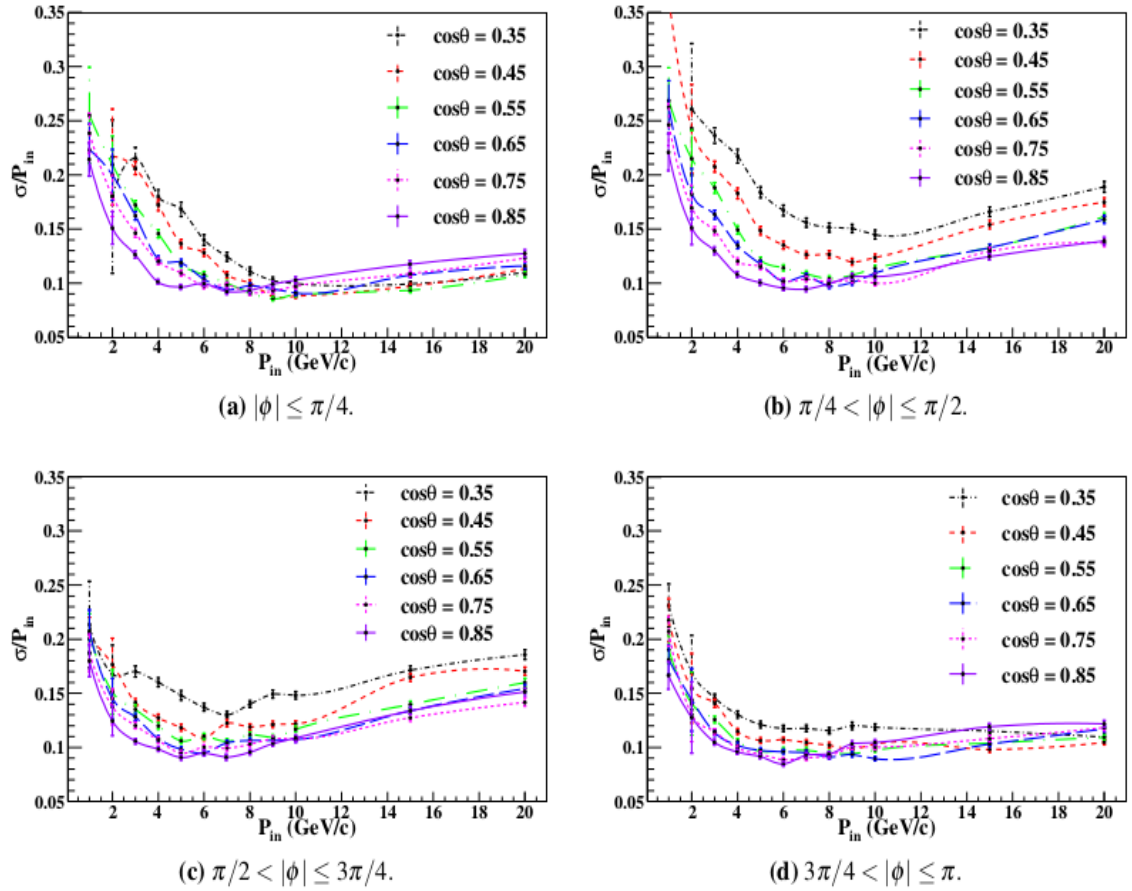

(a) $|\phi| \leq \pi/4$. (b) $\pi/4 < |\phi| \leq \pi/2$.

(c) $\pi/2 < |\phi| \leq 3\pi/4$. (d) $3\pi/4 < |\phi| \leq \pi$.

Figure 3.4: Muon momentum resolution as a function of input momentum and $\cos\theta$ with azimuthal angle (ϕ) dependence [102].

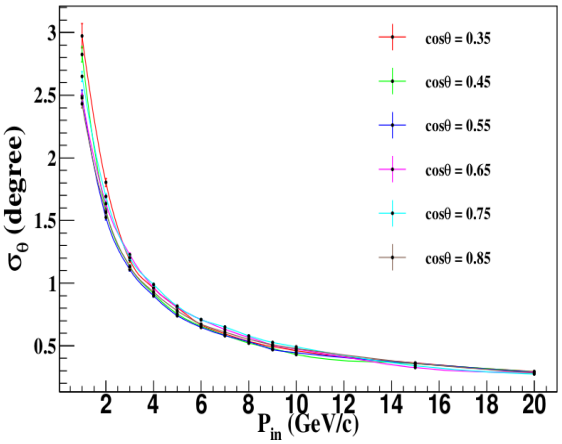

Figure 3.5: Muon angular resolution as a function of input momentum for different $\cos\theta$ values [102].

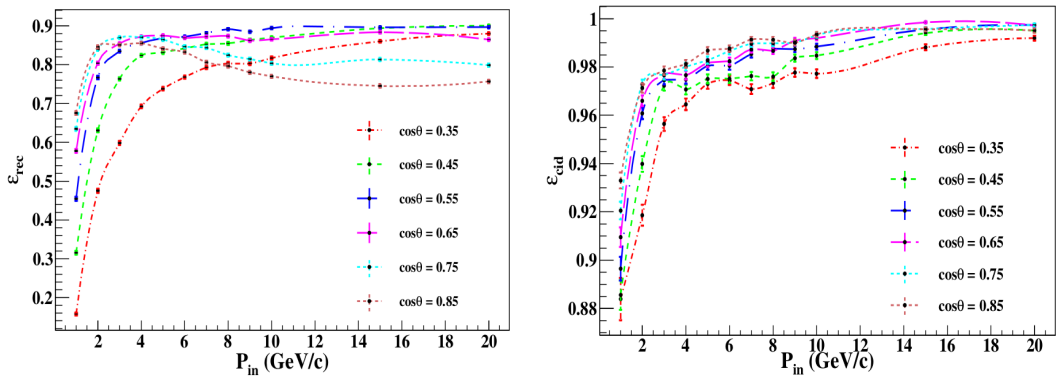

(a) Reconstruction efficiency (b) Charge-identification efficiency

Figure 3.6: Muon reconstruction and charge-identification efficiencies as a function of input momentum [102].

incident ν_μ can be estimated as

$$E_\nu = E_\mu + E_{hadrons} - E_N, \tag{3.2}$$

where E_N is the binding energy of the initial nucleon which is considered at rest, E_μ and $E_{hadrons}$ are the energy of muons and hadron produced in the interaction respectively. Eq. 3.2 clearly shows that the energy of incoming ν_μ (i.e. E_ν) directly depends on the energy of hadrons ($E_{hadrons}$). Therefore, for a fair measurement of incoming neutrino energy, hadron energy should be measured very carefully. The shower of hadrons consists of a mixture of hits generated by charged and neutral pions, which are found in major fraction of about 85 $\%$ on an average and remaining 15$\%$ of shower contributed by the hits from kaons and nucleons, including the recoil nucleons which are indistinguishable from the final visible hadronic shower. The neutral pions decay electromagnetically into two photons, while the charged pions propagate and develop into a cascade due to strong interactions. The shower energy fluctuation, leakage of energy and invisible energy loss mechanisms, etc. are the factors on which visible hadron energy depends and they can affect the energy resolution of hadrons.

The hadron energy resolution has been estimated both for the fixed energy hadrons, generated through MC generator, and for the hadrons generated in a muon neutrino interaction through the NUANCE event generator [99]. The fixed energy hadron analysis has been performed to find the suitable probability density function (PDF) for hadron hit distributions, and to see the detector response with fixed directions and fixed interaction vertex

as well as with smeared directions and smeared interaction vertices. The NUANCE generated hadron analysis has been performed using the appropriate PDF to obtain the realistic resolution for ICAL detector.

3.5 Energy Resolution with Fixed Energy Hadrons

In this section, we describe the characteristics of hadron hit (mainly pions) distributions at various energies and then on the basis of their pattern we investigate the suitable probability distribution function for the hit distribution. Using the appropriate fitting function, we present the hadron energy resolution for fixed energy, direction and vertex and then with smeared directions and vertices.

3.5.1 Analysis of Hadron Hit Pattern

To analyze the hadron hit pattern, different hadrons (pions, kaons and protons) of various fixed energies in the range 1-15 GeV are generated through MC generator. For simulation purpose, a total of 10,000 hadron events of various fixed energies in the above mentioned energy range are generated through MC single particle gun. Each event is randomly propagated within the central region of detector i.e. 200 cm $\times$ 200 cm $\times$ 200 cm. Since the ICAL is a magnetized detector, magnetic field may affect the direction of charged hadron. Although this effect is negligible but still we randomize the hadron direction over the zenith angle $0 \leq \theta \leq \pi$ and azimuthal angle over $0 \leq \phi \leq 2\pi$.

The ICAL RPC detectors provide two dimensional readout through the 1.96 cm wide copper strips placed above and below the glass electrodes. When a charged particle pass through the RPC detector, the two dimensional hit information recorded through these copper strips which provide the information of x and y coordinate of the hit. The RPC layer number provides the z coordinate. The x, y and z dimensions are defined by considering the center of the detector as origin. Generally, muon leaves one or two hits per layer so the position coordinates of muon can easily be obtained from the combination of X and Y strip hits. On the other hand hadron shower creates multiple hits per layer and this may give the ghost hits or the junk hits after combining the X and Y strip hits. In the framework of INO simulation code, these X strip and Y strip hits are encoded as variable X-hits and Y-hits. To eliminate these ghost hits, the maximum of either X-hits or Y-hits obtained per layer has been retained in get another variable named "orighits". Figure 3.7 shows the comparison of

X-hits, Y-hits and orighits distributions obtained from the propagation of π^+ and π^- events with an energy of 3 GeV. The orighits variable is finally used in the analysis to obtain the required hadron hit distributions.

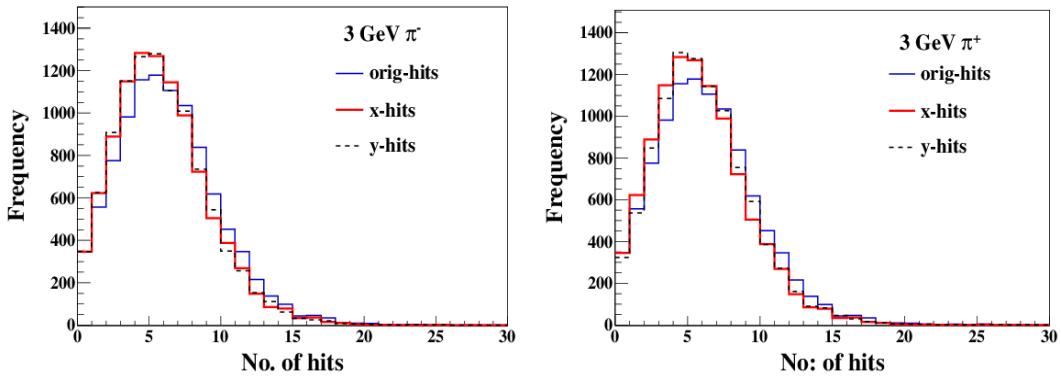

(a) π^- events (b) π^+ events

Figure 3.7: A comparison of X-hits, Y-hits and orighits distributions for π^- events and π^+ events of energy 3 GeV.

To study the characteristic of individual hadron at simulated ICAL detector, we obtained the orighits distributions from the propagation of charged pions, protons and kaons with randomized vertices at various fixed energies. The observed distributions are shown in Figure 3.8. The hit distributions are almost similar for all the hadrons except for π^0, which shows somewhat narrow distribution compared to other hadrons. This reflect the electromagnetic character of π^0 which decay electromagnetically into two photons soon after its production. There are minor differences in the position of the peak and in the number of hits for the same incident energy for various particle which may be caused due to incident angular smearing and mainly due to strong interaction of hadrons with the detector. It can be deduced that ICAL detector is not capable of distinguishing between individual hadrons, therefore, MC charged pions ($\pi^{\pm}$) which are having the major contribution in hadron shower are then analyzed finally to see the detector response to the hadrons.

A sample of hit distributions obtained from the propagation of charged pions of low energy (3 GeV) and of high energy (8 GeV) through the ICAL detector are shown in Figure 3.9. We observed that the hit patterns are asymmetric and have a long tail towards the x-axis side. It has also been observed that the low energy pion produce several zero hits or no hits in the detector while for the case of high energy pion, there are no zero hit counts. It can be seen from Figure 3.9 that for pion energy $\geq$ 5 GeV, the hit distributions

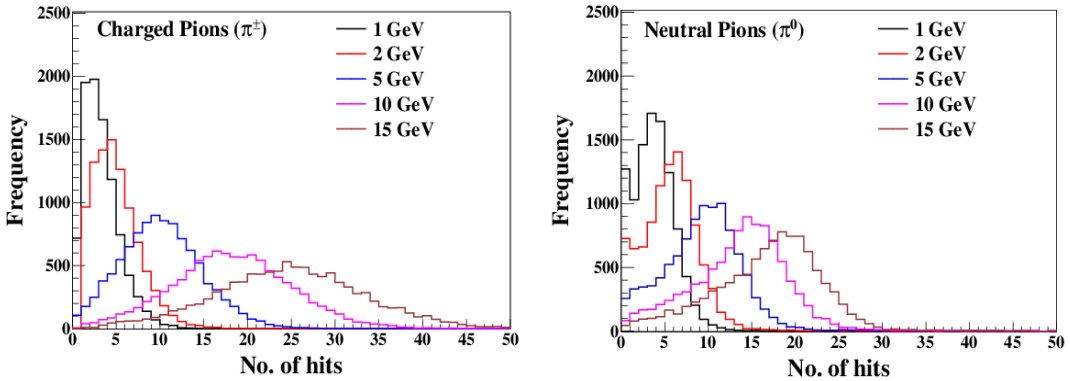

(a) Charged pions

(b) Neutral pions

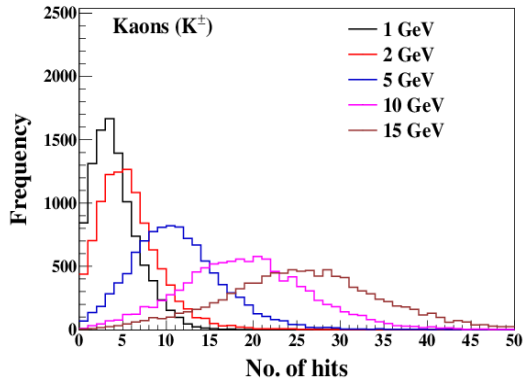

(c) Kaon

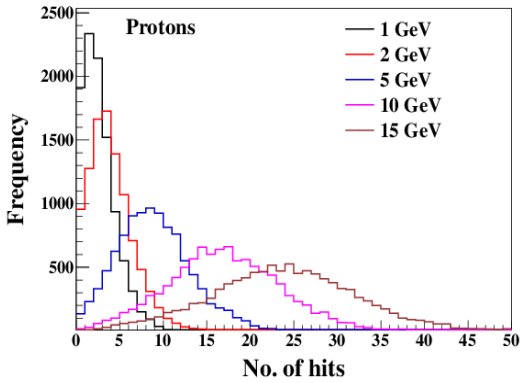

(d) Proton

Figure 3.8: Hit distributions obtained for various hadrons of different energies in the simulated ICAL detector.

are symmetric and have no zero hit counts.

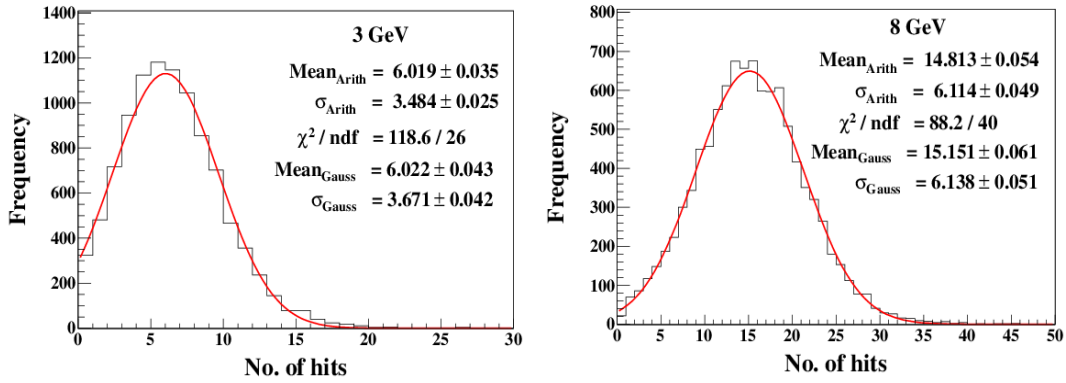

(a) Pions at 3 GeV energy

(b) Pions at 8 GeV energy

Figure 3.9: A sample of hit distributions of pions of fixed energy at 3 GeV and 8 GeV, fitted with Gaussian distribution function.

3.5.2 Choice of Probability Density Function

As described in Section 3.5.1, The pion hit distributions are not symmetric about mean in case of energies < 5 GeV but becomes symmetric for higher energies. Since the probability distributions can be viewed as a tool for dealing with uncertainty obtained in data, it is important to know distribution function which describe our data best. As most of atmospheric neutrino events in ICAL fall in the low energy region, it is very crucial to find a suitable PDF that provides the best shape of the hit distribution especially in this region as well as in higher energy regions. Since these PDF's will ultimately be used to carry out the ICAL physics potential studies, the accurate knowledge of hit distribution is essential.

The energy loss of a particle passing through the materials are commonly modeled using Gaussian (Normal) or Landau distribution functions. In order to obtain a suitable fit function for the hadron hit distribution, we performed a fit to the data with three different fit functions *viz* Gaussian, Landau convoluted Gaussian and Vavilov distribution [105] functions. First, we tried to fit the data using Gaussian distribution function. A sample of Gaussian fit for pion hits of energy 3 GeV and 8 GeV are shown in Figure 3.9. It can be seen from the figure that the parameter χ^2/ndf, which determine the goodness of fit, is $\approx$ 4.6 at lower energy (3 GeV) while at high energy (8 GeV) its value improves to 2.2. This indicates that in the lower energy region Gaussian distribution is not describing the data well while at higher energies distribution is approximated by Gaussian. Thus, Gaussian

distribution function is not adequate to describe the data. Then we tried to fit the data using Landau convoluted Gaussian function to take care of the long tail. A sample of Landau convoluted Gaussian fit to same data is shown in Figure 3.10(c) and in Figure 3.10(d). This fit function also does not appear to describe the data well and hence there is a need of better PDF to fit the data. We tried Vavilov distribution function to fit the data.

Vavilov distribution function [105] is generally used to calculate the energy loss of heavy charged particles in moderately thick absorbers [106]. The functional form the Vavilov distribution is given by

$$P(x;\kappa,\beta^2) = \frac{1}{2\pi i}\int_{c-i\infty}^{c+i\infty}\phi(s)e^{xs}ds, \tag{3.3}$$

where

$$\phi(s) = e^{C}e^{\psi(s)}, \quad C = \kappa(1+\beta^2\gamma)$$

and

$$\psi(s) = s\ln\kappa + (s+\beta^2\kappa)\cdot\left[\int_0^1 \frac{1-e^{-st/\kappa}}{t}\,dt \;-\; \gamma\right] - \kappa\, e^{-s/\kappa}$$

where $\gamma = 0.5772156649$ is the Euler's constant. κ is the significance parameter to describe the energy loss by the particle [107]. The parameters mean and variance (σ^2) of the Vavilov function are given by

$$\text{mean} = \gamma - 1 - \ln\kappa - \beta^2; \quad \sigma^2 = \frac{2-\beta^2}{2\kappa}.$$

It has been observed that the shape of the distribution mainly depends upon the value of parameter κ. For $\kappa \leq 0.05$, Vavilov function behaves like the landau distribution and with increase in the value of κ it approaches to Gaussian distribution function. For the fitting purpose, we have used the Root based Vavilov PDF with the mean shifted from zero. It is to be noted here that for fixed energy, direction and fixed vertex analysis, the original Vavilov PDF, that is, P(x; κ, β^2) has been modified to $P_4 * P(\frac{x-P_2}{P_3};\ P_0,\ P_1)$. These changes account for normalization (P_4) and the shift of the mean to a non- zero value. The parameter P_4 is the overall normalization corresponding to the total number of pions propagated. It was found that using the modified definition of Vavilov function, the parameters of the function are highly correlated so in order to avoid this we redefine the Vavilov function parameters

Table 3.1: Statistical comparison of different fitting functions for 3 GeV and 8 GeV pion hit distribution.

E_π	Parameters	Histogram	Gaussian	Landau convoluted Gaus.	Vavilov
3 GeV	χ^2/ndf		4.6	4.2	1.7
	P (KS test)		8.1×10^{-6}	7.6×10^{-6}	0.95
	P (χ^2 test)		4.3×10^{-7}	5.1×10^{-7}	0.15
	$Mean$	6.01	6.02±0.04	6.02±0.04	6.01±0.04
	σ	3.48	3.67±0.04	3.60±0.04	3.43±0.05
8 GeV	χ^2/ndf		2.20	2.01	1.60
	P (KS test)		2.6×10^{-4}	1.2×10^{-4}	0.92
	P (χ^2 test)		4.0×10^{-3}	6.0×10^{-3}	0.17
	$Mean$	14.81	15.15±0.06	15.06±0.06	14.78±0.06
	σ	6.11	6.13±0.05	6.12±0.05	6.12±0.06

as $\frac{P_4}{P_3} * P(\frac{\mathrm{x-P_2}}{\mathrm{P_3}};\ \mathrm{P_0},\ \mathrm{P_1})$. This gives the modified mean and variance as (σ^2) as,

$$\text{Mean} = (\gamma\ -\ 1\ -\ \ln \mathrm{P_0} - \mathrm{P_1})\,\mathrm{P_3} + \mathrm{P_2}; \quad \sigma^2 = (2 - \mathrm{P_1})\,\frac{\mathrm{P_3^2}}{2\mathrm{P_0}} \tag{3.4}$$

Figure 3.10(e) and 3.10(f) show the Vavilov fit of pion hit distributions at energy 3 GeV and 8 GeV respectively. From these fits, it is clear that Vavilov distribution function provides a good fit for low energy as well as for high energy hadron data. Table 3.1 shows a comparison of all the statistical parameters including P values obtained from Kolmogorov-Smirnov (KS) test and χ^2 test for the Gaussian, Landau convoluted Gaussian and Vavilov distribution functions at 3 GeV and 8 GeV pion distribution function. This comparison indicates that Vavilov function fits the distributions best, it is found to be best for our requirement and has been used for the final analysis.

3.5.3 Resolution with Fixed Direction and Vertex

ICAL detector is most sensitive for atmospheric neutrinos with energies 0.5-15 GeV, therefore, the study of pions hit distributions in this energy range is crucial resolutions measurements. In order to obtain the detector response to hadrons, we first simulate the fixed energy pions with different incident directions falling on the fixed vertex point. The events were generated with MC single particle gun. A total 10,000 pion events were generated for each incident direction. Vertex was kept fixed at 100 cm $\times$ 100 cm $\times$ 100 cm. The events were

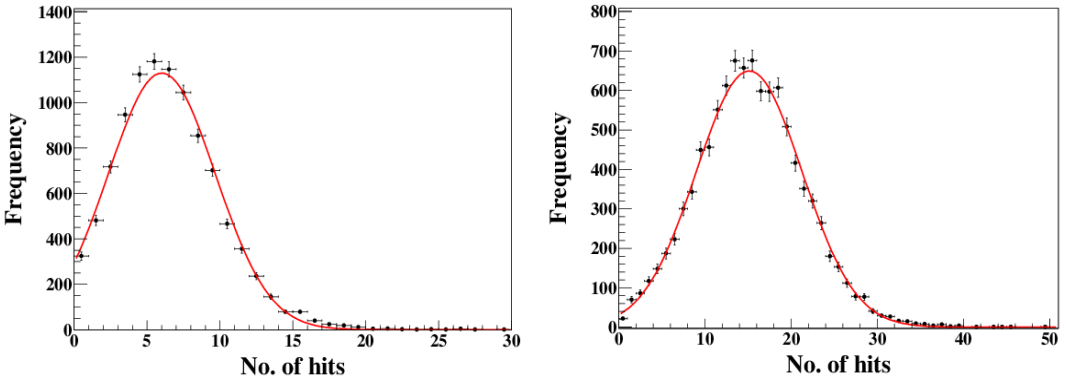

(a) Gaus fit at 3 GeV

(b) Gaus fit at 8 GeV

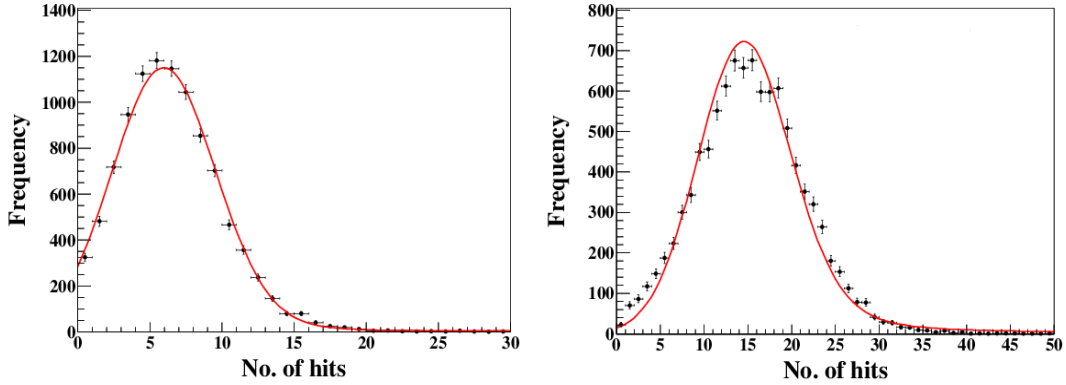

(c) Landau conv. Gaus fit at 3 GeV

(d) Landau conv. Gaus fit at 8 GeV

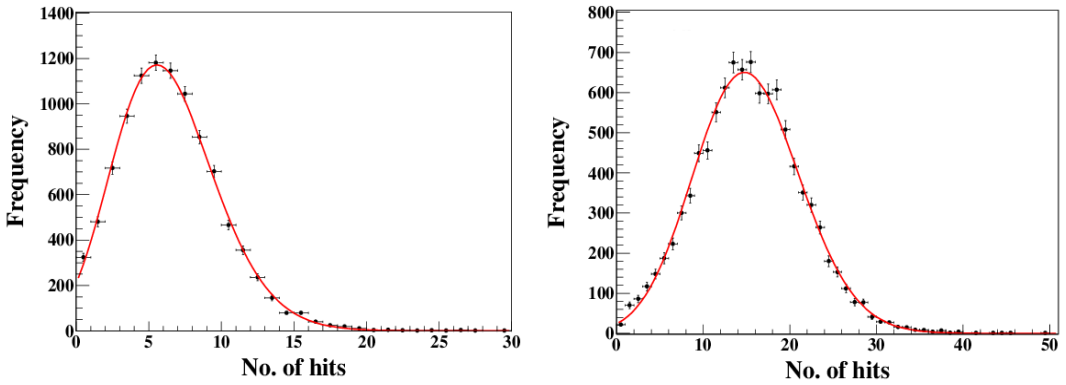

(e) Vavilov fit at 3 Gev

(f) Vavilov fit at 8 GeV

Figure 3.10: A comparison of pion hit distributions of 3 GeV and 8 GeV fitted with Gaussian, Landau convoluted Gaussian and Vavilov distribution function. All statistical parameters of these fits are mentioned in Table 3.1.

generated for the zenith angles $\theta = 5^{\circ}$, 30°, 45° and 60° within the energy range of 0.6-15 GeV. Azimuthal direction ϕ was allowed to smear over 0-2π for full azimuthal directional coverage. The generated events were made to pass through ICAL GEANT4 simulation and reconstruction code.

For each energy and angle bin we get a reconstructed hit distribution. As Vavilov distribution function fits well to the hit distribution at energies below 5 GeV and behave as Gaussian at higher energies (5-15 GeV), each hit distribution was fitted with this function for further analysis. Since the fit parameters of Vavilov distribution function are highly sensitive and correlated, we cannot fully depend on the errors of these parameters returned by ROOT and consequently on the errors of extracted mean and sigma of the hit distributions. To get rid of this situation, each hit distribution having 10,000 events was sampled into number of histograms such that each histogram contains at least 1000 events. Mean and sigma were then extracted from the fit to these histograms and corresponding errors were calculated using statistical deviation method.

The mean hits ($N(E)$) of the distributions increases with increase in the incident pion energy and saturates at higher energies. Average number of pion hits for all given directions from the fitted hit distributions have been plotted as a function of incident pion energy and is shown in Figure 3.11. This distribution then follow the equation:

$$N(E) = N_0[1 - exp(-E/E_0)], \tag{3.5}$$

where N_0 and E_0 are the fit parameters. It is clear from Figure 3.11 that the hadron energy is proportional to the number of mean hits in an event and follows a linear behavior in the desired energy range. Hence,

$$\frac{N(E)}{N_0} = \frac{E}{E_0}, \tag{3.6}$$

Table 3.2: Comparison of fit parameters obtained from the fit of mean Vs energy distribution with Eq. 3.5 for different incident directions.

Angle	N_0	E_0
$\theta = 5^0$	54.09 ± 19.01	14.99 ± 7.26
$\theta = 30^0$	52.91 ± 17.05	13.53 ± 6.24
$\theta = 45^0$	45.64 ± 16.6	15.75 ± 7.82
$\theta = 60^0$	42.33 ± 17.01	16.77 ± 9.038

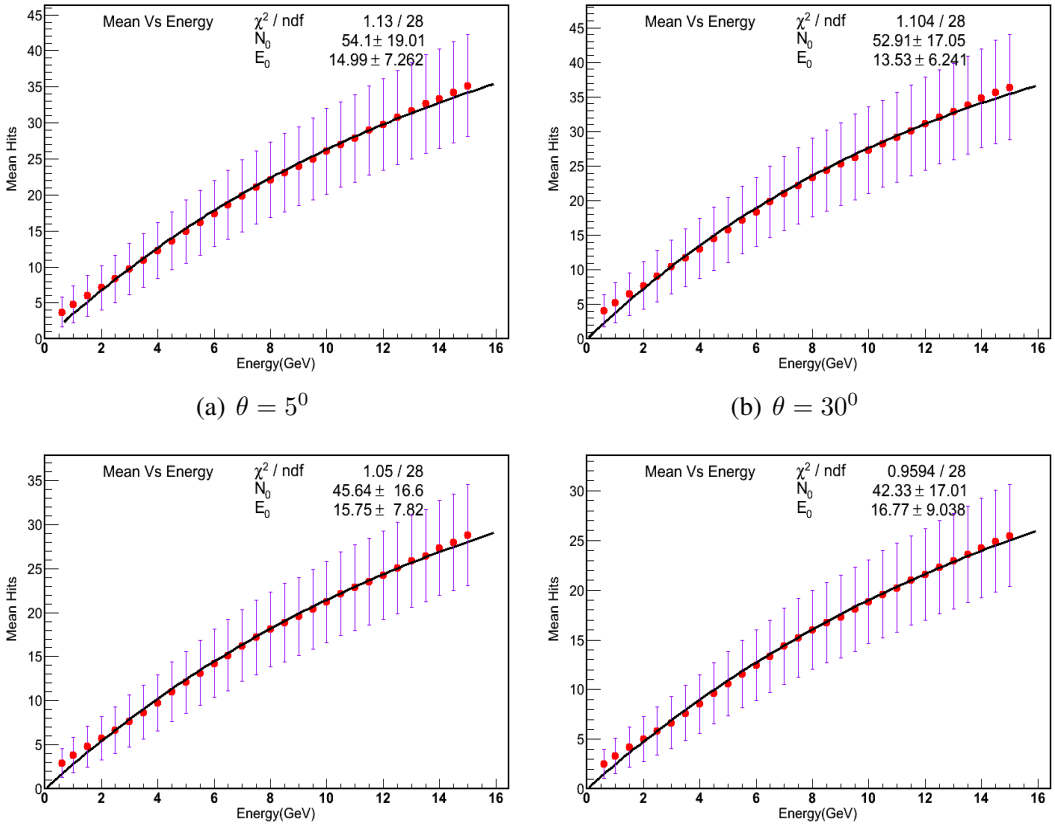

(a) $\theta = 5^0$ (b) $\theta = 30^0$

(c) $\theta = 60^0$ (d) $\theta = 45^0$

Figure 3.11: Average number of hits as a function of energy at different incident zenith directions fitted with the function $N(E) = N_0[1 - exp(-E/E_0)$.

The average number of hits show a linear dependence on energy at different angles. Comparison of fit results for different incident directions are mentioned in the Table 3.2. Here, The large errors in the fit parameters are due to high correlation between the parameters of Vavilov distribution function. Resolution of the detector based on this proportionality behavior can be defined as

$$\frac{\sigma}{E} = \frac{\Delta N}{N}, \tag{3.7}$$

where σ/E defined as the resolution, ΔN is the width of the pion hit distribution and E is the incident energy of the pion. In the rest of the chapter, σ/E will be used for energy resolution.

The standard form for the parameterization of hadron energy resolution is given by

$$\frac{\sigma}{E} = \sqrt{\left(\frac{a}{\sqrt{E}}\right)^2 + b^2} \tag{3.8}$$

where a is stochastic coefficient which takes systematic and statistical errors in to account and b is a constant. These parameters show the dependence on energy of the resolution and can be extracted from the fit.

The hadron energy resolution obtained from MC single pion with fixed energy, different directions and fixed vertex analysis using Vavilov fit are shown in Figure 3.12.

Figure 3.13 shows the resolution (σ/E) as a function of energy for $\theta = 5^0$, 30^0, 45^0, 60^0 together in a one picture; fitted with Eq. 3.8. Comparative study of hadron energy resolution of INO-ICAL detector using MC pion events is calculated in the energy range 0.6-15 GeV at different incident angles using different fitting functions has been done and fit results from Figure 3.13 are listed in Table 3.3.

Angle	a_1	b_1
$\theta = 5^0$	0.5288 ± 0.0060	0.151 ± 0.0024
$\theta = 30^0$	0.5492 ± 0.0057	0.1509 ± 0.0026
$\theta = 45^0$	0.5757 ± 0.0039	0.1275 ± 0.0020
$\theta = 60^0$	0.5842 ± 0.0064	0.1362 ± 0.0029

Table 3.3: Comparison of resolution fitting parameters at different angles.

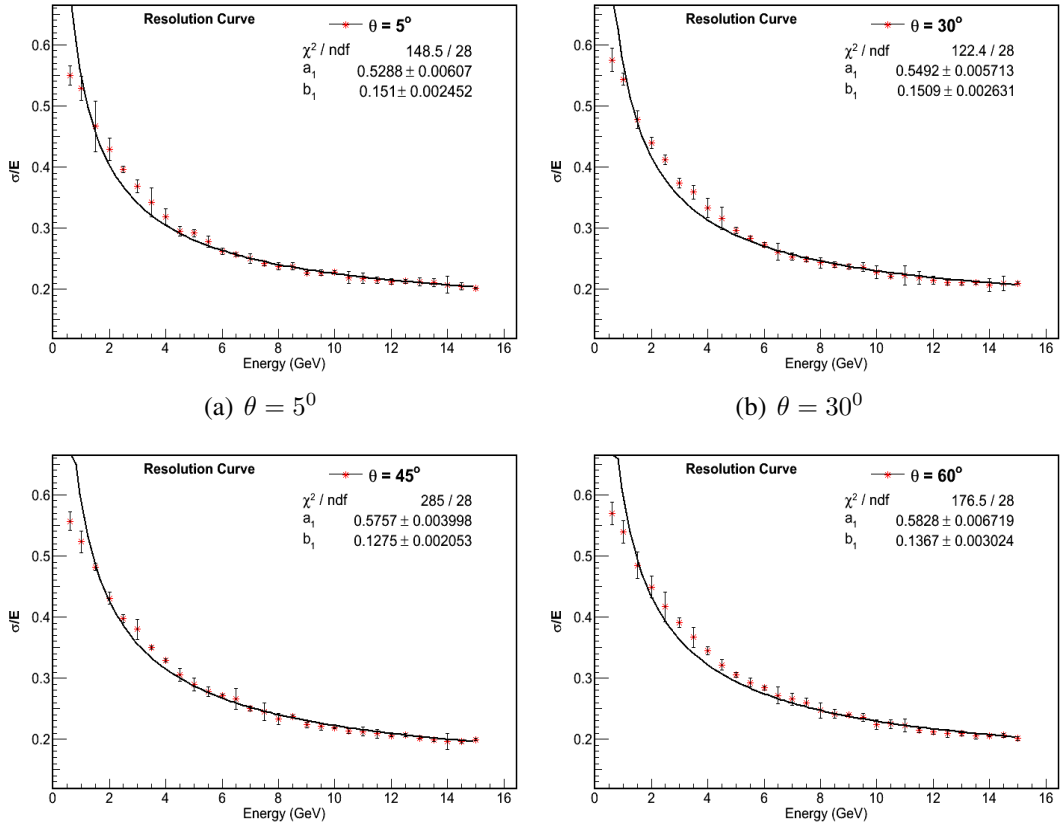

(a) $\theta = 5^0$ (b) $\theta = 30^0$

(c) $\theta = 45^0$ (d) $\theta = 60^0$

Figure 3.12: Resolution plots as function of incident pion energy fitted with Eq. 3.8 obtained for different fixed directions.

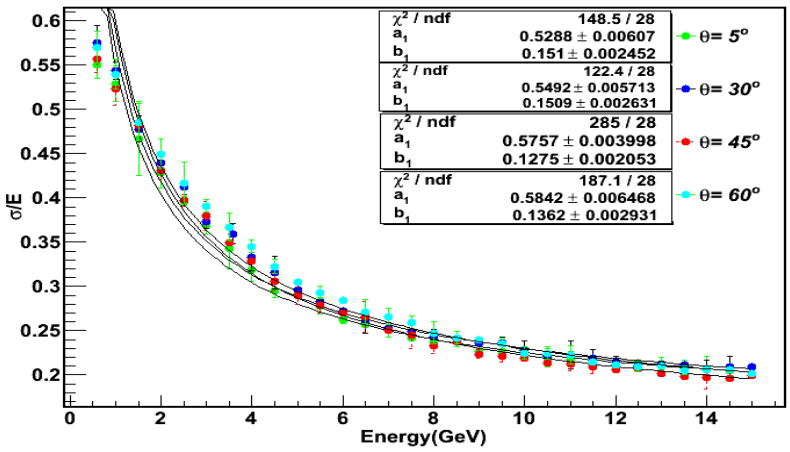

Figure 3.13: Hadron energy resolutions for different incident directions fitted with Eq. $\frac{\sigma}{E} = \sqrt{(\frac{a_1}{\sqrt{E}})^2 + b_1^2}$.

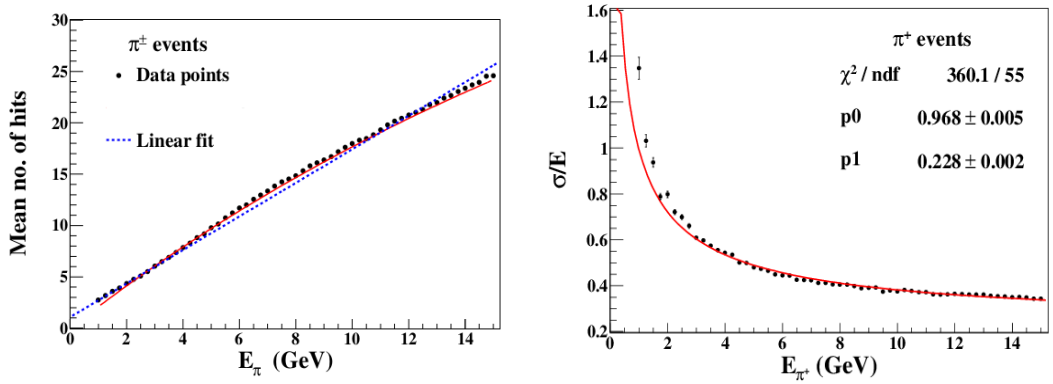

(a) Mean hits versus pion energy

(b) Resolution versus pion energy

Figure 3.14: (a) Average number of hits as a function of pion energy and fitted with Eq. 3.5, and (b) energy resolution as a function of pion energy fitted with Eq. 3.8 obtained from the propagation of π^+ events the at ICAL detector.

3.5.4 Resolution with Smeared Direction and Vertex

In actual ICAL detector, neutrinos will come from all possible directions and can interact with ICAL any where in the detector volume. Therefore, it is important that a simulation study is performed to mimic the actual scenario as closely as possible. To see these effects, we smeared the incoming direction and vertex of the pions. We propagate π^+ and π^- separately in the energy range (0.5-15 GeV) with an interval of 0.25 GeV. For this analysis, a total of 10,000 hadron events of various fixed energies in the above mentioned energy range are generated through MC single particle gun. Each event is randomly propagated within the central region of detector i.e. 200 cm $\times$ 200 cm $\times$ 200 cm. The hadron direction is smeared over the zenith angle $0 \leq \theta \leq \pi$ and azimuthal angle over $0 \leq \phi \leq 2\pi$.

Since π^+ and π^- hits show similar characteristics, we analyze π^+ data only for resolution. To obtain the energy resolution, all the hit distributions are fitted with Vavilov distribution function and analyzed similar to the fixed vertex MC analysis. Mean and sigma obtained from the Vavilov fitting are plotted as a function of incident hadron energy, fitted with Eq. 3.5 and are shown in Figure 3.14(a). It can be seen that the mean number of hits also follow a linear behavior with the pion energy as we have seen for fixed direction and vertex analysis earlier in Section 3.5.3.

Figure 3.15 shows the variation of Vavilov fit parameters with respect to pion energy. The hadron energy resolution obtained from MC single pion smeared vertex analysis using Vavilov fitted mean and variations as a function of pion energy are shown in Figure 3.14(b) and are fitted to Eq. 3.8. The fit parameters a and b extracted from the fitting are also listed on the plots. We find that the hadron energy resolution for ICAL detector using this analysis is about 80-35$\%$ for the energy range 1-15 GeV.

3.6 Energy Resolution with NUANCE Generated Events

In the previous section, we discussed the method of calibrating hadron energy and estimating the energy resolution with single pion events of fixed energies based on MC simulation. However, in reality when neutrino interacts with the detector it produces the muon and the shower of hadrons rather than producing a single hadron. Also, these hadrons can have any energy and can come from any direction. Therefore, to determine the realistic hadron energy resolution for INO-ICAL detector we have to analyze the multiple hadron events simultaneously, as produced in the neutrino interaction. We used the atmospheric neutrino

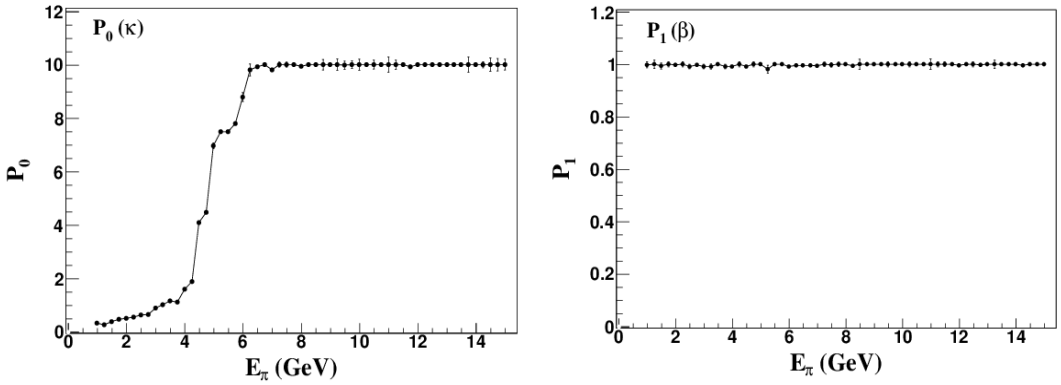

(a) paramter p0 (κ)

(b) paramter p1 (β^2)

(c) paramter p2

(d) parameter p3

Figure 3.15: Dependence of Vavilov parameters:(a) κ = p0, (b) β^2 =p1 (c) parameter p2 and (d) parameter p3 on incident pion energy.

interactions produced by NUANCE neutrino generator for performing this study. Only the hadrons produced in the CC atmospheric ν_μ interactions through quasi-elastic, resonance and deep inelastic scattering processes are analyzed for the energy resolution. Determining the energy resolution with NUANCE generated events not only consider the pions but it also takes care of other hadrons like kaons, protons, etc.

For the present method, we define a new observable E'_{had} which accounts for the energy of hadron shower in the final state (including recoil nucleon) and the energy of the initial state nucleon, including the rest mass, fermi momentum and binding energy. For rest of the analysis we use E'_{had} as hadron energy. Thus, energy of incoming neutrino, in the form of E'_{had} can be written as

$$E_\nu = E_\mu + E'_{had} \tag{3.9}$$

For the simulation, 1000 kton-year unoscillated NUANCE data, which is equivalent to 20 years exposure of 50 kton ICAL, has been propagated through the ICAL detector simulation. The produced hadron events are divided into various E'_{had} energy bins. In each E'_{had} energy bin, the hit distributions averaged over all direction are plotted. Each distribution is then fitted with Vavilov distribution function. Mean hits and σ obtained from the Vavilov fit of these distributions are then plotted against the hadron energy E'_{had} as shown in Figure 3.16. It can be seen from this figure that the mean number of hits obtained from NUANCE generated data follow the same linear pattern as we shown earlier for MC fixed energy analysis [Figure 3.11]. Dependence of Vavilov fit parameters with respect to E'_{had} are shown in Figure 3.18. The hadron energy resolution (σ/E) is obtained following the methodology mentioned in Section 3.5.

The hadron energy response obtained from the NUANCE-generated data contains the mixture of many hadrons that contribute to hadron shower at all energies. The fractional weights of different kinds of hadrons produced in neutrino interactions may, in principle, depend upon neutrino oscillations. In addition, the relative weights of events with different energy that contribute in a single energy bin changes because neutrino oscillations are energy dependent.

Table 3.4: The values of oscillation parameters used in the analysis.

Δm^2_{21}	$\sin^2(2\theta_{12})$	$\sin^2(2\theta_{13})$	$\sin^2(2\theta_{23})$	Δm^2_{31}
7.6×10^{-5} eV^2	0.86	0.113	1	2.39×10^{-3} eV^2

NUANCE events with the inclusion of neutrino oscillations are also generated to study

the effect of oscillations on the hadron energy resolution. The best-fit values of oscillation parameters used to generated the oscillated data are listed in Table 3.4. Resolution studies are also performed with this NUANCE oscillated data. Similar methodology was followed as for the unoscillated data to obtain the resolution. It was found that the resolutions obtained without and with oscillations are very close to each other as can be seen in Figure 3.17. Therefore, we can conclude that the hadron energy resolution can be considered to be insensitive to oscillations and variation of these oscillation parameters within their allowed ranges do not affect the energy resolutions.

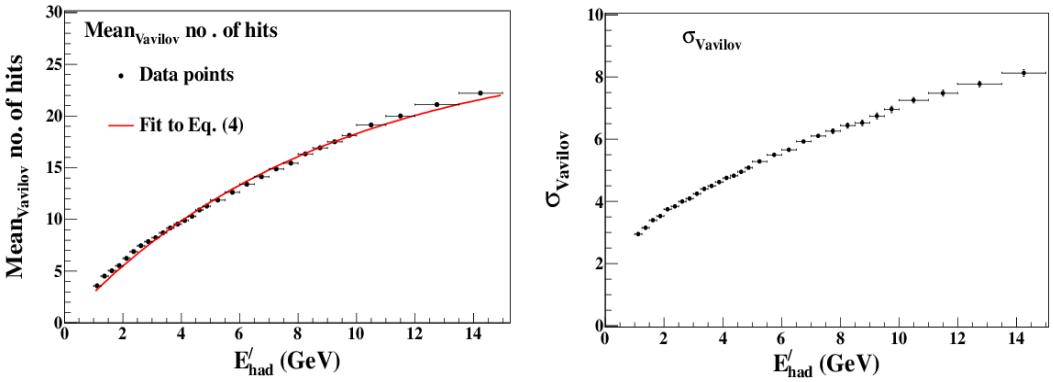

(a) Average hits from Vavilov fit

(b) σ from Vavilov fit

Figure 3.16: Average number of hits and deviation (σ) obtained from Vavilov fit to NUANCE generated hadron hit distributions.

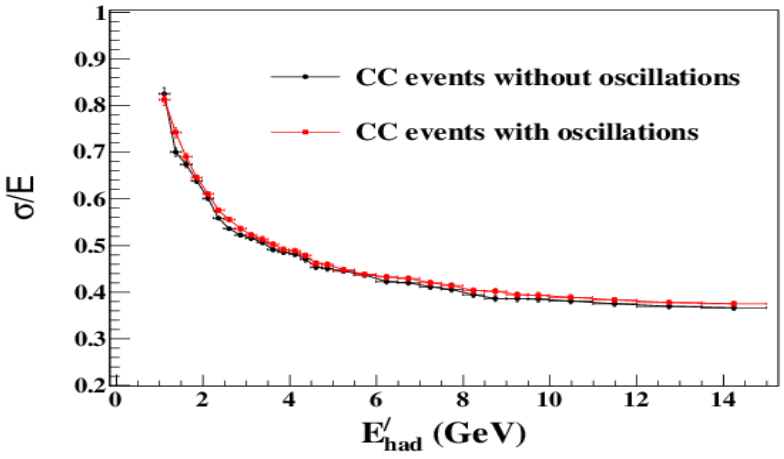

Figure 3.17: Hadron energy resolution obtained for CC hadron events with and without oscillations.

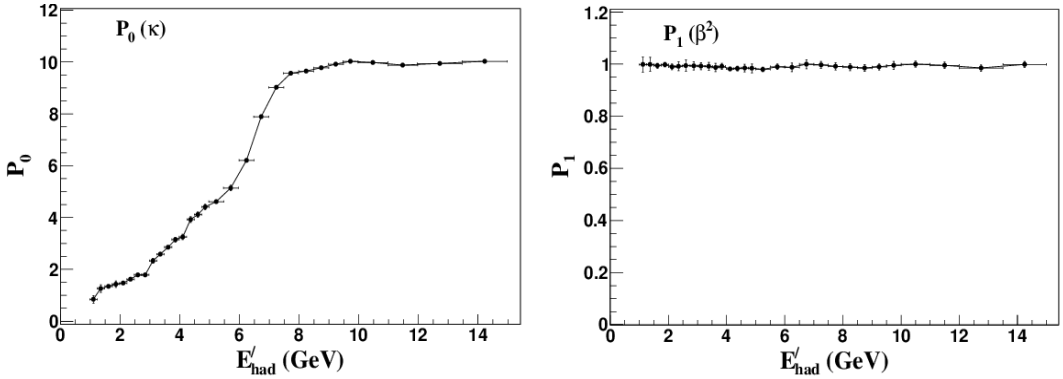

(a) parameter p0 (κ)

(b) parameter p1 (β^2

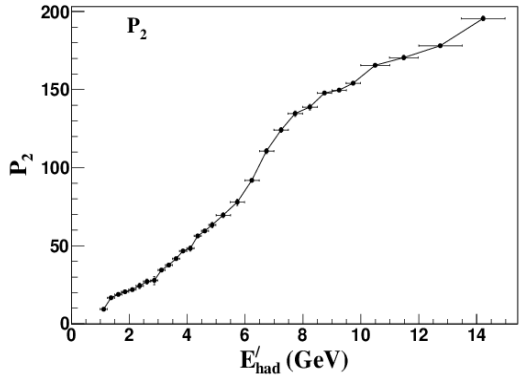

(c) parameter p2

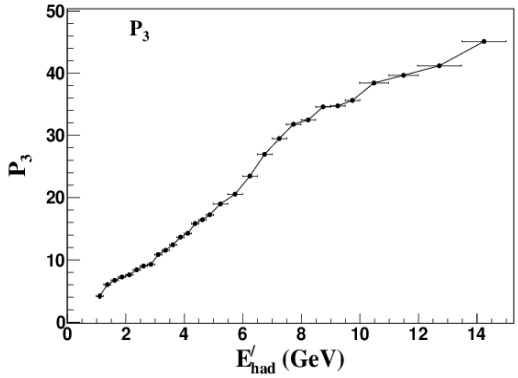

(d) paramter p3

Figure 3.18: Dependence of Vavilov parameters on incident pion energy from NUANCE data fit.

Production of hadron shower inside the ICAL detector also depends on the thickness of the absorber material i.e. iron. Number of hits in the hadron shower will decrease with increase in the iron plate thickness due to the loss of their energy in the target. This in turn may affect the hadron energy resolution of detector and hence can effect the precision measurement of neutrino oscillation parameters. To study the effect of iron thickness for ICAL detector for better detector performance, an analysis has been performed with iron plate thickness varying from 1.5 cm to 8.0 cm [108]. It has been found that the variation of iron plate thickness within the given range does not affect the hadron energy resolution significantly. The default configuration of ICAL with 5.6 cm thick iron plates gives the good energy resolution as any other optimized thickness and is also balanced against the other factors like stability, cost and ease of construction at present.

3.7 Results & Conclusions

Primary focus of the ICAL detector is to study the neutrino mixing parameters through the study of neutrino interaction products i.e. muons and hadrons. The energy resolution of these neutrino interaction products for ICAL detector plays an important role to find out correct information about the neutrino oscillations and their mixing parameters. To study the detector response for hadrons and muons, a GEANT4 simulation based on ICAL detector geometry has been performed. Muon leaves a clear track inside the detector while hadrons produce shower of hits near the interaction vertex. ICAL simulation study for muons indicate that the detector has a good response to muons due to its clear and clean track bending inside the magnetic field. Muon momentum resolution is found to be about 9-14% in the central region of the detector for the input momentum range 1-20 GeV/c; with an average reconstruction efficiency of about 80% and 98% relative charge identification efficiency. Also, the angular resolution of the detector is about a degree for momentum greater than 4 GeV/c which is very important to study the physics reach of ICAL detector.

The precise measurement of hadron energy in ICAL detector plays an important role in obtaining the ICAL physics results. In this chapter we discussed in detail the analysis performed for determining the hadron energy resolution of INO-ICAL detector. Energy resolutions of hadrons have been calibrated using hadron events generated through MC particle gun and NUANCE neutrino generator. Hadron events produced in the atmospheric muon neutrino interaction generated through NUANCE have been analyzed mainly for obtaining realistic detector resolution. Various possibilities and configurations like direction

and fixed vertex, smeared direction and smeared vertex are considered for MC analysis.

For MC studies, charged pions which have major contribution in hadron shower, are analyzed to obtain the detector response whereas NUANCE generated events analysis consider all hadrons produced in atmospheric neutrino interactions. MC fixed energy analyses has been performed in two ways; first with consideration of fixed vertex and different zenith directions and second with smeared vertex and direction. NUANCE based analysis has been performed with the hadron events generated in CC interaction of muon neutrinos with the ICAL detector. We analyzed the hit pattern of hadrons at ICAL under each of the above mentioned configurations. Obtained hadron hit distributions have been fitted with Vavilov distribution function to obtain the mean hit and width of the distribution. Resolution of the detector based on the linear behavior of energy and mean hit has been obtained and different fit function has been applied to estimate the dependence of resolution on the energy of the incoming hadrons. In summary, MC fixed vertex and direction analysis shows that for 1 GeV of hadron, the energy resolution for ICAL detector is about 50-60 $\%$ where as the smeared vertex and direction analysis for fixed energy hadrons shows that ICAL is able to achieve 80-85 $\%$ resolution for 1 GeV hadron and up to 40 $\%$ at 15 GeV. Results obtained from the NUANCE generated hadron events are consistent with the smeared vertex and direction analysis and are in the same resolution band. Thus, we can conclude that the realistic hadron energy resolution for INO-ICAL detector is approximately 85$\%$-40$\%$ for energy range 1-15 GeV. These results are quite promising and can be used to improve the physics potential of the ICAL detector. The present results on muon and hadron energy resolutions are used for further physics sensitivity study for INO ICAL detector which is described in Chapter 4.

Chapter 4

Atmospheric oscillation parameters sensitivity with INO-ICAL

4.1 Introduction

As discussed earlier in Chapter 1, despite various impressive progresses in neutrino physics made by the several neutrino experiments, there are still some unresolved issues yet to be addressed. Some of these issues are; right mass spectrum of neutrinos also known as neutrino mass hierarchy i.e. whether neutrino masses follow the Normal Hierarchy ($m1 < m2 < m3$; NH) or Inverted Hierarchy ($m3 < m1 < m2$; IH), determination of correct octant of θ_{23} i.e. whether $\theta_{23} > 45^0$ or $\theta_{23} < 45^0$ and determination of CP violating phase δ, etc. India-based neutrino Observatory (INO) is one of the planned experiments which will focus on resolving these issues through the observations of earth matter effects in atmospheric muon neutrinos. Re-confirmation of atmospheric neutrino oscillations, precision measurement of atmospheric ν_μ and $\bar{\nu}_\mu$ oscillation parameters, determination of mass hierarchy and deviation of θ_{23} from maximal mixing are the primary physics goals of the INO-ICAL experiment.

Neutrino (ν_μ) produces corresponding charged lepton (μ^-) and associated hadrons while undergoing Charged-Current (CC) interaction with the iron nuclei of the ICAL detector. Since the ICAL detector has efficient muon charge identification system and good muon energy resolution, it will accumulate sufficiently high statistics of atmospheric ν_μ and $\bar{\nu}_\mu$ events in several years of its running, which would allow a high precision measurement of the ν_μ and $\bar{\nu}_\mu$ disappearance due to oscillations. Also, the muon charge discrimination

ability of ICAL detector would help in the determination of correct neutrino mass spectrum. We present the precision measurement of atmospheric neutrino oscillation parameters ($|\Delta m^2_{32}|$ and $\sin^2\theta_{23}$) and θ_{23} deviation from the maximal mixing and mass hierarchy determination at ICAL detector using realistic detector resolutions in 3-flavor neutrino mixing scheme. These measurements can be done in several ways using different measurable quantities as observables which are as follows:

1. Muon energy and Muon direction
2. Neutrino energy and Muon direction
3. Neutrino energy and Neutrino direction

The physics reach of ICAL detector using muon energy and muon direction observables are discussed in Refs. [109, 110]. In this thesis, physics potentials of INO-ICAL detector are estimated using reconstructed neutrino energy and muon direction as observables.

4.2 Analysis

The analysis starts with the generation of the atmospheric neutrino events with NUANCE [99] neutrino generator and then events are binned according to energy (E) and angle of muons with respect to zenith direction (θ_μ). Various resolutions and efficiencies obtained by INO collaboration with GEANT4 [100] based simulation are applied to these binned events in order to obtain the reconstructed neutrino energy and muon direction. Finally, a marginalized χ^2 is estimated over the allowed ranges of neutrino parameters as listed in Table 4.1, after including the systematic errors. The details of the steps involved in the analysis are as follows:

4.2.1 Event Generation

The atmospheric ν_μ and $\bar{\nu}_\mu$ events are generated using NUANCE neutrino generator with the available 3-dimensional neutrino flux provided by HONDA et al.[111] using ICAL detector specifications. The interactions of atmospheric muon neutrino and anti-neutrino fluxes with the detector target are simulated by the NUANCE neutrino generator for 1000 years of exposure of 50 kt ICAL detector to keep the Monte Carlo fluctuations under control. For the purpose of quoting the final sensitivity, we normalize the 1000 years data to 10 years of ICAL exposure. The ICAL is highly sensitive to Charged-Current (CC) interactions where charged muons are produced along with the hadron shower, and can be

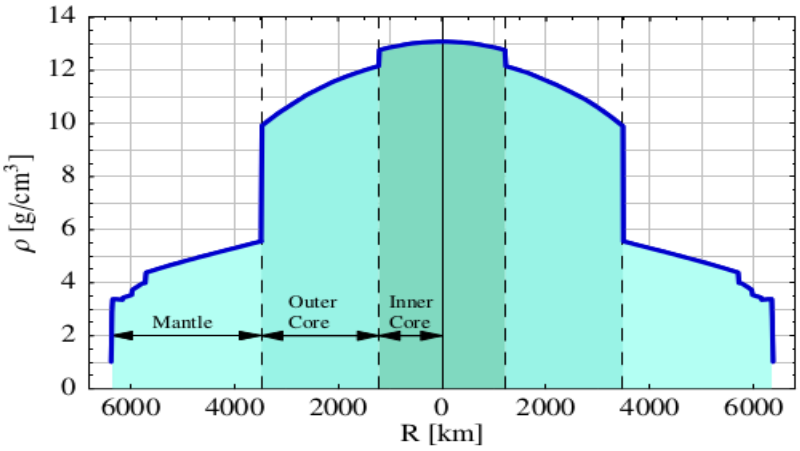

Figure 4.1: Earth matter density profile as mentioned in Ref. [117].

identified very clearly though the RPC detectors. Since the energy, angle resolutions and efficiency measurements for such events have been done by the INO collaboration [102, 112], and are available, only the events generated through CC interactions are considered for the present analysis. Since, the energy and angle measurements for muons from CC tau-decay and Neutral Current interactions are not available yet, we have neglected these channels for the present work.

4.2.2 Oscillation Effects & Event Selection

The neutrino oscillation can be incorporated into the NUANCE code to generate the oscillated neutrino flux at the detector for different values of oscillation parameters. However, this process requires large computational time and resources. Therefore, we simulate the interactions of atmospheric neutrinos with the detector in the absence of oscillations and the effect of oscillations is included by using the re-weighting algorithm described later in this section.

The propagation of atmospheric neutrinos through the earth matter effects largely affects the neutrino oscillation probabilities which are crucial for correct neutrino mass hierarchy measurements [113]-[116]. Therefore, for each neutrino event of a given energy E_ν and zenith direction θ_z, oscillation probabilities are estimated taking earth matter effects into account. The matter density profile of Earth is shown in Figure 4.1; taken from the Preliminary Reference Earth Model [117]. This model is based on worldwide seismological data and divides the Earth into several layers according to the matter densities.

Oscillation parameters	True values	Marginalization range
$\sin^2(2\theta_{12})$	0.86	Fixed
$\sin^2(\theta_{23})$	0.5	0.4-0.6 (3σ range)
$\sin^2(\theta_{13})$	0.03	0.02-0.04 (3σ range)
Δm^2_{21} (eV^2)	7.6×10^{-5}	Fixed
Δm^2_{32} (eV^2)	2.4×10^{-3}	(2.1-2.6) $\times 10^{-3}$ $(3\sigma\ range)$
δ	0.0	Fixed

Table 4.1: Best fit values of oscillation parameters used for analysis and their 3σ deviation range.

As mentioned in Chapter 1, atmospheric neutrinos are with wide range of flight path (L) from about 15 km for downward-going neutrinos to about 12000 km for upward-going neutrinos. These wide ranges in L and E help access to neutrinos with a wide range of L/E values. Figure 1.3(b) shows a sketch of a typical atmospheric neutrino experiment working principle. This distance is measured in terms of polar angle, defined from vertical direction at the detector commonly known as "zenith angle". $\cos\theta_z = 1$ is for neutrinos coming directly down, whereas $\cos\theta_z = -1$ describes fully upward going neutrinos. The path length traversed by neutrinos from the production point to the detector can be obtained as:

$$L = \sqrt{(R_{earth} + R_{atm})^2 - (R_{earth}\sin\theta_z)^2} - R_{earth}\cos\theta_z, \tag{4.1}$$

where R_{earth} is the radius of earth and R_{atm} is the average height of the production point of neutrinos in the atmosphere. We have used $R_{earth} \approx 6371$ km and $R_{atm} \approx 15$ km. Here, we assume that $\cos\theta_z = 1$ is the downward and $\cos\theta_z = -1$ is the upward direction for incoming neutrinos.

UP-Down Asymmetry : Up-Down ratio is an important tool to measure the oscillation effect for atmospheric neutrinos. In the absence of oscillations, the atmospheric neutrino flux from all directions (UP and Down) is expected to be similar. This ratio deviates from unity in the presence of oscillations. Thus, the ratio of events in the up-down direction for a given L/E, reflects the asymmetry of up-down flux due to oscillations, and hence, direct measurement of oscillation probability. We can define

$$\frac{U(up)}{D(down)} = \frac{No.\ of\ upward\ going\ events}{No.\ of\ downward\ going\ events} \tag{4.2}$$

First, we calculate the neutrino oscillation probabilities in framework of 3-neutrino

flavor mixing. A sample of theoretical oscillation probabilities calculated for ν_μ and $\bar{\nu}_\mu$ assuming normal and inverted neutrino mass hierarchies are shown in Figure 4.2 and in Figure 4.3 respectively, for the path length L $\approx$ 9700 km. The oscillation parameters used in the analysis are listed in Table 4.1.

In order to separate the muon neutrino and anti-neutrino events on the basis of their oscillation probabilities, each NUANCE generated unoscillated event is subjected to the oscillation randomly by applying the event re-weighting algorithm as described below:

For $\nu_\mu \rightarrow \nu_\mu$ channel:
For an unoscillated muon neutrino event of energy E and zenith angle θ_z, probabilities $P_{\nu_\mu\nu_e}$, $P_{\nu_\mu\nu_\tau}$ and $P_{\nu_\mu\nu_\mu}$ are calculated. A uniformly distributed random number (r), between 0 and 1 is associated with every interaction in NUANCE data without oscillations. If $r < P_{\nu_\mu\nu_e}$, the corresponding event is considered as a ν_e event and if $P_{\nu_\mu\nu_e} \leq r \leq (P_{\nu_\mu\nu_e} + P_{\nu_\mu\nu_\mu})$, the event is considered as a ν_μ event. The event is considered as a ν_τ event if $r \geq (P_{\nu_\mu\nu_e} + P_{\nu_\mu\nu_\mu})$.
For $\nu_e \rightarrow \nu_\mu$ channel:
Atmospheric ν_e may also change flavor to ν_μ due to oscillations. In order to include this contribution, we simulate the interactions of the ν_e flux with the detector in the absence of oscillations using NUANCE. Then we calculate the transition probability $(P_{\nu_e\nu_\mu})$ for each event. Again, a random number (r'), uniformly distributed in [0, 1] is associated with every event. If $r' < (P_{\nu_e\nu_\mu})$, we consider the event as a ν_μ event. Otherwise, we consider it as a ν_e event.

Hence, total event spectrum consists of ν_μ events coming from both the oscillation channels (i.e. $\nu_\mu \rightarrow \nu_\mu$ and $\nu_e \rightarrow \nu_\mu$) are considered for the analysis. The up-going type neutrinos traverse larger path length undergoing oscillation whereas the down-going ones with much shorter path-length have little chance to oscillate. Therefore, the ICAL detector can be visualizes as far (near) detector for the up-going (down-going) neutrinos. As a result, the ratio of up-going and down-going neutrinos (up/down) will roughly mimic the survival probability. A sample of unoscillated (down going) and oscillated (up-going) μ^- events (from $\nu_\mu \rightarrow \nu_\mu$ channel) as a function of $\cos\theta_\mu$ for the muon energy range of 1.8 - 2.8 GeV is shown in Figure 4.4.

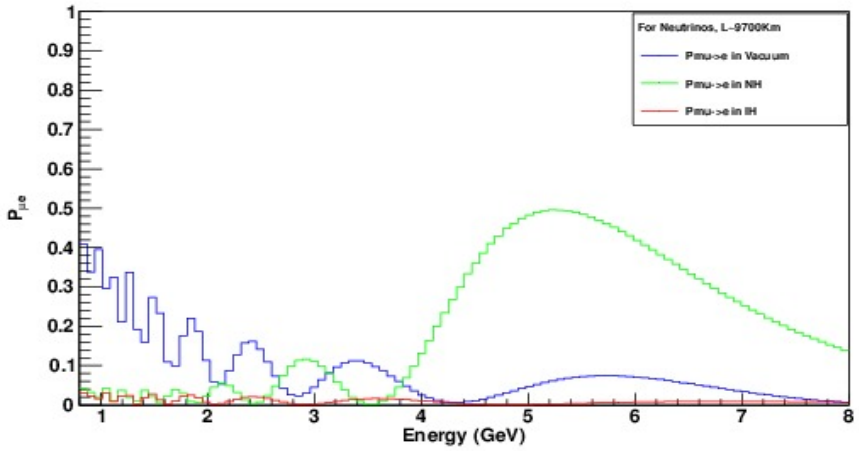

(a) $P(\nu_\mu \rightarrow \nu_e)$

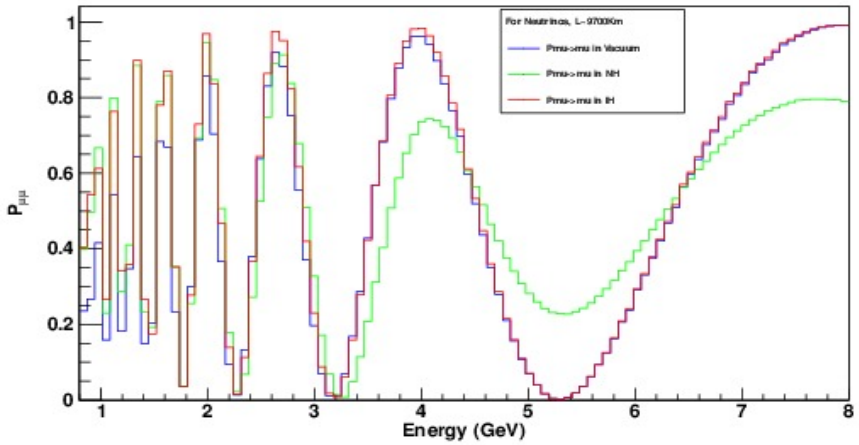

(b) $P(\nu_\mu \rightarrow \nu_\mu)$

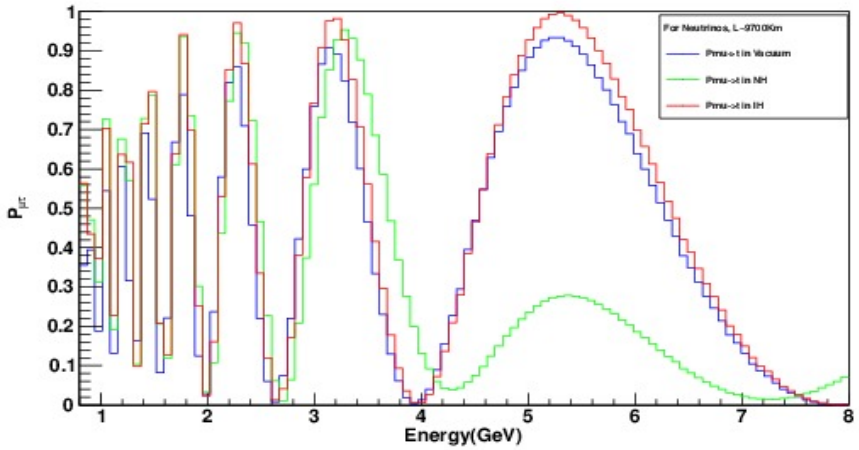

(c) $P(\nu_\mu \rightarrow \nu_\tau)$

Figure 4.2: Neutrino oscillation probabilities as functions of E_ν in vacuum (Blue), normal hierarchy (Green) and in the inverted hierarchy (Red) including matter effects (L$\sim$ 9700 Km).

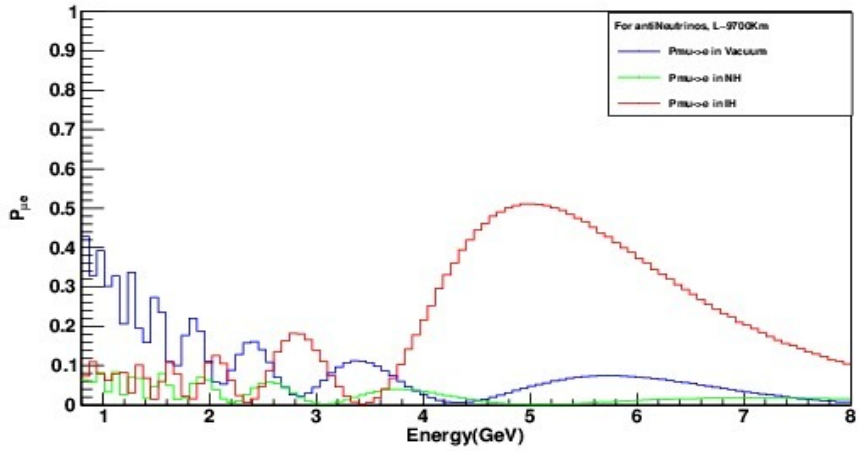

(a) $P(\bar{\nu}_\mu \to \bar{\nu}_e)$

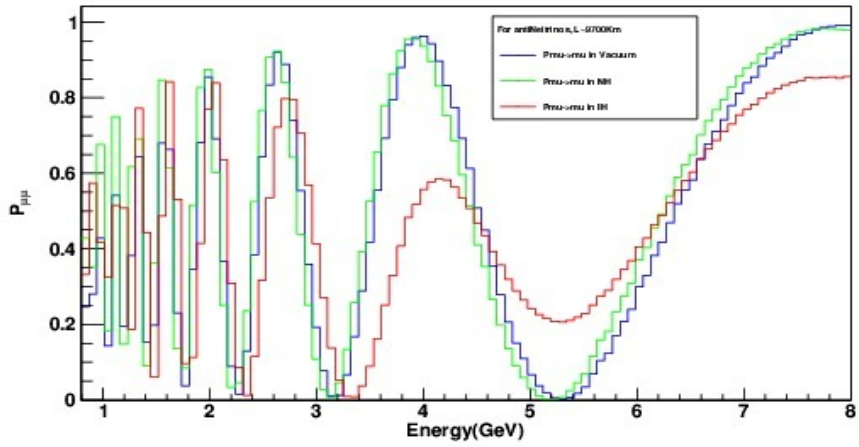

(b) $P(\bar{\nu}_\mu \to \bar{\nu}_\mu)$

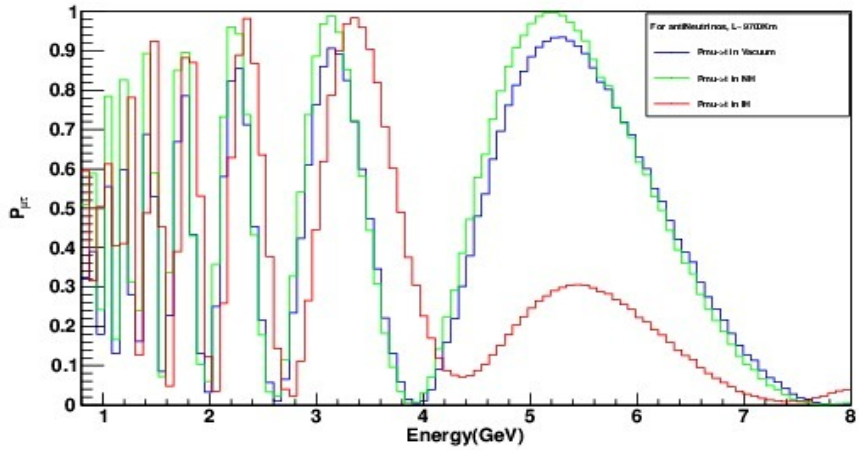

(c) $P(\bar{\nu}_\mu \to \bar{\nu}_\tau)$

Figure 4.3: Anti-neutrino oscillation probabilities as functions of $E_{\bar{\nu}}$ in vacuum (Blue), normal hierarchy (Green) and in the inverted hierarchy (Red) including matter effects (L$\sim$ 9700 Km.)

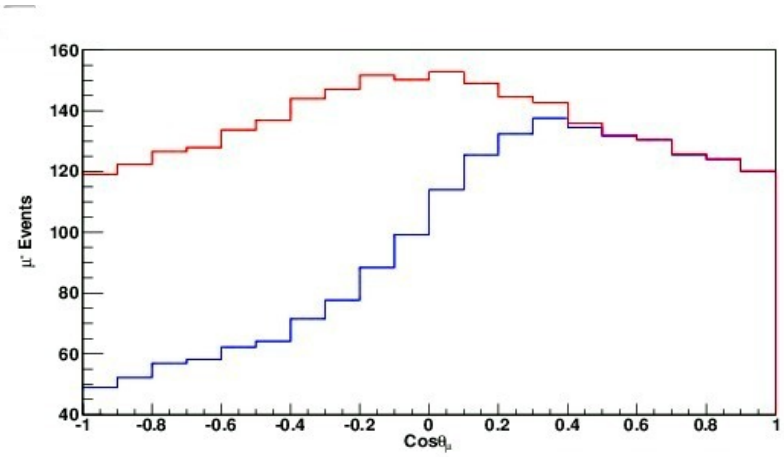

Figure 4.4: Unoscillated (Red) and Oscillated (Blue) μ^- events for the muon energy range 1.8 - 2.8 GeV for 10 years of exposure of ICAL detector.

4.2.3 Implementation of Detector Resolutions and Neutrino Energy Reconstruction

When atmospheric $\nu_\mu(\bar{\nu}_\mu)$ interact with the ICAL detector, it produces $\mu^+(\mu^-)$ and shower of hadrons. In order to extract the full information about the parent neutrino, information of muons along with that of the hadrons is needed. Since the neutrino energy cannot be measured directly, therefore, in the analysis presented here, the neutrino energy is obtained by adding the energy deposited by the muons and hadrons inside the ICAL detector. We then use this reconstructed neutrino energy (E_ν) and muon angle ($\cos\theta_\mu$) as observables for the χ^2 estimation.

Muon and hadron energy resolutions have been obtained by the INO collaboration as function of true energies and true directions of muons or hadrons using a GEANT4 [100] based code as mentioned in Chapter 3. Muons give a clear track of hits inside the magnetized detector, therefore the energy of muons can be reconstructed easily using a track fitting algorithm. It was observed that the muons energy reconstructed by the ICAL detector follows Gaussian distribution for $E_\mu \geq 1$ GeV, whereas it follows Landau distribution for $E_\mu < 1$ GeV. Figure 4.5 shows a comparison of μ^- events (from $\nu_\mu \rightarrow \nu_\mu$ channel) with and without applying ICAL detector resolution and efficiencies as a function of $\cos\theta_\mu$ for the muon energy range of 1.8-2.8 GeV. Since ICAL is not able to reconstruct the horizontal events ($cos\theta_\mu \approx 0$) due to its horizontal iron-RPC layers, these events show a dip near the horizontal directions as shown in Figure 4.5. In the present analysis, muon energy and angular resolutions are implemented by smearing true muon energy and direction

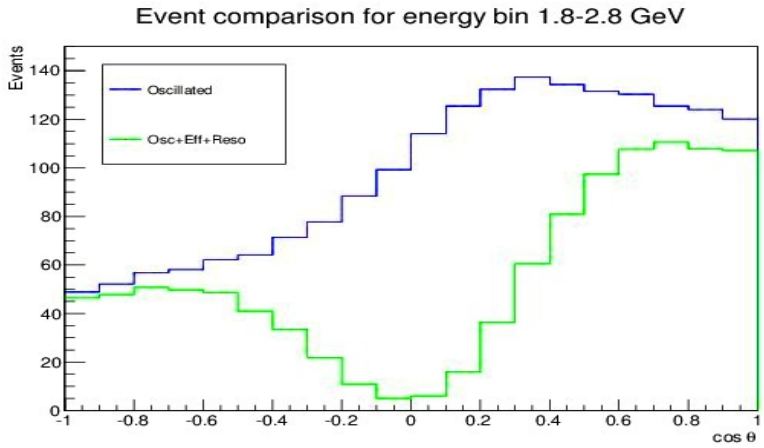

Figure 4.5: Oscillated μ^- events in absence (Blue) and in presence of INO resolutions and efficiencies (Green), for 10 years of exposure of ICAL detector.

of each μ^+ and μ^- event using the ICAL muon resolution functions [102]. True hadron energies are smeared using ICAL hadron resolution functions as mentioned in 3. Reconstructed neutrino energy is then taken as the sum of smeared muon and hadron energies. Figure 4.6 shows the true and reconstructed neutrino and anti-neutrino energies obtained from the $\nu_\mu \rightarrow \nu_\mu$ channel. Figure 4.7 shows the same for $\nu_e \rightarrow \nu_\mu$ channel. It can be seen that at lower incoming neutrino energies ($E_\nu \leq 1$), reconstruction of neutrino energy at ICAL is poor due to the poor detector resolutions in this regime. Since the muon direction reconstruction is extremely good for ICAL, and hadron direction information is not yet available, we have used the reconstructed muon directions in the χ^2 estimation.

The reconstruction and charge identification efficiencies (CID) for μ^- and μ^+ for ICAL detector are included into analysis by simply weighted each event with its reconstruction and relative charge identification efficiency. Though the CID efficiencies of ICAL detector are $\geq 90\%$ beyond $E_\nu \sim 1$ GeV [102], it is still possible that some muon events (say μ^+) are wrongly identified as of the opposite charge particle (say μ^-). So, the total number of events reconstructed as μ^- will increase by

$$N^{\mu^-} = N^{\mu^-}_{RC} + (N^{\mu^+}_{R} - N^{\mu^+}_{RC}), \tag{4.3}$$

where N^{μ^-} are the number of total reconstructed μ^- events. $N^{\mu^-}_{RC}$ are the number of μ^- events reconstructed and correctly identified in charge and $N^{\mu^+}_{RC}$ are the number of μ^+ events with their respective reconstruction and CID efficiencies folded in; whereas $N^{\mu^+}_{R}$ are the number of μ^+ events with the reconstruction efficiency only. Hence, $N_R - N_{RC}$

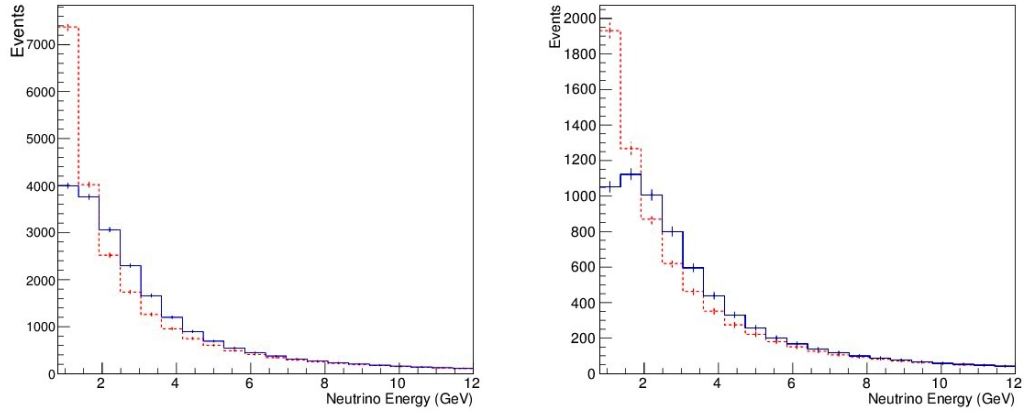

(a) For neutrino events (b) For anti-neutrino events

Figure 4.6: True neutrino energy (red-dashed line) and the reconstructed neutrino energy (blue-solid line) from nuance simulated data for (a) neutrino events and (b) anti-neutrino events, from $\nu_\mu \rightarrow \nu_\mu$ oscillation channel.

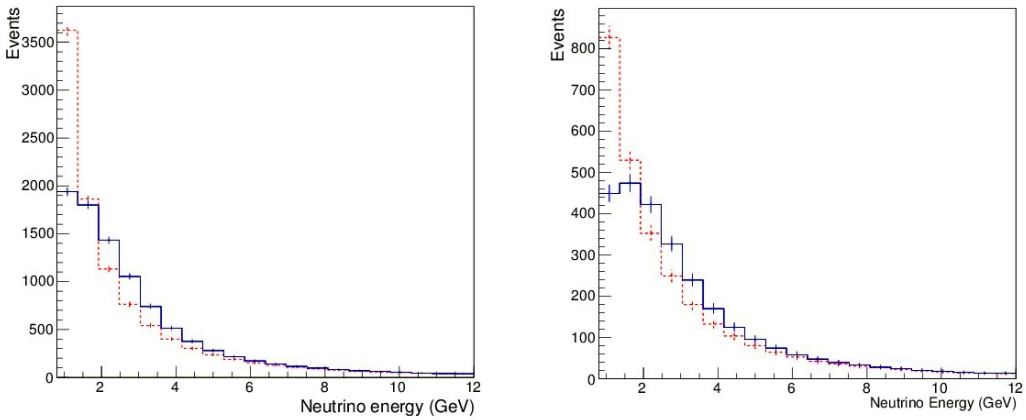

(a) For neutrino events (b) For anti-neutrino events

Figure 4.7: True neutrino energy (red-dashed line) and the reconstructed neutrino energy (blue-solid line) from nuance simulated data for neutrino events and for anti-neutrino events, from $\nu_e \rightarrow \nu_\mu$ oscillation channel.

Events	μ^- ($\nu_\mu \to \nu_\mu$)	μ^+ ($\nu_\mu \to \nu_\mu$)	μ^- ($\nu_e \to \nu_\mu$)	μ^+ ($\nu_e \to \nu_\mu$)	μ^- (Total)	μ^+ (Total)
Unoscillated	14208.64	5691.97	6207.19	2246.74	20415.83	7938.71
Oscillated	10249.14	4125.72	202.75	36.5	10451.89	4328.47
With Resolutions	9988.68	3934.89	197.7	34.5	10186.38	3969.39
With Efficiencies	4763.83	2123.73	106.00	17.319	4869.83	2141.049

Table 4.2: Number of Muon events from $\nu_\mu \to \nu_\mu$ and $\nu_e \to \nu_\mu$ channels at different stages of the analysis for 10 years of exposure of ICAL detector.

gives the fraction of reconstructed events that have their charge wrongly identified. Total reconstructed μ^+ events can be obtained using similar expression with charge reversal. Table 4.2 shows a sample of muon events counts on applying detector resolutions and efficiency for the muon energy range 0.8 - 10 GeV.

4.2.4 χ^2- Estimation

The sensitivity of the atmospheric neutrino oscillation parameters is estimated by minimizing the χ^2 for the neutrino data, simulated for the ICAL detector. The re-weighted events, with detector resolutions and efficiencies folded in, are binned into reconstructed neutrino energy and muon direction for the determination of χ^2. The data has been divided into total 20 varied neutrino energy bins in the range of 0.8 - 10.8 GeV. Since most of the atmospheric neutrino events come below the neutrino energy $E_\nu \sim 5$ GeV, we have a finer energy binning with a bin width of 0.33 GeV from 0.8 to 5.8 GeV with a total of 15 energy bins. The high energy events, i.e. from 5.8 GeV to 10.8 GeV, are divided into a total of 5 equal energy bins with bin width of 1 GeV. A total of 20 $\cos\theta_\mu$ direction bins in the range [-1, 1] with equal bin width, have been chosen. The bin size for the analysis has been optimized such that each bin contains at least one event. The above mentioned binning scheme is applied for both ν_μ and $\bar{\nu}_\mu$ events.

We use the maximal mixing, that is, $\sin^2\theta_{23} = 0.5$ as the reference value. The atmospheric mass square splitting is related to the other oscillation parameters, so for the precision study we have used Δm^2_{eff}, which can be written as [109, 118],

$$\Delta m^2_{eff} = \Delta m^2_{32} - (\cos^2\theta_{12} - \cos\delta \sin\theta_{23} \sin 2\theta_{12} \tan\theta_{23})\Delta m^2_{21}. \tag{4.4}$$

The other oscillation parameters (θ_{12}, Δm^2_{21} and δ) are kept fixed both for observed and

predicted events as the marginalization over these parameters has negligible effects on the analysis results. Since in our analysis, the event samples are distributed in terms of reconstructed neutrino energy and the muon zenith angle bins, we call these events as neutrino-like events, that is, we refer to N^{μ^-} as $N(\nu_\mu)$ and N^{μ^+} as $N(\bar{\nu}_\mu)$. The various systematic effects on the χ^2 have been implemented through five systematic uncertainties, *viz.* 20 % error on atmospheric neutrino flux normalization, 10% error on neutrino cross-section, a 5% uncertainty due to zenith angle dependence of the fluxes, an energy dependent tilt error, and an overall 5% statistical error. The effect of each systematic error on the precision measurement analysis is mentioned in Section 4.10.

The systematic uncertainties are applied using the method of "pulls" as outlined in Ref.[119]. Briefly, in the method of pulls, systematic uncertainties and the theoretical errors are parametrized in terms of set of variables ζ, called pull. The χ^2 function including the pull terms can be defined as [119]:

$$\chi^2(\overrightarrow{w}, \overrightarrow{\zeta}) = \chi^2_{data}(\overrightarrow{w}, \overrightarrow{\zeta}) + \chi^2_{pulls}(\overrightarrow{\zeta}), \tag{4.5}$$

where $\overrightarrow{w}$ denotes the oscillation parameter to which experiment under consideration has sensitivity and ζ is pull variable. The deviation of the experimental results from their theoretical predictions is defined by χ^2_{data} and the additional term χ^2_{pulls} gives penalties to the uncertainties of the systematics and the theoretical inputs from their nominal value. Due to the fine binning, some bins may have very small number of entries, therefore, we have used the poissonian definition of χ^2 given as

$$\chi^2(\nu_\mu) = min \sum_{i,j} \left(2(N^{th'}_{ij}(\nu_\mu) - N^{ex}_{i,j}(\nu_\mu)) + 2N^{ex}_{i,j}(\nu_\mu)(\ln \frac{N^{ex}_{i,j}(\nu_\mu)}{N^{th'}_{i,j}(\nu_\mu)}) \right) + \sum_k \zeta_k^2, \tag{4.6}$$

where

$$N^{th'}_{ij}(\nu_\mu) = N^{th}_{i,j}(\nu_\mu) \left(1 + \sum_k \pi^k_{ij} \zeta_k \right). \tag{4.7}$$

Here, N^{ex}_{ij} are the observed number of reconstructed μ^- events, as calculated from Eq. 4.3, generated using true values of the oscillation parameters as listed in Table 4.1 in i^{th} neutrino energy bin and $j^{th} \cos\theta_\mu$ bin. In Eq. 4.7, N^{th}_{ij} are the number of theoretically predicted events generated by varying oscillation parameters, $N^{th'}_{ij}$ shows modified events spectrum due to different systematic uncertainties, π^k_{ij} is the systematic shift in the events

of i^{th} neutrino energy bin and j^{th} $\cos\theta_\mu$ bin due to k^{th} systematic error. ζ_k is the univariate pull variable corresponding to the π_{ij}^k uncertainty. An expression similar to Eq. 4.6 can be obtained for $\chi^2(\bar{\nu}_\mu)$ using reconstructed μ^+ event samples. We have calculated $\chi^2(\nu_\mu)$ and $\chi^2(\bar{\nu}_\mu)$ separately and then these two are added to get total χ^2_{total} as

$$\chi^2_{total} = \chi^2(\nu_\mu) + \chi^2(\bar{\nu}_\mu). \tag{4.8}$$

We impose the recent θ_{13} measurement as a prior while marginalizing over $\sin^2\theta_{13}$ as

$$\chi^2_{ical} = \chi^2_{total} + \left(\frac{\sin^2\theta_{13}(true) - \sin^2\theta_{13}}{\sigma_{\sin^2\theta_{13}}}\right)^2. \tag{4.9}$$

The value of $\sigma_{\sin^2\theta_{13}}$ was taken as 10% of the true value of $\sin^2\theta_{13}$.

Finally, in order to obtain the experimental sensitivity for θ_{23} and $|\Delta m^2_{32}|$, we minimize the χ^2_{ical} function by varying oscillation parameters within their allowed ranges over all systematic uncertainties.

4.2.5 Precision Measurement of Neutrino Oscillation Parameters

We have derived the measurement contours of the atmospheric oscillation parameters in 3 flavor mixing using earth matter effect with reconstructed neutrino energy and muon direction observables. The precision measurement study has been performed under normal hierarchy consideration. The two dimensional confidence region of the oscillation parameters ($|\Delta m^2_{eff}|$, $\sin^2\theta_{23}$) are determined from $\Delta\chi^2_{ical}$ around the best fit. The resultant region is shown in Figure 4.8. These contour plots have been obtained assuming $\Delta\chi^2_{ical} = \chi^2_{min} + m$, where χ^2_{min} is the minimum value of χ^2_{ical} for each set of oscillation parameters and values of m are taken as 2.30, 4.61 and 9.21 corresponding to 68%, 90% and 99% confidence levels respectively for two degrees of freedom. Figure 4.9(a) depicts the one dimensional plot for the measurement of test parameter $\sin^2\theta_{23}$ at constant value of $|\Delta m^2_{eff}| = 2.4 \times 10^{-3}$ (eV^2) and Figure 4.9(b) for the $|\Delta m^2_{eff}|$ at constant $\sin^2\theta_{23} = 0.5$ at 1σ, 2σ and 3σ levels for one parameter estimation.

The precision on the oscillation parameters can be defined as:

$$Precision = \frac{P_{max} - P_{min}}{P_{max} + P_{min}}, \tag{4.10}$$

where P_{max} and P_{min} are the maximum and minimum values of the concerned oscilla-

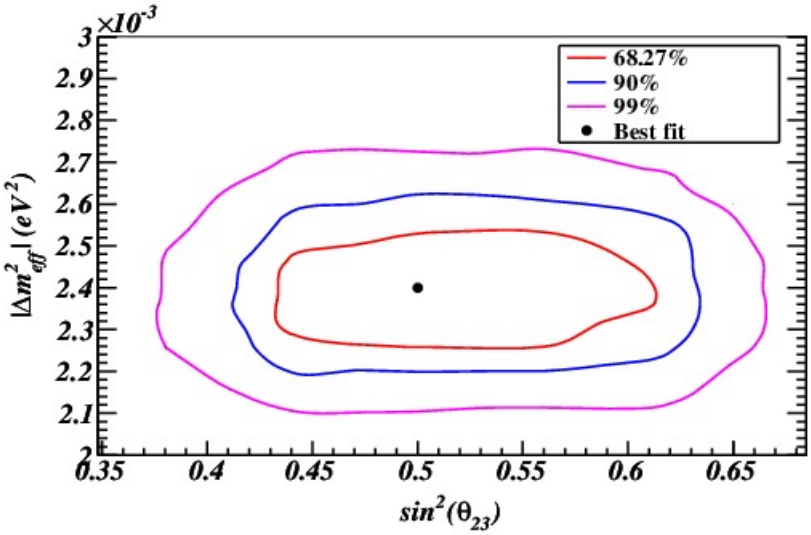

Figure 4.8: Contour plots for $\sin^2\theta_{23}$ and $|\Delta m^2_{eff}|$ measurements at 68%, 90% and 99% confidence level for 10 years exposure of ICAL detector.

tion parameters at a given confidence level.

The current study shows that ICAL is capable of measuring the atmospheric mixing angle $\sin^2\theta_{23}$ with a precision of 13%, 21% and 27%, at 1σ, 2σ and 3σ confidence levels respectively. The atmospheric mass square splitting $|\Delta m^2_{32}|$ can be measured with a precision of 4%, 8% and 12% at 1σ, 2σ and 3σ confidence levels respectively. These numbers show an improvement of 20% and 23% on the precision measurement of $\sin^2\theta_{23}$ and $|\Delta m^2_{32}|$ parameters respectively at 1σ level over muon energy and muon direction analysis [110]. These results shows that the inclusion of hadron information together with muon information significantly improves the capability of ICAL detector for the estimation of oscillation parameters. These results may further be improved by including the neutrino direction in the χ^2 definition.

4.2.6 Systematic Uncertainties and Their Effects on Precision Measurement

In this section, we will explore the effect of each applied systematic error on the achievable precision of atmospheric neutrino oscillation parameters. As mentioned in Section 4.2.4, we have used 20% error on neutrino flux normalization, 10% crossection error and 5%

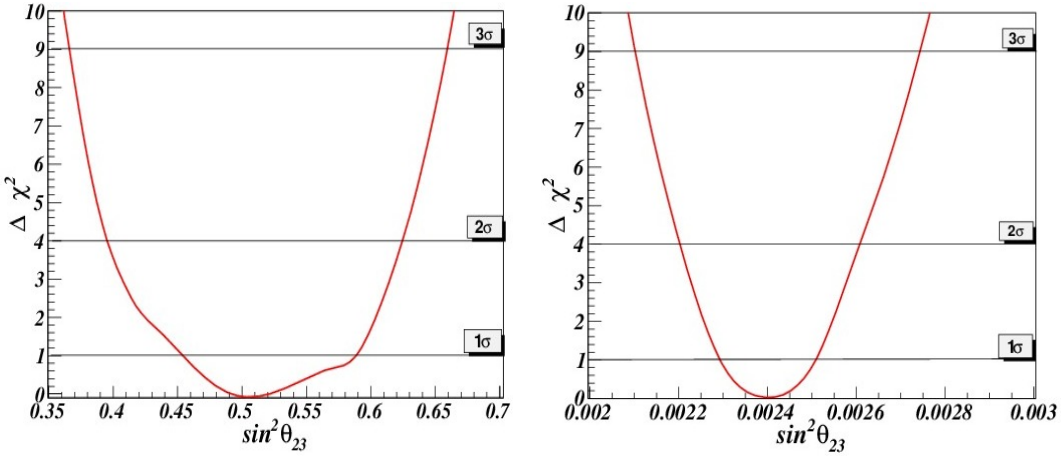

(a) χ^2 Vs. $\sin^2\theta_{23}$ (b) χ^2 Vs. $|\Delta m^2_{32}|$

Figure 4.9: (a) $\Delta\chi^2$ as a function of test values of $\sin^2\theta_{23} = 0.5$, and (b) $\Delta\chi^2$ as a function of input values of $|\Delta m^2_{32}|$.

overall systematic errors. These three uncertainties are taken as constant for each energy and $\cos\theta$ bin. We have applied uncertainty on the zenith angle dependence of the flux as 5 $\%$ of average of each $\cos\theta$ bins. The energy dependent tilt error which has been calculated using power law (Eq. 4.11) as given in [110, 119] is also included in the analysis.

$$\phi_\delta(E) = \phi_0(E)\left(\frac{E}{E_0}\right)^\delta \approx \phi_0(E)\left(1 + \delta\, ln\frac{E}{E_0}\right) \tag{4.11}$$

where, $\phi_0(E)$ is the predicted atmospheric neutrino flux and $\phi_\delta(E)$ is the shifted neutrino flux. E_0 = 2 GeV and δ is the 1σ systematic tilt error, which has been taken as 5$\%$. The difference between $\phi_\delta(E)$ and $\phi_0(E)$ is then considered as actual shift in neutrino spectrum due to tilt errors.

We estimate the effect of each systematic uncertainty on the central value of χ^2 one by one. Figure 4.10(a) shows the effect of each uncertainty on the ($|\Delta m^2_{eff}|$, $\sin^2\theta_{23}$) contour plot at 90$\%$ confidence level. It is to be noted that the contour plots shown here are generated using muon energy and muon direction as observable in χ^2. These uncertainties are added separately, not in quadrature. As a crosscheck of our procedure, we have plotted together the ($|\Delta m^2_{eff}|$, $\sin^2\theta_{23}$) contour from the first two uncertainties separately through the pull method, and the contour obtained from combining these two uncertainties in quadrature before providing this as a single systematic in χ^2. The results are shown in Figure 4.10(b), where we consider 20$\%$ normalization error and 10$\%$ crossection er-

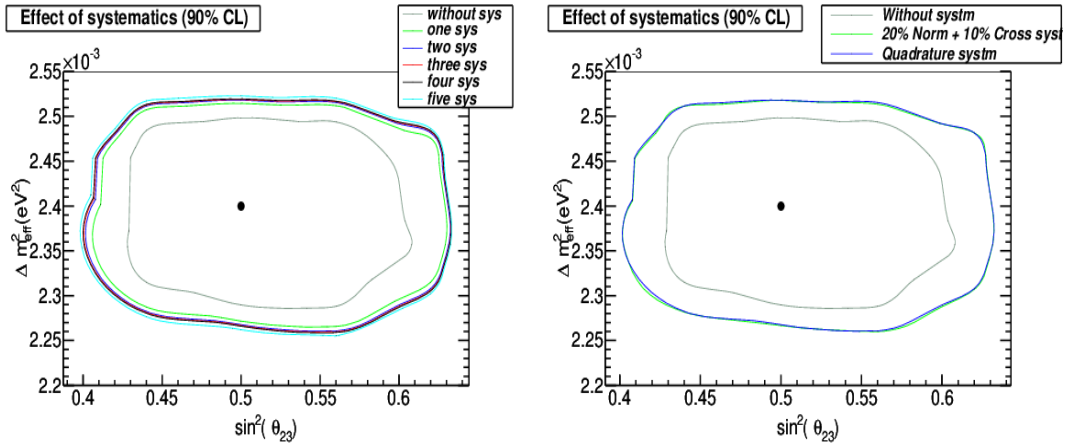

(a) Inclusion of systematics (b) Effects of systematic with quadrature addition

Figure 4.10: Contour plots for 90% confidence level with and without (a) all systematic errors as mentioned in Section 4.2.4, and (b) with the effect of normalization and crossection uncertainty in quadrature addition.

rors separately and then as a single combined error, which is equal to quadrature sum of these two errors. It can be seen from this figure that the two results agree within statistical uncertainties and therefore, proves that our systematic errors are uncorrelated.

4.2.7 Octant Sensitivity Study at INO-ICAL

The sensitivity to the octant of atmospheric mixing angle θ_{23} is an important issue which is to be resolved by atmospheric neutrino experiments. Recently, MINOS experiment claimed for non-maximal value for θ_{23} [58]. According to octant degeneracy, there are two possible solutions; one is octant of θ_{23} is below 45° which is known as Lower Octant (LO) and other possibility is that θ_{23} is above 45° which is known as Higher Octant (HO). We have performed the octant sensitivity study in context of INO-ICAL detector using neutrino-like events. Octant studies are performed under normal hierarchy consideration. The significance of ruling out the wrong octant is given by

$$\Delta\chi^2 = \chi^2(false\ octant) - \chi^2(true\ octant), \tag{4.12}$$

where χ^2 (true octant) has been obtained by considering both the predicted and observed event spectrum in true octant while the χ^2 (false octant) has been obtained by assuming predicted events with true octant and observed event with false octant. Note that for this

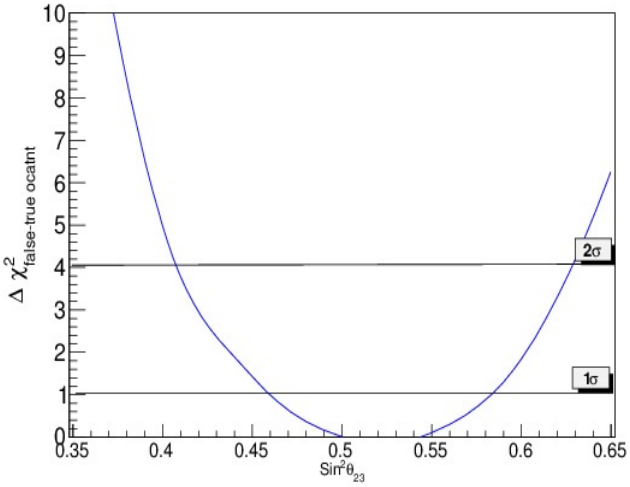

Figure 4.11: $\Delta\chi^2_{false-true\ octant}$ for different input values of $\sin^2\theta_{23}$.

study we kept all the oscillation parameters fixed and analysis has been performed for different true values of $\sin^2\theta_{23}$.

Figure 4.11 shows the χ^2 plot for the identification of octant sensitivity for different true values of $\sin^2\theta_{23}$ assuming Normal hierarchy. From this figure, it is clear that using neutrino energy and muon direction observable as two dimensional observables, ICAL can identify the lower octant when $\sin^2\theta_{23} < 0.46$ and $\sin^2\theta_{23} < 0.40$ with 1σ and 2σ confidence levels respectively assuming Normal Hierarchy (NH) is true. Similarly, with the same assumption, higher octant can be identified when $\sin^2\theta_{23} > 0.58$ and $\sin^2\theta_{23} > 0.63$ with 1σ and 2σ confidence levels respectively. It has also been observed that ICAL sensitivity deteriorates on approaching the θ_{23} close to its maximal mixing ($\sin^2\theta_{23} = 0.5$). The 2-dimensional contour plots in $\sin^2\theta_{23}$ and Δm^2_{32} plane have been plotted for the clear view of significance levels for the octant sensitivity assuming true lower octant ($\sin^2\theta_{23} = 0.4$) and true higher octant ($\sin^2\theta_{23} = 0.65$) [see Figure 4.12]. As we mentioned earlier that this analysis has been performed using Monte Carlo method, the effect of randomness is clearly observed in the form of fluctuations in the contour plots. It is clear from Figure 4.12 that ICAL is able to determine the deviation of θ_{23} from the maximal mixing up to 2σ confidence level.

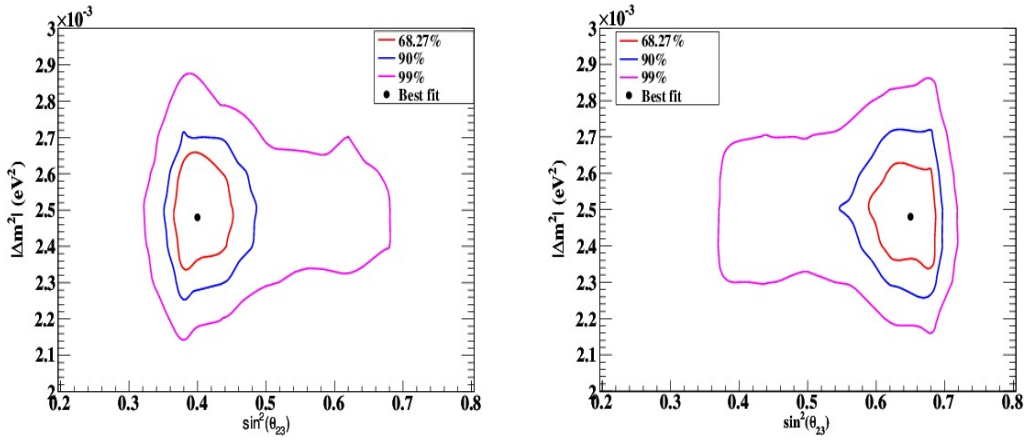

(a) When $\sin^2\theta_{23} = 0.4$ (LO) is true

(b) When $\sin^2\theta_{23} = 0.65$ (HO) is true

Figure 4.12: Contour plots indicating 68%, 90% and 99% CL (a) at true $\sin^2\theta_{23} = 0.4$, and (b) at true $\sin^2\theta_{23} = 0.65$ assuming NH is true for 10 year of ICAL exposure.

4.2.8 Mass Hierarchy Studies at INO-ICAL

The neutrino mass hierarchy whether normal or inverted is of great interest in today's neutrino physics. For non zero value of θ_{13}, the hierarchy determination is possible through the earth matter effects on the oscillation. Thus, the experiments sensitive to earth matter effects can probe the neutrino mass hierarchy. Since atmospheric neutrinos cover a large path length and earth matter effects through their propagation, studies of these neutrinos are important for mass hierarchy determination. Also, the matter effects in neutrino oscillations are sensitive to the sign of Δm^2_{32}. ICAL at INO has a unique capability to easily distinguish μ^- & μ^+ events and hence ν_μ & $\bar{\nu}_\mu$ events with high charge discrimination efficiencies. This makes it possible to determine the correct neutrino mass spectrum using these atmospheric muon neutrino events. The ICAL experiment is insensitive to δ [109], but it has been observed that the INO mass hierarchy results together with other experimental results can only help to determine the value of δ [120].

We have performed the mass hierarchy sensitivity study for INO-ICAL detector using reconstructed neutrino energy and muon angle observables. For the present analysis, all the oscillation parameters (θ_{12}, θ_{23}, Δm^2_{32}, Δm^2_{21} and δ) are kept fixed both for observed and predicted events. Reconstruction of neutrino energy, muon directions, the implementation of detector resolutions and efficiencies have been done exactly as mentioned in previous sections. We evaluate the χ^2 for both normal hierarchy (NH) and inverted hierarchy (IH)

for neutrino and anti-neutrinos separately and the total χ^2 is then defined as the sum of $\chi^2(\nu_\mu)$ and $\chi^2(\bar{\nu}_\mu)$ as

$$\chi^2 = \chi^2(\nu_\mu) + \chi^2(\bar{\nu}_\mu). \tag{4.13}$$

We minimize this χ^2 function over all systematic uncertainties.

The mass hierarchy study has been performed by taking both the assumptions (True Normal and True Inverted hierarchies) into consideration for a given detector run time. These are explained as below:

(1) True Normal Hierarchy study : For this study, first we simulate the neutrino-like events for normal mass hierarchy for desired exposure at the best fit values of the oscillation parameters given in Table 4.1. The observed data is then fitted with the true (Normal) and false (Inverted) hierarchy using a binned χ^2 analysis. Finally, in order to obtain the experimental sensitivity, the significance of ruling out the wrong hierarchy is given by

$$\Delta\chi^2 = \chi^2_{IH} - \chi^2_{NH}. \tag{4.14}$$

(2) True Inverted Hierarchy study: For this study, the predicted neutrino-like event spectrum is fitted with the inverted hierarchy and the observed data for the same oscillation parameters is first fitted with inverted hierarchy and then with normal hierarchy which is considered as false hierarchy now. The χ^2 is now defined as

$$\Delta\chi^2 = \chi^2_{NH} - \chi^2_{IH}. \tag{4.15}$$

We perform the hierarchy study for maximal mixing of θ_{23} i.e. $\sin^2\theta_{23} = 0.5$ and in the lower octant ($\sin^2\theta_{23} = 0.4$) and for higher octant ($\sin^2\theta_{23} = 0.6$). The final mass hierarchy sensitivity for different run time has been obtained and are shown in Figure 4.13.

Here, it is to be noted that we applied the resolutions using the Monte Carlo analysis, therefore minimum χ^2 for a given true hierarchy is not equal to zero but have some minimum value due to the randomness involved in the procedure. It is clear from Figure 4.13 that for maximal mixing ($sin^2\theta_{23} = 0.5$), ICAL is able to discriminate between both the hierarchies up to 2.5σ confidence level for an exposure of 10 years. This result is in agreement with the earlier ICAL results for muon energy and muon direction analysis [109].

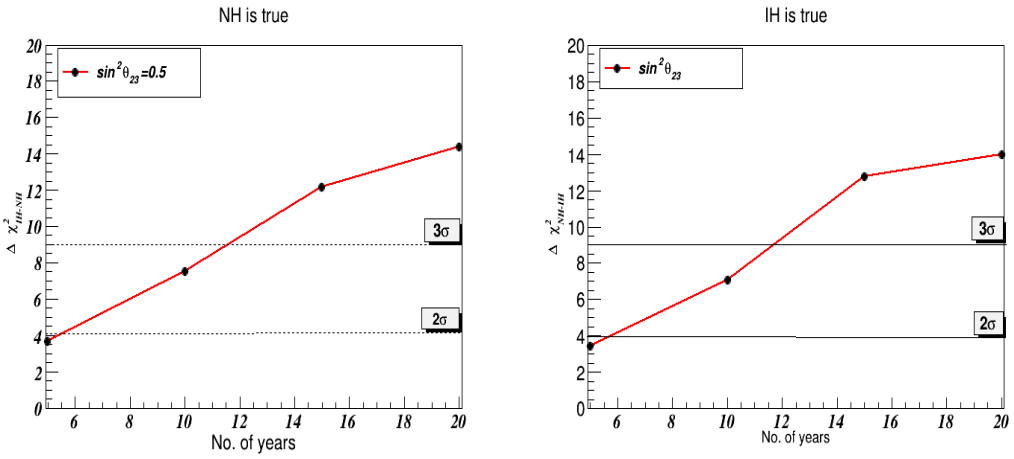

(a) NH is true (b) IH is true

Figure 4.13: Mass hierarchy sensitivity for different years of ICAL exposure at maximal mixing; $\sin^2\theta_{23} = 0.4$, m for true Normal hierarchy and for true Inverted hierarchy.

4.3 Results & Conclusions

In this chapter, we have discussed the potentials of atmospheric neutrino oscillations in the context of India-based Neutrino Observatory. Atmospheric neutrino events for 1000 years of running ICAL detector are simulated from NUANCE neutrino generator which incorporates all the detector geometry. To save the large computational time, events are generated without neutrino oscillation effects i.e. only unoscillated events are generated. Since ICAL is highly sensitive for Charged-Current (CC) neutrino interaction, the present analyses consider only the CC neutrino interactions. These unoscillated events are then subjected to the oscillation effects with a well defined re-weighting algorithm suitable for any set of oscillation parameters. Analysis has been performed in the framework of 3-neutrino flavor mixing and by taking earth matter effect into account. Final sensitivity has been estimated for 10 years of exposure of ICAL detector which is obtained by scaling down the 1000 years data to 10 years data in order to minimize the statistical fluctuations. Oscillated neutrino-like events are then distributed in fine binning of reconstructed neutrino energy and muon directions. Atmospheric ν_μ (or $\bar{\nu}_\mu$) interactions with the ICAL detector produce charged muons and hadrons. The muon and hadron information are crucial for the complete information of interaction neutrinos. Recently, it has been shown that including hadron information together with the muon events improves the ICAL potential for the measurement of neutrino mass hierarchy [121, 122]. Therefore, the response of muon and hadron for ICAL detector

has been used for the reconstruction of neutrino energy. The oscillated event spectrum is then folded with the muon and hadron reconstruction efficiencies, muon charge identification efficiencies, energy resolution of muons and hadrons and the muon angle resolution functions obtained from ICAL simulations. We present the effect of these resolutions and efficiencies over the total oscillated events as a function of muon direction. We have studied the ICAL detector capability for the precision measurement of neutrino oscillation parameters, octant sensitivity and mass hierarchy determination at ICAL detector using neutrino energy and muon angle as observables. For the measurement of precision of atmospheric neutrino oscillation parameters, a marginalized χ^2 analysis in fine bins of reconstructed neutrino energy and muon angle has been performed using realistic detector resolutions and efficiencies. The effect of various systematic uncertainties have also been included in the analysis. We conclude that by using reconstructed neutrino energy and muon direction there is an average improvement of about 20% on the precision measurement of both the parameters ($\sin^2\theta_{23}$ and $|\Delta m^2_{32}|$) over muon energy, muon angle analysis [110]. The octant sensitivity and mass hierarchy sensitivity studies has been performed with fixed values of oscillation parameters. The octant study shows that ICAL is able to discriminate the octant of θ_{23} with a significance of 2σ for 10 year exposure. For the mass hierarchy study, data is generated for true values for the oscillation parameters and a given neutrino mass hierarchy and then fitted with the wrong hierarchy. The results of mass hierarchy has been shown as a function of the exposure in ICAL. The obtained results show that the ICAL is able to determine the right mass hierarchy with more that 2.5σ confidence level with 10 years of exposure. The mass hierarchy determination using the present analysis does not improve significantly over the muon energy and muon angle only analysis. Moreover, this study is also a demonstration of the fact that the ICAL experiment has the capability of harnessing hadron information to further improve the measurement of oscillation parameters.

Chapter 5

Conclusions & Future Outlook

The India-based Neutrino Observatory (INO) is an approved project aimed at building a world-class underground laboratory to study mainly the neutrino properties. A magnetized Iron calorimeter detector is going to be the main experiment at this facility. The ICAL experiment has capability to address the current unresolved issues in neutrino physics using atmospheric neutrino source through the earth matter effects. A key feature of this experiment is its charge identification capability, through an applied magnetic field strength of $\sim$1.5 Tesla. This enables ICAL to distinguish between atmospheric neutrino and anti-neutrinos interaction by identify the charge of interaction products which is crucial for the determination of neutrino mass hierarchy. The ICAL detector will consists of stack of 151 horizontal layers of iron slab interleaved within 4 cm gap for the Resistive Plate Chambers (RPCs), which are the active detector elements. The research work described in this thesis is a part of the effort to develop the RPC detectors using different electrode materials and its operation under varied environmental conditions.

RPC is a fast tracking detector basically made up of two high resistive electrodes and works on the principle of ionization. Development of detector technology and understanding the characteristic properties of electrodes are the key elements for the improvement of high rate Resistive Plate Chambers. Performance of a RPC detector such as efficiency, time resolution and aging effects mainly depends upon the resistivity and surface smoothness of the electrode plates. We characterized different electrode materials like Glasses *viz.* Asahi, Modi & Saint Gobain and Bakelites *viz.* Formica & Hylam Bakelite for constructing RPC detectors. The properties such as bulk resistivity, surface resistivity and surface smoothness of these electrode samples have been measured carefully.

From our studies, we found that the glass electrodes have greater bulk resistivity compared to the Bakelite electrodes. The Saint Gobain glass has the maximum bulk resistivity of the order 5×10^{12} Ω-cm at operating voltage 6 kV on an average among all the electrode samples. Asahi and Modi are found to be having similar bulk resistivity and is approximately 1.5×10^{12} Ω-cm at 5 kV applied voltage. The Bakelite electrodes are having bulk resistivity of the order $\sim 10^{10}\Omega$-cm. From the surface resistivity measurements of all the samples, we showed that the surface resistivity of Asahi glass is uniform over most of the surface area whereas there are significant variations in the surface resistivity distribution of the Saint Gobain and Modi glass. The Bakelite electrodes have even wider surface resistivity variations. It can be concluded that the bulk resistivity of Saint Gobain glass is maximum while Asahi glass having the smoothest surface among all the glass electrodes.

Further, the RPC detectors of dimension 30 cm $\times$ 30 cm were fabricated by following standard procedure using the electrodes mentioned above. For each RPC, two resistive electrodes are separated with a gas gap of 3 mm by means of highly insulated polycarbonate spacers. The fabricated RPCs were then characterized for efficiency, count rate and leakage current under different temperature and humidity variations. The performance of each RPC with different gas compositions has also been analyzed. From the efficiency study of each RPC, we conclude that the efficiency under different gas compositions is similar for all the types of the glasses and is above 95%. The efficiency of the RPCs made from Formica Bakelite, which we found best among all the Bakelite samples, varied between 80$\%$ and 90$\%$. All these measurements are performed at the normal pressure, relative humidity varying from 40% to 45% and temperature varying between $19^{\circ}C$ to $21^{\circ}C$.

The noise rate and leakage current measurements of all RPCs show that these properties highly depends on the smoothness of the electrode plates and on the fraction of SF_6 gas in the gas mixture. We observed that noise rate and leakage current are minimum for Asahi glass which have smoothest surface among all samples. Noise rate as expected is maximum in the absence of SF_6 and decreases with increase in fraction of SF_6 in the gas mixture.

We perform the studies for the discriminator threshold and found the threshold of 50 mV as optimum value for further studies. The study on variation of temperature and humidity shows that with increase in temperature from 18 to 21 degree centigrade and relative humidity varying approximately between 35% and 45%, there is not much effect on leakage current and noise rate. But, further increasing the temperature to $24^{\circ}C$, both the leakage current and noise rate increases. We did not find any considerable effect of temperature and relative humidity on efficiency.

In conclusion, we can say that the performance wise, glass electrodes are much better than the Bakelite electrodes; especially, Saint Gobain and Asahi glasses are suitable for the INO-ICAL RPCs in terms of most of the parameters that we studied. On the basis of studies performed with different gas compositions we conclude that $R134a$ (95.0%), C_4H_{10} (4.5%), SF_6 (0.5%) gas composition is acceptable for RPCs operation. Temperature and humidity variation studies show that it is necessary to keep the temperature around 20^0C and relative humidity under control for better RPC performance. However, these studies are performed on small prototypes RPCs of size 30 cm $\times$ 30 cm, and we are in the process of constructing actual size INO-ICAL RPCs. We will further continue our studies on large size detectors for these parameters along with many other characterization studies of RPC like time resolution, charge spectra and multi hit performance of each read out channel of RPC (cross talk studies).

This thesis also discuss the ICAL detector response for muons and hadrons in the GeV energy range which is based on GEANT4 simulation studies. A detail description of hadron energy resolution of ICAL detector has been shown. Based on the realistic and effective detector resolutions and efficiencies for muons and hadrons, the physics potentials of the ICAL detector are also determined and are part of this thesis work. The ICAL detector is mainly sensitive to atmospheric muon neutrinos and anti-neutrinos. These neutrinos when undergo Charged-Current (CC) and Neutral Current (NC) interactions with iron target of the detector, muons and hadrons are produced. Muon gives clear track inside the detector and hadron produces shower hits. Muon energy and direction can be determined by its path length, but hadron energy can only be calibrated by taking shower hits into account. A GEANT4 based simulation study with the ICAL detector specifications was performed to find out the hadron energy resolution of ICAL detector. Monte Carlo (MC) single pion events of fixed energies and hadrons generated in atmospheric ν_μ interactions using NUANCE neutrino generator for the energy range 1-15 GeV have been analyzed. For MC studies, the charged pions which have major contribution in hadron shower, are analyzed mainly to obtain the detector response whereas NUANCE generated events analysis consider all hadrons produced in atmospheric neutrino interaction. The obtained hadron hit distributions have been fitted with various fitting functions to get the mean energy of the hadrons. Various fitting function has been applied to calibrate the resolution as a function of energy for the detector.The best fit was obtained using Vavilov distribution function. Resolution of the detector based on the linear behavior of energy and mean hits has been obtained. Resolution of the detector based on this proportionality behavior may be defined

as $\sigma/E = \Delta E/E$, where σ is the width and E is the hadron energy in GeV, corresponds to mean number of hits from the distribution. On the basis of the hadron calibration we conclude that the ICAL is able to reconstruct the hadron energy resolution from 85% (at 1GeV) to 35%(at 15 GeV). These resolution can further be improved with the improvement in the track reconstruction algorithm and fitting techniques. Further, hadron direction resolution is also an important parameter which is essential for the reconstruction of actual direction of neutrinos. The work on this area is underway in the INO collaboration and will be included in future works.

The physics potential of INO-ICAL detector based on results obtained on detector resolutions and efficiencies have been estimated. We performed an analysis for the determination of INO-ICAL sensitivity for the precision measurement of atmospheric neutrino oscillation parameters, octant of θ_{23} and mass hierarchy with the muon neutrino events, generated with monte carlo NUANCE event generator. The analysis has been performed using neutrino energy and muon direction as the observables. The realistic resolutions and efficiencies obtained from a GEANT4-based simulation have been used to reconstruct the neutrino energy and muon direction. Various systematic uncertainties from neutrino fluxes and cross sections have also been included, but the background effects have not been considered. It is well known that a significant background may arise due to neutral current interactions in which a track that may be reconstructed as a muon might be produced in the hadronic shower leading to a misidentification of the event as a charged-current interaction. The other possible background will be the τ contamination which may arise when the atmospheric ν_μ and ν_e oscillates into a ν_τ that produces a τ lepton through CC interaction with nuclei, that eventually decays into muons with a branching ratio of $\sim 17\%$. In this thesis work, we have considered only the CC analysis because this is one of the major channels in the ICAL having the largest sensitivity.

A marginalized χ^2 analyses using reconstructed neutrino energy and muon zenith angle binning scheme for the 10 years of running INO-ICAL detector has been performed. We conclude that the ICAL detector can measure the atmospheric neutrino mixing parameters, $\sin^2\theta_{23}$ and $|\Delta m^2_{32}|$, with the precision of about 13% and 27% at 3σ confidence interval respectively. ICAL detector is also capable of ruling out the wrong octant of θ_{23} at the 2σ confidence level with 10 years of exposure. The mass hierarchy sensitivity for the desired period of ICAL detector is more than 2σ confidence level with the analysis techniques described in this thesis.

In conclusion, the inclusion of hadronic information together with the muon informa-

tion improves the sensitivity of ICAL for precision measurement of $\sin^2\theta_{23}$ and $|\Delta m^2_{32}|$ by about 20% for results with muon information alone. Also, the θ_{23} octant determination capability of ICAL improves with the addition of hadron information. However, there is no significant improvement in the mass hierarchy determination capability of ICAL detector over the muon only analysis. Nevertheless, a significant improvement has been seen with the inclusion of hadron information in a different way [122]. Moreover, the importance of the method presented in this thesis shows that the inclusion of the hadron response together with the muon response of the ICAL detector is crucial to achieve the physics goals of INO. Many improvements in the resolutions and efficiencies are also possible using better track fitting algorithms, improving the material budget, better implementation of the magnetic field interpolation etc. Including the hadron direction estimation might further improve the physics capabilities of the ICAL detector.

At present, construction of INO tunnel, cavern and other site infrastructure are underway and are expected to complete within 3-4 years. INO is expected to put its first ICAL module by the year 2020 and will start taking data soon after its placement with this module. The next two modules will also be installed later. With approximately 10 years of data taking, the ICAL will be capable of determining the correct neutrino mass hierarchy with a significance of more than 3σ and mixing parameters with good precision. In the same time frame, the other experiments like T2K, MINOS, PINGU and Noνa are also expected to measure these parameters at a significant confidence levels as described in Chapter 1. Also, the synergy of the ICAL detector results with the results from these various experiments will open up a possibility to determine the new physics. Unique advantage of atmospheric neutrino study with ICAL detector will play an important and complementary role in the next discovery era of neutrino physics.

Bibliography

[1] INO Collaboration, S. Atthar et al., *"The Technical Design Report of INO-ICAL Detector"* (2006).

[2] India-based Neutrino Observatory (INO), http://www.ino.tifr.res.in/ino/.

[3] http://en.wikipedia.org/wiki/Standard-Model.

[4] ATLAS Collaboration, *"Observation of a new particle in the search for the standard model Higgs boson with the ATLAS detector at the LHC"*, Phys. Lett. B 716, 1 (2012).

[5] CMS Collaboration, *"Observation of a new boson at a mass of 125 GeV with the CMS experiment at the LHC"*, Phys. Lett. B 716, 30 (2012).

[6] CMS Collaboration, *"Observation of a new boson with mass near 125 GeV in pp collisions at $\sqrt{s}$ = 7 and 8 TeV"*, J. High Energy Phys. 06, 081 (2013).

[7] W. Pauli, *"Liebe Radioaktive Damen und Herren"*, letter to physicists at Tubingen (1930), cited by A. Franklin, *"Are there really Neutrinos?"*, p. 71 (2000).

[8] J. Chadwick, *"Possible Existence of a Neutron"*, Nature 129, 312 (1932).

[9] J. Chadwick, *"The Existence of a Neutron"*, Proc. Royal Soc. A 136, 692 (1932).

[10] E. Fermi, *"Versuch einer Theorie der beta-Strahlen. I."*, Zeitschrift fur Physik 88, 161 (1934).

[11] F. Reines and C. Cowan, *"Detection of the Free Neutrino"*, Phys. Rev. 92, 830 (1953).

[12] G. Danby et al., *"Observation of High-Energy Neutrino Reactions and the Existence of Two Kinds of Neutrinos"*, Phys. Rev. Lett. 9, 36 (1962).

[13] The ALEPH, DELPHI, L3, OPAL Collaborations et al., *"Precision Electroweak Measurements on the Z Resonance"*, Phys. Reports 427, 257 (2006).

[14] DONUT Collaboration, *"Observation of Tau Neutrino Interactions"*, Phys. Lett. B 504, 218 (2001).

[15] Sigl, Guenter, *" High Energy Neutrinos and Cosmic Rays"*, Proc. Int. Sch. Phys. Fermi 182, 145-184 (2012).

[16] http://www2.astro.psu.edu/users/nnp/cr.html.

[17] B. Pontecorvo, *"measonium and anti-mesonium"*, Zh. Eksp. Theor. Fiz. 33, 549 (1957).

[18] B. T. Cleveland et al., *"Measurement of the solar neutrino flux with the Homestake chlorine detector"*, Astrophys. J. 496, 505 (1998).

[19] B. Pontecorvo, Sov. Phys. JETP 26, 984 (1968) and Zh. Eksp. Teor. Fiz 53, 1717 (1967).

[20] Z. Maki, M. Nakagawa and S. Sakata, Prog. Theor. Phys. 28, 870 (1962).

[21] S. P. Mikheyev and A. Y. Smirnov, *"Resonance Amplification of Oscillations in Matter and Spectroscopy of Solar Neutrinos"*, Sov. J. Nucl. Phys. 42, 913 (1985).

[22] Wendell, R. et al., *"Atmospheric neutrino oscillation analysis with sub-leading effects in Super-Kamiokande I, II, and III"*, Feb 2010. URL http://arxiv.org/abs/1002.3471

[23] John N. Bahcall, Aldo M. Serenelli, Sarbani Basu, *"New solar opacities, abundances, helioseismology, and neutrino fluxes"*, Astrophys. J. 621:L85-L88 (2005).

[24] D. N. Abdurashitov et al., *"The Russian-American gallium experiment (SAGE) Crneutrino source measurement"*, Phys. Rev. Lett. 77, 4708-4711, (1996).

[25] W. Hampel et al., *"GALLEX solar neutrino observations: Results for GALLEX IV"*, Phys. Lett. B447, 127-133 (1999).

[26] K. S. Hirata et al., *"Experimental Study of the Atmospheric Neutrino Flux"*, Phys. Lett. B 205, 416 (1988).

[27] T. J. Haines et al., *"Calculation of atmospheric neutrino induced backgrounds in a nucleon decay search"*, Phys. Rev. Lett. 57, 1986-1989 (1986).

[28] Super-Kamiokande Collaboration, Y. Fukuda et al., *"Evidence for Oscillation of Atmospheric Neutrinos"*, Phys. Rev. Lett. 81, 1562(1998)

[29] Super-Kamiokande Collaboration, Y. Fukuda et al., *"Measurement of the Flux and Zenith-Angle Distribution of Upward Throughgoing Muons by Super-Kamiokande"*, Phys. Rev. Lett. 82, 2644 (1999).

[30] SNO Collaboration, Q. R. Ahmad et al., *"Direct Evidence for Neutrino Flavor Transformation from Neutral-Current Interactions in the Sudbury Neutrino Observatory"*, Phys. Rev. Lett. 89, 011301 (2002).

[31] SNO Collaboration, *"Electron energy spectra, fluxes, and day-night asymmetries of B^8 solar neutrinos from measurements with NaCl dissolved in the heavy-water detector at the Sudbury Neutrino Observatory"*, Phys. Rev. C 72, 055502 (2005).

[32] KamLAND, K. Eguchi et al., *"First results from KamLAND: Evidence for reactor anti- neutrino disappearance"*, Phys. Rev. Lett. 90, 021802 (2003).

[33] Super-Kamiokande Collaboration, K. Abe et al., *"Search for Differences in Oscillation Parameters for Atmospheric Neutrinos and Antineutrinos at Super-Kamiokande"*, Phys. Rev. Lett. 107, 241801 (2011).

[34] KamLAND, T. Araki et al., *"Measurement of neutrino oscillation with KamLAND: Evidence of spectral distortion"*, Phys. Rev. Lett. 94, 081801 (2005).

[35] Kamiokande-II, K. S. Hirata et al., *"Evidence for oscillation of atmospheric neutrinos"*, Phys. Lett. B 280, 146 (1992).

[36] R. Becker-Szendy et al., *"Neutrino measurements with the IMB detector"*, Nucl. Phys. Proc. Suppl. 38, 331 (1995).

[37] M. Ambrosio et al., *"Matter effects in upward-going muons and sterile neutrino oscillations"*, Phys. Lett. B 517, 59 (2001).

[38] M. C. Sanchez et al., *"Observation of atmospheric neutrino oscillations in Soudan 2"*, Phys. Rev. D 68, 113004 (2003).

[39] Super-Kamiokande collaboration, Y. Fukuda et al., *"Measurement of a small atmospheric ν_μ / ν_e ratio"*, Phys. Lett. B 433, 9 (1998).

[40] Super-Kamiokande collaboration, Y. Fukuda et al., *"Study of the atmospheric neutrino flux in the multi-GeV energy range"*, Phys.Lett. B436, 33 (1998).

[41] Super-Kamiokande collaboration, Y. Fukuda et al.,*"Measurement of the Flux and Zenith-Angle Distribution of Upward Throughgoing Muons by Super-Kamiokande"* Phys. Rev. Lett. 82, 2644 (1999).

[42] The Super-Kamiokande collaboration, Y. Fukuda et al., *"Evidence for oscillation of atmospheric neutrinos"*, Phys.Rev. Lett. 81, 1562 (1998).

[43] Super-Kamiokande collaboration, R.wendell et al., *"Atmospheric neutrino oscillation analysis with subleading effects in Super-Kamiokande I, II, and III"*, Phys. Rev. D 81, 092004 (2010).

[44] The IceCube Collaboration, H. Kolanoski et al., *"IceCube - Astrophysics and Astroparticle Physics at the South Pole"*, arXiv:1111.5188 (2011).

[45] The ANTARES collaboration, J.A. Aguilar et al., *ANTARES: the first undersea neutrino telescope"*, Nulc. Inst. Meth. A 656, 11 (2011).

[46] The IceCube collaboration, A. Gros et al., *Atmospheric Neutrino Oscillations in IceCube"*, Nucl. Phys. Proc. Suppl. 237-238, arXiv:1301.4339 [hep-ex] (2013).

[47] The ANTARES collaboration, S. Adrian-Martinez et al, *"Measurement of atmospheric neutrino oscillations with the ANTARES neutrino telescope"*, Phys. Lett. B714, 224 (2012).

[48] Double Chooz Collaboration, Y. Abe et al., *"Reactor $\bar{\nu}_e$ disappearance in the Double Chooz experiment"*, Phys. Rev. D 86, 052008 (2012).

[49] Double Chooz Collaboration, Y. Abe et al., *"Indication of Reactor $\bar{\nu}_e$ Disappearance in the Double Chooz Experiment"*, Phys. Rev. Lett. 108, 131801 (2012).

[50] Double Chooz Collaboration, Y. Abe et al., *"Improved measurements of the neutrino mixing angle θ_{13} with the Double Chooz detector"*, JHEP 10, 086 (2014).

[51] DAYA-BAY Collaboration, F. An et al., *"Observation of Electron-Antineutrino Disappearance at Daya Bay"*, Phys. Rev. Lett. 108, 171803 (2012).

[52] DAYA-BAY Collaboration, F. An et al., *"Spectral measurement of electron antineutrino oscillation amplitude and frequency at Daya Bay"*, Phys. Rev. Lett. 112, 061801 (2014).

[53] DAYA-BAY Collaboration, F. An et al., *"Improved Measurement of Electron Antineutrino Disappearance at Daya Bay"*, Chin. Phys. C37, 011001 (2013).

[54] RENO Collaboration, J. K. Ahn et al., *"RENO: An Experiment for Neutrino Oscillation Parameter θ_{13} Using Reactor Neutrinos at Yonggwang"*, arXiv:1003.1391 [hep-ex].

[55] RENO collaboration, J. Ahn et al., *"Observation of Reactor Electron Antineutrinos Disappearance in the RENO Experiment"*, Phys. Rev. Lett. 108, 191802 (2012).

[56] RENO Collaboration, Seon-Hee Seo, *"New Results from RENO and The 5 MeV Excess"*, Neutrino 2014 proceeding, arxiv:1410.7987 [hep-ex].

[57] MINOS Collaboration, P. Adamson et al., *"Improved Search for Muon-Neutrino to Electron-Neutrino Oscillations in MINOS"*, Phys. Rev. Lett. 107, 181802 (2011).

[58] MINOS Collaboration, P. Adamson et al. , *"Combined Analysis of ν_μ Disappearance and $\nu_\mu \to \nu_e$ Appearance in MINOS Using Accelerator and Atmospheric Neutrinos"*, Phys. Rev. Lett. 112, 191801 (2014).

[59] MINOS Collaboration, P. Adamson et al., *"Electron Neutrino and Antineutrino Appearance in the Full MINOS Data Sample"*, Phys. Rev. Lett. 110, 171801 (2013).

[60] T2K Collaboration, K. Abe et al., *"Indication of Electron Neutrino Appearance from an Accelerator-Produced Off-Axis Muon Neutrino Beam"*, Phys. Rev. Lett. 107, 041801 (2011).

[61] T2K Collaboration, K. Abe et al., *"Precise Measurement of the Neutrino Mixing Parameter θ_{23} from Muon Neutrino Disappearance in an Off-Axis Beam"*, Phys. Rev. Lett. 112, 181801 (2014).

[62] T2K Collaboration, K. Abe et al., *"Observation of Electron Neutrino Appearance in a Muon Neutrino Beam"*, Phys. Rev. Lett. 112, 061802 (2014).

[63] NOνA Collaboration, D.S. Ayres et al., hep-ex/0503053.

[64] G. L. Folgi et al., *"Global analysis of neutrino masses, mixings and phases: entering the era of leptonic CP violation searches"*, arXiv:1205.5254 [hep-ph](2012).

[65] M. C. Gonzalez-Gracia et al., *"Global fit to three neutrino mixing: critical look at present precision"*, JHEP 1212, 123 (2012).

[66] F. Capozzi et al., *"Status of three-neutrino oscillation parameters, circa 2013"*, Phys. Rev. D 89, 093018 (2013).

[67] M. C. Gonzalez-Gracia, *"Global analyses of oscillation neutrino experiments"* Physics of the Dark Universe 4, 1-5, (2014).

[68] K. Abe et al., *"Letter of Intent: The Hyper-Kamiokande Experiment-Detector Design and PhysicsPotential"*, arXiv:1109.3262.

[69] Hyper-Kamiokande Working Group collaboration, E. Kearns et al., *"Hyper-Kamiokande Physics Opportunities"*, arXiv:1309.0184.

[70] D. J. Koskinen, *"IceCube-DeepCore-PINGU: Fundamental neutrino and dark matter physics at the South Pole"*, Mod. Phys. Lett. A 26, 2899 (2011).

[71] Walter Winter, *"Neutrino mass hierarchy determination with IceCube-PINGU"* Phy Rev D.88, 013013 (2013).

[72] A. Rubbia, *"Future Liquid Argon Detectors"*, Nuclear Physics B Proceedings Supplement 00, 1–9 arXiv:1304.0127 [physics.ins-det](2013).

[73] R. Gandhi et al., "Resolving the Mass Hierarchy with Atmospheric Neutrinos using a Liquid Argon Detector", Phys. Rev. D 78, 073001 (2008).

[74] V. Barger et al., *"Configuring the Long-Baseline Neutrino Experiment"*, arXiv:1307.2519.

[75] D. Indumathi and M. V. N. Murthy, *"Question of hierarchy: Matter effects with atmospheric neutrinos and antineutrinos"*, Phys. Rev. D 71, 013001 (2005).

[76] C. V. Achar et al., *"Particle astrophysics with high energy neutrinos"*, Physics Letters 18, 196 (1965).

[77] Infolytica Corp., Electromagnetic field simulation software, http://www.infolytica.com/en/products/magnet/.

[78] S. P. Behera et al "Simulation Studies for Electromagnetic Design of INO ICAL Magnet and its Response to Muons" arXiv:1406.3965 (2014).

[79] R. Santonico, R. Cardarelli, *"Development of resistive plate counters"*, Nucl. Instr. and Meth. 187, 377 (1981).

[80] R. Cardarelli et al., "Progress in resistive plate counterss", Nucl. Instr. and Meth. 263 20 (1988).

[81] BaBar Collaboration, *"BaBar Technical Design Report"*, SLAC Report SLAC-R-95-457 (1995).

[82] A. Abashian et al., *"The Belle Detector"*, Nucl. Instr. and Meth. A 479 (2002).

[83] OPERA Collaboration, M. Guler et al., *"An appearance experiment to search for ν_μ-ν_τ oscillations in the CNGS beam: experimental proposal"*, CERN/SPSC 2000-028 (2000).

[84] ALICE Collaboration, *"ALICE Technical Design Report of the time-of-flight system (TOF)"*, CERN-LHCC 2000-12 (2000).

[85] ATLAS Collaboration, *"ATLAS muon spectrometer: Technical Design Report"*, CERN-LHCC 97-22 (1997).

[86] CMS Collabration, Technical Proposal, CERN-LHCC-94-38 (1994); CMS Collaboration JINST, 3, S08004 (2008).

[87] L. Pontecorvo, *"Proceedings of the II International Workshop on The Resistive Plate Chambers in Particle physics and Astrophysics"*, Scientifica Acta 8, 145 (1993).

[88] C. Bacci et al., *"A hodoscope made of resistive plate chambers to identify muonsin a fixed targed beauty hadroproduction experiment"*, Nucl. Instr. Meth. A 324, 83-92 (1993)

[89] R. Cardarelli, A. Di Caiccio, and R. Santonico, *" Performance of a resistive plate chamber operating with pure CF3Br"*, Nucl. Instr. Meth., A 333, 399-403 (1993).

[90] P. Camarri et al., "Streamer suppression with SF6 in RPCs operated in avalanche mode", Nucl. Instr. and Meth. A 414, 317-324 (1998).

[91] S. Bhide et al, *"Preliminary results from India-based Neutrino Observatory detector $R\&D$ programme"*, PRAMANA-Journal of Physics 69(6),1015-1023 (2007).

[92] V. M. Datar et al, *"Development of glass resistive plate chambers for INO experiment"*, Nucl. Instr. and Meth. 602 744-748 (2009).

[93] S. Biswas et al., *"Performances of silicon coated high resistive bakelite RPC"*, arXiv:1206.5627 (2012).

[94] H. Czyrkowski et al., *"New development on resistive plate chambers for high rate operation"*, Nucl. Instr. Meth. A 419, (1998).

[95] M/s Alpha Pneumatics, Mumbai, India.

[96] Y. Hoshi et al, *"Proc. Workshop on RPCs and Related Detectors, Coimbra"* (2001).

[97] W. Riegler, *"Induced Signals in Resistive Plate Chambers"*, NIM A 491, 258, (2002)

[98] Hewett, J. L. et al., *"Fundamental Physics at the Intensity Frontier"*, arXiv:1205.2671 [hep-ex] (2012).

[99] D. Casper, *"The nuance Neutrino Simulation, and the Future"*, Nucl.Phys. Proc.Suppl.112, 161 [arXiv:0208030][hep-ph](2002).

[100] GEANT simulation toolkit wwwasd.web.cern.ch/wwwasd/geant/

[101] R. E. Kalman, *"A new approach to linear filtering and prediction problems"*, J. Basic Eng. 82, 35, (1960).

[102] A. Chatterjee et al., *"A Simulations Study of the Muon Response of the Iron Calorimeter Detector at the India-based Neutrino ObservatoryA Simulations Study of the Muon Response of the Iron Calorimeter Detector at the India-based Neutrino Observatory"*, JINST 9 P007001 (2014).

[103] K. Rawat et al. *"Simulations Study of Muon Response in the Peripheral Regions of the Iron Calorimeter Detector at the India-based Neutrino Observatory"* (accepted to be published in JINST).

[104] https://root.cern.ch/

[105] A. Rotondi, P. Montagna,*"Fast calculation of Vavilov distribution"*, Nuclear Instrumentation and Methods B 47, 215-224 (1990).

[106] William R. Leo., *"Techniques for Nuclear and Particle Physics Experiments"*.

[107] https://desktop-publishing.web.cern.ch/desktop-publishing/crnrepex.pdf

[108] L. S. Mohan et al., "Hadron energy resolution as a function of iron plate thickness at ICAL", JINST 9 T09003 (2014).

[109] A. Ghosh et al., *"Determining the neutrino mass hierarchy with INO, T2K, NOvA and reactor experiments"*, JHEP 04, 009 (2013).

[110] T. Thakore et al., *"The reach of INO for atmospheric neutrino oscillation parameters"*, JHEP 05, 058 (2013).

[111] M. Honda, T. Kajita et al., *"New calculation of the atmospheric neutrino flux in a three-dimensional scheme"*, Phys. Rev. D 70, 043008 (2004).

[112] M. M. Devi et al., *"Hadron energy response of the Iron Calorimeter detector at the India-based Neutrino Observatory"*, JINST 8 P11003 (2013).

[113] M. Ba nuls, G. Barenboim, and J. Bernabeu, *"Medium effects for terrestrial and atmosphericneutrino oscillations"*, Phys. Lett. B 513,391-400 (2001).

[114] J. Bernabeu, S. Palomares-Ruiz, and S. Petcov, *"Atmospheric neutrino oscillations, θ_{13} and neutrino mass hierarchy"*, Nucl. Phys. B669, 255-276 (2003).

[115] D. Indumathi, M.V.N. Murthi, *"A question of hierarchy: matter effects with atmospheric neutrinos and anti-neutrinos"*, Phys. Rev. D 71, 013001 (2005).

[116] S. Petcov and S. Palomares-Ruiz, *"On the atmospheric neutrino oscillations, theta(13) and neutrino mass hierarchy"*, arXiv:0406106 [hep-ph].

[117] A. M. Dziewonski and D. L. Anderson, *"Preliminary reference earth model"*, Phys. Earth Planet. Interior 25, 297-356 (1981).

[118] H. Nunokawa, S. J. Parke and R. Zukanovich Funchal, *"Another possible way to determine the neutrino mass hierarchy"*, Phys. Rev. D 72, 013009 (2005).

[119] M. C. Gonzalez-Garcia, M. Maltoni et al, *"Atmospheric neutrino oscillations and new physics"*, Phys. Rev. D 70, 033010 (2004).

[120] M. Ghosh et al., *"Can atmospheric neutrino experiments provide the first hint of leptonic CP violation?"*, Phys. Rev. D 89, 011301 (2014).

[121] A. Ghosh, S. Choubey, *"Measuring the Mass Hierarchy with Muon and Hadron Events in Atmospheric Neutrino Experiments"*, JHEP 2013,174 (2013).

[122] M. M. Devi et al., *"Enhancing sensitivity to neutrino parameters at INO combining muon and hadron information"*, JHEP 10, 189 (2014).